

**Search for New Massive Long-Lived Neutral Particles
decaying to Photons in pp Collisions at $\sqrt{S} = 8$ TeV**

A DISSERTATION
SUBMITTED TO THE FACULTY OF THE GRADUATE SCHOOL
OF THE UNIVERSITY OF MINNESOTA
BY

Tambe Ebai Norbert

IN PARTIAL FULFILLMENT OF THE REQUIREMENTS
FOR THE DEGREE OF
Doctor of Philosophy

Prof. Yuichi Kubota

April, 2015

**© Tambe Ebai Norbert 2015
ALL RIGHTS RESERVED**

Acknowledgements

There are many people that have earned my gratitude for their contribution to my time in graduate school.

The universe is unbiased, she chooses to reveal herself to all who have the correct attitude.

Tambe E. Norbert

So I would claim you are profoundly misled by thinking about physics as similar to logic or number theory. Its not! its dynamical evolution, and most results of physics problems are not nice numbers like 1 or π or even e^π .

by Prof. Matt Strassler

Dedication

No, I have nothing against Mr. Einstein. He is a kind person and has done many good things, some of which will become part of the music. I will write to him and try to explain that the ether exists, and that its particles are what keep the Universe in harmony, and the life in eternity.

Nikola Tesla

The Universe is unbiased, she chooses to reveal herself to whomever she wants.

Tambe E. Norbert

Abstract

Dark matter particles are believed to be neutral, stable, weakly interacting with ordinary matter and maybe massive. The hunt for dark matter particles is on! There are theoretical models which predict the existence of dark matter particles that can be produced in a proton-proton collider like the Large Hadron Collider provided there is sufficient center of mass energy. Gauge Mediating Supersymmetric Models are examples of such models. These models describe the production and decay into isolated energetic photons, new, massive, neutral, weakly interacting particles known as supersymmetric particles. The Neutralino ($\tilde{\chi}_1^0$), being the lightest supersymmetric particle in terms of mass, is a prime example and its decay into a photon is accompanied by a light weakly interacting and stable supersymmetric particle, the gravitino (\tilde{G}) which is considered to be a very good candidate for dark matter particles. The resulting photon from such a decay, is understood to be delayed in its arrival time at the detector. This timing delay is due to inherent dynamics understood and well described by models beyond the standard model. The signature of a delayed photon is not specific to only supersymmetric models but could be the result of probably some new kind of physics unrelated to the standard model. Using the Compact Muon Solenoid detector at the LHC, we have performed a search for delayed photons produced from proton-proton collisions at the center of mass energy, $\sqrt{S} = 8$ TeV. We did not find any excess of events over standard model background. Consequently, we compute an upper limit on the cross section $\sigma_{\tilde{\chi}_1^0} > 0.02$ pb on the possible production and decay of a lightest neutralino with mass and proper lifetime; $m_{\tilde{\chi}_1^0} \geq 235$ GeV/c² and $\tau_{\tilde{\chi}_1^0} \geq 35$ ns respectively, as described in the gauge mediated supersymmetric models. We also show that using only the timing information of the electromagnetic calorimeter as an observable, the CMS detector is sensitive to neutralinos with lifetimes up to 30 ns and mass, $m_{\tilde{\chi}_1^0} = 255$ GeV/c² which no previous experiment had shown. We provide hints on possible improvements which might help discover delayed photons in future search analysis.

Contents

Acknowledgements	i
Dedication	ii
Abstract	iii
List of Tables	viii
List of Figures	x
1 Introduction	1
2 Model and Phenomenology of Long-Lived Particles	5
2.1 The Standard Model of Particle Physics	5
2.1.1 Main Components of the SM	5
2.1.2 Spontaneous Symmetry Breaking	11
2.1.3 Limitations of the Standard Model	14
2.2 Beyond Standard Model Physics	15
2.2.1 Supersymmetry	18
2.2.2 Minimal Supersymmetric Standard Model	20
2.2.3 Soft Supersymmetry Breaking	24
2.2.4 Gauge Mediated Supersymmetry Breaking and Phenomenology .	25
2.3 Long-Lived Particles in GMSB Models	32
2.3.1 Production of supersymmetric particles at Hadron Colliders . .	32
2.3.2 Particle Production Cross-section and Decay Rate	35

2.3.3	Decay of supersymmetric particles in CMS detector	38
2.4	Previous Search Experiments and Results	42
3	Hadron Collider and Detector	43
3.1	Large Hadron Collider	43
3.1.1	Overview	43
3.1.2	Colliding Energy	44
3.1.3	Luminosity	45
3.1.4	Superconducting Electromagnets	47
3.1.5	Timing	48
3.2	Compact Muon Solenoid	53
3.2.1	Overview	53
3.2.2	Tracker	57
3.2.3	Calorimeter	59
3.2.4	Muon Chambers	64
3.2.5	Particle Detection	65
3.2.6	Triggering	66
4	Timing Reconstruction and Calibration	68
4.0.7	Electromagnetic Calorimeter Readout Chain	69
4.0.8	Timing Extraction	72
4.0.9	Timing Resolution	74
4.0.10	Timing Calibration Procedure	76
4.0.11	Electromagnetic Calorimeter Timing Performance	86
5	Physics Objects Reconstruction and Identification in CMS	91
5.1	Physics Objects Reconstruction	91
5.1.1	Supercluster Reconstruction	92
5.1.2	Vertex and Track Reconstruction	95
5.1.3	Photon or Electron Identification	97
5.1.4	Muon Reconstruction	102
5.1.5	Jet Reconstruction	104
5.1.6	Missing Transverse Energy Reconstruction	105

5.2	Anomalous Signals	107
5.3	Using Timing for Event Cleaning	110
6	Search Analysis for Long-Lived Particles	111
6.1	Analysis Strategy	111
6.1.1	Signal and Background Modelling	113
6.1.2	Datasets	114
6.2	Event Selection	116
6.2.1	Trigger	118
6.2.2	Offline Selection	119
6.2.3	ECAL Time	122
6.3	Background Estimation	127
6.3.1	Non-Collision Backgrounds	129
6.3.2	Collision Backgrounds	134
6.3.3	Event Cleaning, Veto Performance and Fake Rate	135
6.3.4	Background Estimation Cross Check	139
6.4	Results	144
6.5	Systematic Studies	145
7	Statistical Analysis	147
7.1	Limit Computation	147
7.1.1	CLs Technique	148
7.1.2	Statistical Test Formalism	149
7.1.3	Test Statistics and p -values	151
8	Limit Interpretation	155
8.1	Signal Efficiency and Acceptance	155
9	Conclusion	160
	Bibliography	161
	Appendix A. Glossary and Acronyms	167
A.1	Glossary	167

A.2 Acronyms	167
------------------------	-----

List of Tables

2.1	SM particles and their gauge multiplets(representation) with quantum numbers. the numbers for example (3 , 2 , $\frac{1}{6}$) means (<i>triplet, doublet, Y = 1/6</i>) representations.	11
2.2	Supermultiplets and particle spin in SM and Supersymmetry.	19
2.3	Supermultiplets and components in Supersymmetry.	20
2.4	Chiral supermultiplets and representation in Minimal Supersymmetric SM (MSSM). Super symmetric particles (sparticles) have a $\tilde{}$ on them. Spin -0 fields are complex scalars while spin-1/2 fields are left-handed two component Weyl fermions.	21
2.5	Gauge supermultiplets and representation in Minimal Supersymmetric SM (MSSM). Super symmetric particles (sparticles) have a $\tilde{}$ on them.	21
3.1	The LHC operation parameter conditions during RUN 1:2010-2013 . . .	50
3.2	CMS Detector Material and Resolution(Time resolution: $N \approx 35$ ns, $\bar{C} \approx 0.020$ ns [?])	55
4.1	Table Comparing Timing Resolution performance of 2011 with 2012 . .	90
5.1	Simple Cut-Based criteria for High energy electron and photon identification in CMS	101
6.1	Dataset and corresponding integrated luminosity totaling 19.1 fb^{-1} used in this analysis	115
6.2	The signal GMSB SPS8 MC samples for difference Δ and Branching Ratios used in this analysis	116
6.3	The $\gamma +$ jets samples used in this analysis	116
6.4	The photon identification and selection criteria used in this analysis . .	120
6.5	The Jet ID selection used in this analysis	121

6.6	Fake rates for different non-collision cleaning.	135
6.7	ABCD Control Regions (CRs) for estimating non-collision background. .	137
6.8	$A' B' C' D'$ and $I I'$ CRs for estimating collision background.	138
6.9	Result from closure test of background estimation technique using 0 and 1-jet events. Numbers in bracket represent our expected background estimate using ABCD method.	139
6.10	Result of observed events and estimated background from signal sample, events with at least 2-jets. Numbers in bracket represent our observed number of events while numbers not in bracket are our expected number of background events estimated using ABCD method.	145
6.11	Final number for $\Lambda = 180$ TeV GMSB SPS8 MC signal events events passing our selection cuts.	145
6.12	Summary of systematic uncertainties used in this analysis and applied to our cross-section upper limit, σ_{UL} calculation.	146
A.1	Acronyms	168

List of Figures

2.1	Higgs boson ‘‘Mexican hat’’ potential, $V(\phi^*\phi) = \mu^2(\phi^*\phi) + \lambda(\phi^*\phi)^2$, which leads to spontaneous symmetry breaking with choice of parameters $\mu^2 < 0$, $\lambda > 0$	13
2.2	SM particles and their interactions with vector bosons as mediators.	13
2.3	Higgs self energy diagrams showing how the higgs boson mass is computed from both Higgs field and supersymmetric partner particle contributions.	16
2.4	SUSY Mass spectra in the mGMSB SPS8 model (left) and GGM Model (right) with mass of gluino ($M_{\tilde{g}} = 1.0$ TeV)	24
2.5	Feynman diagrams of gravitino/golstino, \tilde{G} , gaugino and scalar interactions with superpartner pairs (ψ, ϕ) scalar (a) and (λ, A) gaugino (b) decay to gravitino.	30
2.6	Supersymmetry production cross-section against sparticle mass for different modes of supersymmetry production at a proton-proton collider. $pp \rightarrow \tilde{g}\tilde{g}$ processes have the dominant production cross-section.	33
2.7	Feynman diagrams for gluino single (<i>top left</i>) and double (<i>top right</i>) photon and squarks single (<i>bottom left</i>) and double (<i>bottom right</i>)photon production from cascade decays of gluino and squark at LHC.	34
2.8	Neutralino transverse momentum distribution(<i>top left</i>) and proper decay length(<i>top right</i>) with its decayed photon transverse momentum distribution(<i>bottom left</i>) and time of arrival at ECAL(<i>Bottom right</i>) for GMSB SPS8 model.	41
2.9	Neutralino lifetime and mass upper limit from ATLAS(left) and CMS(right) 7 TeV analysis with non-pointing photons and MET.	42

3.1	Schematic diagram showing the full Large hadron Collider. Image taken from [33]	44
3.2	Cumulative luminosity versus day delivered to (blue), and recorded by CMS (orange) during stable beams and for p-p collisions at 8 TeV centre-of-mass energy in 2012.	47
3.3	Longitudinal Profile taken with LDM detector showing definition of Ghost/Satellite bunches with respect to main bunches.	51
3.4	(left) Arrival time distribution(red) of ATLAS MBTS for LHC fill 1533 during 2010 Pb-Pb run and LDM profile(black) for Beam2(same for Beam1). (Right) Timing of Clusters in the CMS endcap calorimeters for fill 1089:Left: EEP detector(left side of IP $z < 0$) Right: EEM detector(right side of IP, $z > 0$). NB: Plots taken from [41] and [42]	52
3.5	CMS Detector showing the different subdetectors and their material.	54
3.6	Schematic diagram of CMS detector view showing definition of cordinates as used by CMS.	56
3.7	Schematic diagram of CMS Tracker showing the silicon pixel detector region (inner closer to LHC beam) and silicon strip reigion (outer).	57
3.8	Schematic diagram of CMS calorimetry system with HCAL enclosing ECAL in the Barrel and Endcap regions.	60
3.9	Layout of the CMS electromagnetic calorimeter showing the arrangement of crystal modules, supermodules in the barrel with the preshower infront of endcap with supercrystals.	62
3.10	Longitudinal view of CMS showing the coverage range of its sub-detectors.	65
3.11	Transverse slice of the CMS detector showing how different types of particles interact and hence identified using this detector.	66
4.1	Schematic diagram of the CMS ECAL ReadOut Chain.	70
4.2	Typical pulse shape of a given signal showing signal amplitude and time.	72
4.3	<i>Left:</i> A measured ECAL pulse shape for each channel. <i>Right:</i> $T - T_{MAX}$ Vs $R(T)$ showing the distribution of $T(R)$. Solid line is reference shape or shape from test beam while dots correspond to a 10 discrete samples corresponding to signal from a single event in a single channel or crystal.	73

4.4	Deviation of the timing difference as a function of A_{eff}/σ_n between two crystals sharing an energy in the same electromagnetic shower obtained during electron testbeam measurements. The single crystal energy scales for barrel (EB) and endcap (EE) is overlaid. The fitted results give $N = (35.1 \pm 0.2)$ ns and $\bar{C} = (20 \pm 4)$ ns.	76
4.5	<i>Top 3:</i> Timing calibration maps showing the distribution of mean time for each channel/PbWO ₄ crystal in EB (top) and EE (below: EE-(left), EE+(right)) before calibration. <i>Bottom 3:</i> Timing calibration maps showing the distribution of mean time for each channel/PbWO ₄ crystal in EB (top) and EE (below: EE-(left), EE+(right)) after calibration. After calibration most crystals have an average time of zero(Green). . .	80
4.6	<i>Top:</i> Crystal mean time distribution for crystals in readout electronics EB±8. Crystal time obtained from Laser data. <i>Bottom:</i> Crystal mean time distribution for crystals in readout electronics EE+ and EE-. The adjustment for global timing shift per FED due to difference in light source for each CCU has been shown to reduce the possibility of CCU showing false timing shift. The figures show the distributions of the Δt_{CCU} with corresponding RMS values after the global shift has been removed.	82
4.7	<i>Top Row:</i> Distribution of mean time as a function of crystal energy for EB prior (left) and after (right) timing bias corrections depending on amplitude have been applied. <i>Bottom Row:</i> Distribution of timing deviation (sigma) as a function of crystal energy for EB prior (left) and after (right) timing bias corrections depending on amplitude have been applied.	85
4.8	<i>Top:</i> Distribution of mean time as a function of amplitude (left) and Resolution as a function of amplitude (right) for different pseudo-rapidity regions in the barrel. <i>Bottom:</i> All modules in EB combined timing resolution as a function against η crystals in the same readout electronics in barrel (EB).	86

4.9	Ecal absolute time of a single reconstructed electron in $Z \rightarrow e^-e^+$ decay. The electron time is the seed (crystal with highest energy deposit)time of the electron in EB and EE	88
4.10	Ecal time difference between the two reconstructed electrons in $Z \rightarrow e^-e^+$ decay. The electron time is the seed (crystal with highest energy deposit) time with additional correction due to the time of flight of the electron in EB and EE	88
4.11	Resolution of time difference between : <i>Right</i> : Two most energetic crystals in the same readout unit, <i>Right</i> : Two most energetic crystals belonging to different readout units, as a function of effective amplitude($A_{eff} = A_1A_2/\sqrt{A_1^2 + A_2^2}$) normalized to noise in EB. Both crystals are from reconstructed electrons in $Z \rightarrow e^-e^+$ events.	89
5.1	Superclustering algorithm in ECAL for both hybrid (EB) and island (EE) clustering algorithms.	93
5.2	Superclustering in ECAL for hybrid clustering algorithm in barrel.	93
5.3	Superclustering in ECAL for Island clustering algorithm in barrel.	94
5.4	$Z \rightarrow e^+e^-$ mass plot showing resolution and energy scale that is obtained from applying energy scale corrections to account for intrinsic spread in crystal and photo-detector response and time-dependent corrections to compensate for channel response loss for EB (right) and EE (left)	98
5.5	Super-clusters showing resolution and energy scale that is obtained from applying energy scale corrections for EB (right) and EE (left)	98
5.6	Illustration of the differences between proton-proton collision muons, cosmic and halo muons. (a) Muons from collision propagating from the center and moving outwards in a well defined pattern, (b) Cosmic muons penetrating the detector and leaving signals in opposite hemispheres of the muon system, (c) Cosmic muons leaving signals in the tracker and opposite hemispheres, (d) cosmic muons entering and leaving the detector without passing through the muon detector layers, (e) beam halo muons penetrating the detector and leaving signals in the endcaps and (f) Cosmic muons entering the detector through the endcap and leaving through the barrel and which can happen in a vice-versa manner.	103

6.1	Schematic diagram showing $\tilde{\chi}_1^0 \rightarrow \gamma + \tilde{G}$ decay topology within the ECAL volume of the CMS detector. Proton beams are also shown showing the possible production of collision and non-collision delayed photons	118
6.2	Trigger efficiency turn-on curves for photon p_T and $E_T^{\text{miss}} > 25$ GeV (left) and for E_T^{miss} with photon $pt > 80$ GeV/c (right). The $\gamma +$ jets samples require photon $p_T > 170$ GeV/c for selecting events with true E_T^{miss}	119
6.3	Pulse shape profile showing a spike (solid line) and a real photon (dashed line) from data.	122
6.4	Timing distribution of photons showing timing measurements using seed crystal (black) and using Weighted Average basic cluster time (blue). Resolution (σ) from seed time is better compared to that for cluster time which is computationally intensive. Together with the χ^2 , the seed time performs better in identifying anomalous timing objects.	123
6.5	Timing distribution of photons showing timing of data and MC $\gamma +$ jets (blue) samples and data (red) before (left) and after (right) timing Calibration is applied to MC.	124
6.6	ECAL timing distribution of photons in barrel (EB), endcap (EE) and all of ECAL (ALL ECAL) with $p_T > 50$ GeV from data. A 2.5 ns delay timing structure is observed in endcap subdetector.	125
6.7	Sources of delayed photons produced from neutralino decay in the SPS8 model with $\Lambda = 180$ TeV and $c\tau = 6000$ mm arriving at ECAL.	126
6.8	ECAL time against η (left) and ECAL time against ϕ (right) for photons with $p_T > 60$ GeV from data. The lower plot shows the photon timing distribution for events with different jet multiplicity.	128
6.9	ECAL time Vs η (left) and ECAL time Vs ϕ (right) and $CSC(Seg, \gamma)\Delta\phi$ for photons with $p_T > 80$ GeV from data. Halo photons show a clear matched between CSC segments and ECAL cluster in $\Delta\phi$ with their distribution peaking at $\phi = 0, \pm\pi$ and also the shape of their expected time.	131

6.10	2 dimensional plot showing $DT\Delta\eta(Seg, \gamma)$ against $DT\Delta\phi(Seg, \gamma)$ for photons with $p_T > 80$ GeV, ECAL Time, $t_\gamma > 2$ ns and ECAL Time $t_\gamma < -3$ ns from proton-proton collision data (left) and pure cosmic muon data (right). Small $\Delta\eta$ and $\Delta\phi$ are cosmic photon candidates.	132
6.11	Plot showing <i>number of crystals</i> in photon supercluster for photons from the region with ECAL Time, $t_\gamma < 0$ ns. Figure shows the timing distribution of candidate true photons(black), spike candidate photons (magenta) and halo candidate photons (red). The toplogical swiss-cross variable ($1-E_4/E_1$) distribution is shown comparing true photons ($ t_\gamma < 1.0$) to spike populated sample.	134
6.12	Residual Background after tagging the different non-collision background sources using the methods described in text.	136
6.13	ECAL time, t_γ Vs η_γ (top) and t_γ Vs ϕ (bottom) for photons from SinglePhoton dataset (left) compared to electron candidates from the DoubleElectron dataset (right). All photons or electron candidates are in barrel subdetector. Most of the photons with $\phi = 0, \pm\pi$ are halo photons which are not observed in the Z boson candidate sample.	140
6.14	Di-electron candidate mass distribution and the time of both electrons for the signal $76 < m_Z < 100$ GeV/c^2 Z boson sample(left) and similar distributions from the Control ($50 < m_Z < 76$ GeV/c^2 and $100 < m_Z < 130$ GeV/c^2) sample (right). Candidates events from the DoubleElectron dataset.	141
6.15	<i>Top:</i> Control sample (left) and signal sample (right) of di-electron candidate mass distribution. <i>Bottom:</i> Figure showing definition of scale factor use in estimating the contributions from control sample in signal sample.	143
6.16	Timing distribution of genuine Z bosons after background contribution has been subtracted.	144
7.1	Sampling distributions for $f(t_\mu \mu)$ showing how one extracts the p -vlaues. left: is the using a analytic of the Asymptotic method and right: is from the HybridNew method.	152
7.2	Distribution of p -vlaues showing how upper limit on μ is extracted for a given threshold probability.	154

8.1	The reconstruction and selection efficiency (left) \times Acceptance ($t > 3$ ns) (right) against transverse decay length in laboratory frame for different $c\tau$ points.	156
8.2	Neutralino production cross section against proper delay length upper limit interpretation in SPS8 model. (Left) $\Lambda = 100$ TeV, (Right)(left) $\Lambda = 180$ TeV	157
8.3	Neutralino production cross section against neutralino mass upper limit at 95% confidence levels interpretation in SPS8 model.(Left) $C\tau = 11000$ mm, (Right) $C\tau = 6000$ mm	158
8.4	Neutralino two dimensional exclusion limit of neutralino mass (Λ) against proper delay length upper limit interpretation in SPS8 model in the decay $\tilde{\chi}_1^0 \rightarrow \gamma + \tilde{G}$ with limits from previous experiments shown.	159

Chapter 1

Introduction

We have performed a search for Neutral Massive Long-Lived Particles (NMLLP) decaying to photons using timing information. This analysis uses data recorded using the CMS detector from proton-proton (pp) collisions by the Large Hadron Collider (LHC) with a center of mass energy $\sqrt{S} = 8$ TeV.

Particles from the decay of NMLLP could be *Dark Matter* (DM) particles as they are weakly interacting and stable. Matter observed around us make up only 4.5% of our total universe or multiverse. It is best described with unmatched precision by simple symmetries known as gauge symmetries. The mathematical formulation of gauge symmetries used in our understanding of the visible or baryonic universe is best implemented in the Standard Model (SM). The SM cannot describe non-visible or non-baryonic matter (DM) which make up the larger percentage of matter content in our universe. Although a direct detection of DM is yet to be presented, indirect detection experiments in Cosmology and Astrophysics support speculation that non-visible matter is made up of particles which may be very stable or have long lifetime collectively called *Long-Lived* (LL) particles. In general, LL particles are either charged (electromagnetically charged (i.e interact with light (photons)) or color charged) or neutral (i.e cannot interact with light in the context of the SM).

Of particular interest to the scientific community are neutral LL particles, since DM is understood to not interact directly with light and could very weakly interact with visible matter. Recent negative search results is indicating that dark matter particles,

if they exists, could be very light i.e having very small mass of about a few eV to keV. These are known as Warm Dark Matter (WDM). DM particles could also be heavy with mass in the GeV to TeV mass range. These are called Cold Dark Matter (CDM). A common property is that they are stable.

The phenomenon of interest is a delayed photon produced in the decay of a meta-stable Next-to-Lightest Supersymmetric Particle (NLSP). The NLSP is the NMLLP. A classic example of a NLSP is the neutralino ($\tilde{\chi}_1^0$). It decays into a photon and the Lightest Supersymmetric Particle (LSP) called the gravitino (\tilde{G}). In R-parity conserving (RPC) models, supersymmetric particles like the neutralino are produced in pairs at a particle collider. The neutralinos are produced in a cascade decay of higher massive supersymmetric particles produced from proton-proton (pp) collisions. The gravitino being the LSP is stable, light in mass, neutral and weakly interacting with ordinary matter. This makes it a good candidate particle for DM. The photons from neutralino decay are energetic, isolated and delayed in their arrival time at a detector. These photons can be detected using the electromagnetic calorimeter. High transverse momentum (p_T) spray of hadronic particles collectively called jets and missing transverse energy due to the weakly interacting nature of the gravitino as it leaves the detector undetected, accompany this decay. The measured photon arrival time at the electromagnetic calorimeter is large (nanoseconds (ns)) because of the inherently long neutralino lifetime and extra distance traveled inside the detector. This combination of jets, missing transverse momentum and delayed photon is a clear signal for a new kind of physics beyond the standard model (SM). An event with the decay of a neutralino, produced in the LHC pp collider would be recorded using the Compact Muon Solenoid (CMS) detector. The CMS detector is located at one of the beam crossing or collision points (also known as Interaction Point (IP)) at Point 5 in Cessy, France. Relying on the excellent timing and energy resolution of Electromagnetic Calorimeter (ECAL) sub detector, of the CMS detector, we can distinguish between high energy photons from NMLLP decay and photons produced in interactions precisely and well described by the SM. Finding such a LL particle would address a lot of important questions in modern physics like: Why do we observe so much matter than anti-matter in our universe? Is there a reason

why particles as currently observed in the SM have very different masses and can be classified to exists in 3 generations? What is the origin and existence of Dark Matter (DM) and what is it made of? Do all fundamental forces behave the same way at some higher energy scale? Answers to these questions will provide a clear understanding and direction towards studying physics beyond the standard model.

We have described in this thesis, a search analysis for delayed photons with results. This description is arranged as follows in the following chapters:

- Chapter 1 gives an introduction and general outline of this thesis.
- In Chapter 2, we give a brief description of the current standard model highlighting its strengths and weaknesses. We also describe *supersymmetric* models which are theoretical extensions beyond the standard model (BSM) embedded with the prediction of NMLLP. The physics of long-lived particle is also described. This chapter also presents compelling hints from theory, experiment as well as cosmological observation supporting the existence of NMLLPs which motivates our search. The phenomenology of NMLLP in *gauge mediating supersymmetric* models is used as a benchmark model in our search. Results from previous search analysis are also presented.
- Chapter 3, describes the experimental setup particularly the LHC collider and CMS detector giving detail description of its sub-detectors emphasizing on those which have been used in our search analysis.
- Timing reconstruction and calibration is described in chapter 4, detailing the method of extraction and calibration procedure used by CMS.
- In chapter 5, the reconstruction of physics objects such as superclusters, photons, jets and missing transverse energy (E_T^{miss}) according the CMS standards is described here. The presence of anomalous signals in the electromagnetic calorimeter is also mentioned.
- The search analysis is described in chapter 6 detailing triggers used, dataset, choice of observables, event selection and background estimation techniques used. The

result of the search is also presented here. Sources of systematic and quantification considered in this experiment are also described.

- Chapter 7 presents the statistical analysis and methods used providing clear meaning of p -values as used in this search analysis.
- Using the minimal *Gauge Mediating Supersymmetric Model* (mGMSB) with *Snowmass Signal Point 8* (SPS8) as our benchmark model, chapter 8 provides an interpretation of our results in terms of exclusion regions reached by our analysis. Possible improvement for future analysis is briefly mentioned.
- In chapter 9, we present our conclusion from performing the search for delayed photons.

Chapter 2

Model and Phenomenology of Long-Lived Particles

2.1 The Standard Model of Particle Physics

The Standard Model (SM) provides a thorough and experimentally valid mathematical description of the fundamental constituents of baryonic matter and its interactions (except gravity) of our universe. Predictions using the SM agree with most of the available experimental data with unmatched precision. However, there are some theoretical and experimental difficulties with the model, such as, the observational evidence for the existence of Dark Matter (DM) in gravitational lensing experiments, the experimental evidence for neutrino oscillation and neutrino masses and gravitational interactions. These observations cannot be explained using the SM. As a result, it is believed that the SM could be the lower energy extension of a more general model. A candidate mathematical model which extends the SM providing possible explanation for these observations is *supersymmetry*. In the next section, we briefly describe the SM highlighting its major components, its strengths and some of its limitations.

2.1.1 Main Components of the SM

Mass, Charge, Spin and Lifetime can be used to identify and categorize fundamental particles of nature. *Spin* is an *internal quantum number* i.e a non-spatial unlike mass

and charge. A particle's spin is expressed in units of $n\hbar$, where n can be *integer* or *half-integer*. Half-integer spin ($\frac{1}{2}, \frac{3}{2}, \dots \times \hbar$) particles obey a *Fermi-Dirac* statistics. These are called *fermions*. No two identical fermions can occupy the same quantum state. While integer spin particles ($0, 1, 2, \dots \times \hbar$) obey *Bose-Einstein* statistics. These are called *Bosons*. Any number of bosons can occupy a given quantum state. Particles also have their *Anti-particles* which have the same mass and spin as the particle but have opposite charge. Particles and anti-particles can be massive or massless and charged or neutral. Fermions are the fundamental building blocks of the material or matter in our universe while bosons help mediate interactions between fermions. No spin = $0\hbar$ particle had ever been experimentally observed prior to the 4th of July 2012 when the *Higgs* boson which is a favorable candidate for the first spin-0 particle was observed,[1]. The Higgs boson is responsible for providing mass to both fermions and bosons. Its discovery completes the SM. From an elementary view point, it is not unreasonable to classify the present and possibly future fundamental particles describing our universe using a spin set, S , given as:

$$S = \{s = (\dots, 0, \frac{1}{2}, 1, \frac{3}{2}, 2, \dots) \cdot \hbar\}$$

where s is the spin of a particle and \hbar is the fundamental *Planck* constant. Our present and possibly future understanding of the universe can thus be summarize as:

- $S = \frac{1}{2}\hbar$ Particles which make up all the matter in our universe.
- $S = 1\hbar$ Mediating particles for gauge interactions.
- $S = 0\hbar$ The fundamental particle responsible for giving mass to other particles.
- $S = 2\hbar$ Mediator for gravitational interactions (might be gauged).
- $S = \frac{3}{2}\hbar$ Particles which make up **Dark Matter?**

However, a subset of the above set with particle spins, $s = \{0, \frac{1}{2}, 1\} \hbar$ very precisely describes only $\approx 4\%$ of the entire universe using the mathematical understanding provided by SM. This mathematical framework is a *relativistic quantum field theory* in which particles are represented as *quantum fields* and their dynamics and interaction with other particles can be expressed using a mathematical functions called the *Lagrangian density*,

\mathcal{L} . The Lagrangian density describes the dynamics of fermions, bosons and their interactions with the Higgs boson. Fermions and bosons obtain their mass interacting with the Higgs boson through a process fundamental to the SM called the *Higgs Mechanism*. In our brief description of the SM, we have divided it into the following sections:

- **Fermions:** All of visible matter is described using fermion fields.
- **Interactions:** Fermions interact either through electromagnetic, weak and strong interactions with vector bosons mediating those interactions. An interaction is described by a given symmetry.
- **Spontaneous Symmetry Breaking or Higgs Mechanism:** Fermions originally have no mass. They get their mass by interacting with the Higgs field through a process known as *Higgs mechanism*. New states or particles of matter can be formed from mixing other states or fermions.

Fermions

The *Dirac* equation given as:

$$\mathcal{L}(\bar{\psi}, \psi, G^\mu) = \bar{\psi} (i\gamma^\mu \mathcal{D}_\mu - m) \psi \quad (2.1)$$

describes fermion dynamics and interaction. Fermions exist in *pairs* known as *doublets* in the SM as either leptons (ℓ) or quarks (q) and come in 3 *generations*. The SM gives no explanation for the existence of only 3 generations. Leptons do participate in electromagnetic and weak interactions but not in strong interactions while quarks participate in all three interactions. In the SM, leptons have integer charge while quarks have fractional charge. The 3 generation of quarks and leptons also known as *flavors* are arranged in a mass hierarchy with the third generation being the heaviest. The second and third generation being meta stable can disintegrate or *decay* into the first generation through weak interactions. A lepton pair or doublet consists of a particular lepton flavor and its corresponding neutral neutrino flavor type. For example, an **electron** (e) and its corresponding electron **neutrino** (ν_e) make the first generation pair, (e, ν_e). Other lepton flavors include **muon** (μ) and **muon neutrino** (ν_μ) pair (μ, ν_μ) and **tau** (τ) and **tau neutrino** (ν_τ) pair (τ, ν_τ). In the SM, neutrinos are described as

having no mass, however, numerous experiments have confirmed that neutrinos have a very tiny mass (order of electronvolts (eV)) and can oscillate from one flavor or generation into another over sufficiently large distances.

On the other hand, a first generation pair of quarks consists of an “*up-type*” and a “*down-type*” quark. In addition to the electric charge, quarks also carry a *color* charge and as a result can equally participate in strong interactions. *Up-type* quarks like **up** (u), **charm** (c), **top** (t) have charge of $+\frac{2}{3}$ and *down-type* quarks such as **down** (d), **strange** (s), **bottom** (b) have a charge of $-\frac{1}{3}$. Charges are expressed in units of elementary charge e. Quark doublets include (u, d) as the first generation and (c, s) and (t, b) as second and third generations respectively. Quarks do not exist as free particles in nature and are found in bound states as composite particles like *protons* and *neutrons* collectively called *hadrons*. The distributions of these quarks inside hadrons can be modeled using *parton distribution functions* (PDF) which depends on the fraction of momentum of the given hadron carried by each quark.

One can distinguish between “Left” from the “Right” handed fermions based on the nature of their interaction with electroweak bosons. Since most particles in the second and third generation are meta-stable, it is possible to describe all visible matter in our universe using only one generation of leptons, **electron** and the **electron neutrino** (e, ν) and one generation of quarks, **up-quark** and **down quark** (u,d).

Interactions

Fermions interaction is mediated by particles called vector *bosons*; i.e $s = 1\hbar$. The SM describes three different forces and their carriers. The *electromagnetic force* described using the mathematical frame work of *Quantum Electrodynamics* (QED). Its force carrier is a massless vector boson called the *photon* (γ). The two nuclear forces which include the *weak force* which was developed later in the 1960s in a combined *electro-weak* framework of *Electro-Weak Field Theory* independently developed by Sidney Glashow, Abdus Salam and Steven Weinberg [2] have 3 massive vector bosons W^\pm , Z^0 discovered at CERN in 1983 as its force-mediating particles. Finally, the *strong force* described using the frame work of *Quantum Chromodynamics* (QCD), is mediated by massless *gluons* (g). The strong force is not unified with the other two forces. It remains an open question whether at a much higher energy scale, all these forces unify and

start behaving as a single force. It is also understood(theoretically) that *gravitational* interaction is mediated by a spin-2 particle called the *graviton*. There are experiments searching for gravitons.

At the heart of the formulation of the SM, is the concept of *symmetry* and *conserved quantum numbers*. Symmetry is the invariance of the dynamics (Lagrangian density, \mathcal{L}), under a given transformation and a conserved quantum number is the conserved quantity associated with that transformation. In the SM, these transformations are called *local gauge* transformations or symmetry groups. The gauge transformations present in the SM can be written as:

$$SU(3)_C \otimes SU(2)_L \otimes U(1)_Y \quad (2.2)$$

$SU(3)_C$ is the local gauge transformation for strong interactions. Its conserved quantum number is the *color* (C) charge which allows gluons to couple with quarks. There are $3^2 - 1 = 8$ colorless and massless self interacting gluons and three different color type quarks for each quark flavor. There are eight gluons because of the $SU(3)$ group symmetry. Anti-quarks carry opposite color charges. As previously mentioned, no free quark has been observed, rather, quarks exist in nature in the form of bound states called *hadrons*. Hadrons are made up of 2 or 3 quarks as in the case of pions and protons or neutrons respectively. Recent experiments have observe bound states consisting of 4 quarks,[3], which remain consistent with the nature of strong interactions. $SU(2)_L \otimes U(1)_Y$ is the gauge transformation group with conserved quantum number, *weak isospin* (T_3), necessary for the electroweak interaction. Corresponding to the $SU(2) \otimes U(1)$ gauge group, there are $2^2 - 1 + 1 = 4$ massless gauge bosons, $W_\mu^{1,2,3}, B_\mu$, capable of mixing with each other to form the physical electroweak bosons as charged W^\mp and neutral Z^0 and γ . The W^\mp and Z^0 through the spontaneous breaking of the electro-weak symmetry, obtain their mass and are the physical mass states ensuring quark flavor transformations. These bosons couple using the “charge” of the weak interaction called *weak isospin*, T_3 , and the *hypercharge*, Y , to matter fields. The W^\mp only interacts with **left-handed** fermions and **right-handed** anti-fermions. This leads to a phenomenon called *parity* violation. The electromagnetic charge, Q , is the result of a combination of the third component of the weak isospin, T_3 and the hyper charge,

Y , through the following relation:

$$Q = T_3 + \frac{Y}{2} \quad (2.3)$$

Left handed fermions have $T_3 = \pm \frac{1}{2}$ and are represented as *multiplets* or in this case of the SM, isospin *doublets*, while, right-handed fermions have $T^3 = 0$ and are isospin *singlets*. We summarize fundamental particles as described by the SM in Table 2.1 showing their representations as *multiplets*(*doublets*, *triplets*, etc) and quantum numbers.

Infact, the $SU(2)_L \otimes U(1)_Y$ guage group is a combination of two symmetry groups with coupling strengths g and g' connected to the electric charge of each fermion as $e = g \sin \theta_w = g' \cos \theta_w$.

The angle, θ_w , is the *Weinberg angle*, $\sin^2 \theta_w \approx 0.231$ is not predicted by the SM but measured from experiments. Gauge bosons can rotate from their *weak* eigen states to physically observed states using this angle.

$$W^\mp_\mu = \frac{W_\mu^1 \mp i W_\mu^2}{\sqrt{2}}, \quad \begin{pmatrix} A_\mu \\ Z_\mu \end{pmatrix} = \begin{pmatrix} \cos \theta_w & \sin \theta_w \\ -\sin \theta_w & \cos \theta_w \end{pmatrix} \begin{pmatrix} B_\mu \\ W_\mu^3 \end{pmatrix} \quad (2.4)$$

This angle also allows for the transformation of a quark from one flavor into another through the W^\mp bosons. On the contrary, according to the SM, such flavor transformation could be possible with leptons but does not lead to any possible observable effects as neutrinos are considered massless in the SM. On the contrary, recent neutrino experiments have proven otherwise as they observed mixing between different neutrino types indicating neutrinos do have mass. The transformation of quarks into different flavors is a typical interaction happening inside the core of our sun as in a nuclear reactor in the decay of neutrons to protons. The complete transformation of all quark flavors is described by the *Cabibbo-Kobayashi-Maskawa* (CKM) 3 by 3 matrix whose elements are parameters only measured from experiments and not predicted by the SM.

Particle and Their Gauge Group Representation

Particle Name(Symbol)	Spin	Multiplet	$SU(3)_C \otimes SU(2)_L \otimes U(1)_Y$
Quarks (Q)	$1/2$	$(\mathbf{u}_L, \mathbf{d}_L)$	$(\mathbf{3}, \mathbf{2}, \frac{1}{6})$
$\bar{\mathbf{u}}$	$1/2$	\mathbf{u}_R^\dagger	$(\bar{\mathbf{3}}, \mathbf{1}, -\frac{2}{3})$
$\bar{\mathbf{d}}$	$1/2$	\mathbf{d}_R^\dagger	$(\bar{\mathbf{3}}, \mathbf{1}, \frac{1}{3})$
$(\times 3 \text{ families})$			
Leptons(L)	$1/2$	(ν, \mathbf{e}_L)	$(\mathbf{1}, \mathbf{2}, -\frac{1}{2})$
$\bar{\mathbf{e}}$	$1/2$	\mathbf{e}_R^\dagger	$(\bar{\mathbf{1}}, \mathbf{1}, 1)$
$(\times 3 \text{ families})$			
Higgs (\mathbf{H}_u)	0	$(\tilde{\mathbf{H}}^+_u, \tilde{\mathbf{H}}^0_u)$	$(\mathbf{1}, \mathbf{2}, +\frac{1}{2})$
Higgs(\mathbf{H}_d)	0	$(\tilde{\mathbf{H}}^+_d, \tilde{\mathbf{H}}^-_d)$	$(\mathbf{1}, \mathbf{2}, -\frac{1}{2})$
Force Carriers			
Gluons	1	\mathbf{g}	$(\mathbf{8}, \mathbf{1}, 0)$
(Strong Force)			
W bosons	1	\mathbf{W}^\pm	$(\mathbf{1}, \mathbf{3}, 0)$
B boson	1	\mathbf{B}^0	$(\mathbf{1}, \mathbf{1}, 0)$
(Electro-Weak Force)			

Table 2.1: SM particles and their gauge multiplets(representation) with quantum numbers. the numbers for example $(\mathbf{3}, \mathbf{2}, \frac{1}{6})$ means (*triplet, doublet, $Y = 1/6$*) representations.

2.1.2 Spontaneous Symmetry Breaking

It is the spontaneous breaking of the gauge transformation group:

$$SU(3)_C \otimes SU(2)_L \otimes U(1)_Y \xrightarrow{SSB \text{ into}} SU(3)_C \otimes U(1)_{QED} \quad (2.5)$$

Early attempts prior to the 1960s to construct a gauge theory of weak interactions failed because the gauge bosons were massless while experimental evidence proved otherwise. The Higgs (or Higgs-Brout-Englert) mechanism ,[4], is archived by introducing a complex weak isospin *scalar doublet*, ϕ , i.e spin $s = 0\hbar$.

During this process, the $SU(2)_L \otimes U(1)_Y$ symmetry is spontaneously broken into a $U(1)$ symmetry which describes electromagnetic interaction. Figure 2.1 shows a picture of the potential of the spin-0 complex Higgs field.

The choice for the minimum value of the potential, $|\phi_0| = \sqrt{\frac{-\mu^2}{\lambda}} = \nu$, where $\mu^2 < 0$ and $\lambda > 0$, as parameters, is to spontaneously break the $SU(2)_L \otimes U(1)_Y$ symmetry into $U(1)$ symmetry. In this process, both matter and gauge bosons except the photon obtain their mass. This process is referred to as *Higgs-Brout-Englert mechanism* or *Higgs mechanism*.

Quarks and leptons through their interaction with the Higgs field obtain their mass. A fermion's mass, m_f , is proportional to the strength of its interaction (Yukawa coupling λ_f) with the Higgs field. Electro-weak interaction mediating gauge bosons, Z^0 and W^\pm obtain their mass m_Z and m_{W^\pm} respectively, by engulfing or “*eating*” the available massless components (*Nambu-Goldstone bosons*) of the complex Higgs doublet. From the four scalar fields(complex Higgs doublet), only a physically massive *Higgs boson* remains.

$$m_f = \lambda_f \frac{\nu}{\sqrt{2}}, \quad \frac{m_{W^\pm}}{m_Z} = \frac{\frac{1}{2}\nu g}{\frac{1}{2}\nu \sqrt{g^2 + g'^2}} = \cos \theta_w \quad (2.6)$$

The search for the Higgs boson was one of the purpose for building the large hadron collider at CERN. The discovery of the Higgs candidate scalar boson through its decay into two photons, $H \rightarrow \gamma\gamma$, and a pair of Z bosons, $H \rightarrow ZZ$, was presented to the public on June 04, 2012. Its mass measured was $m_H = 125 \pm 0.21 \text{ GeV}/c^2$.

It is important to note that there is no fundamental reason given by the SM why there should be only one type of the Higgs field to which all fermions couple to obtain their mass nor any prediction from the SM for the choice of parameters. There are other models such as supersymmetry, which allows for the possibility of more than one Higgs field. In Figure 2.2, we show a complete summary of particles and their interactions as described by the SM.

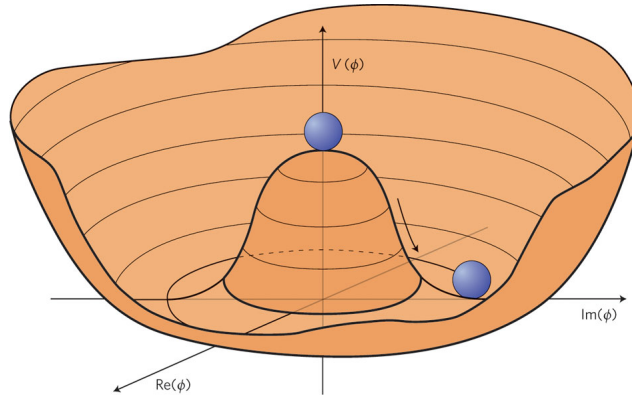


Figure 2.1: Higgs boson “Mexican hat” potential, $V(\phi^*\phi) = \mu^2(\phi^*\phi) + \lambda(\phi^*\phi)^2$, which leads to spontaneous symmetry breaking with choice of parameters $\mu^2 < 0$, $\lambda > 0$.

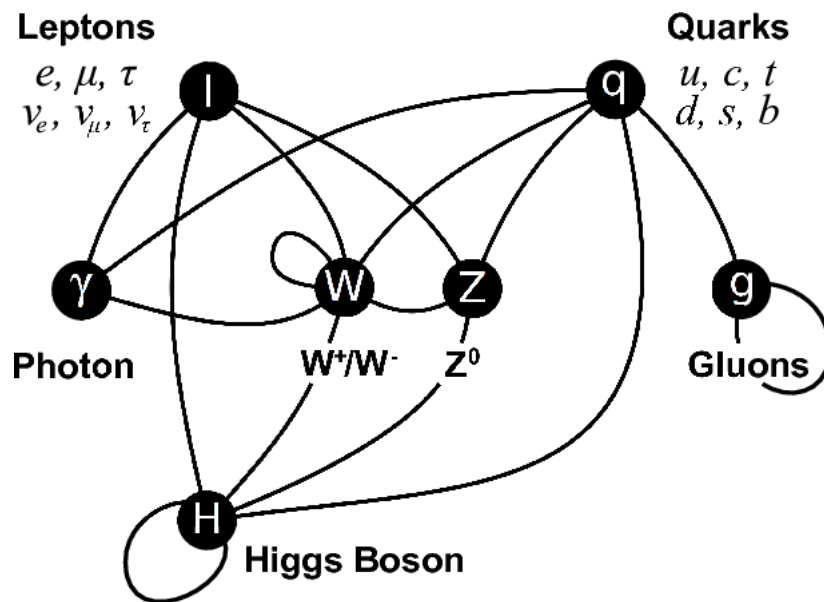


Figure 2.2: SM particles and their interactions with vector bosons as mediators.

2.1.3 Limitations of the Standard Model

Although numerous experiments support the SM in its description of particle properties with unmatched precision, there are many unanswered questions by the SM. We provide a summary below of those of our interest.

- **General Formalism**

Many important parameters like particle masses, Weinberg angle, the CKM matrix elements for example cannot not be derived from the SM. These are measured from experiments. Why only 3 generations of particles? Why multiplet structure of fields representation in the SM? These are questions to which the SM provides no answer.

- **Astrophysical**

Why is there so much matter than anti-matter in the universe? *Cosmic Microwave Background* (CMB) and the *Wilkinson Microwave Anisotropy Probe* (WMAP) experimental results indicate the presence of excess matter which does not interact with light called *Dark Matter* (DM) and *Dark Energy* (DE). DE is responsible for an increase energy density causing rapid acceleration expansion of the universe. The nature of DM and DE and such observations cannot be explained using the current SM.

- **Theory**

SM description of nature does not include gravitational interactions. Observation of SM coupling constants varying with energy begs the question of whether at some higher energy scale, all the weak, strong and electromagnetic coupling constants behave as one i.e unify as a single coupling constant. If possible, at what energy scale does this force unification occur?

- **Mass Hierarchy or Naturalness**

Particle masses ranges from neutrino masses, a few eV to the top particle's mass of 173 GeV/c². The SM does not provide and answer for this mass hierarchy. To some physicist, the energy gap between the electro-weak symmetry breaking energy scale (≈ 246 GeV) and the Planck energy scale (reduced Planck mass, $M_p = 10^{18}$ GeV) seems unnatural.

2.2 Beyond Standard Model Physics

The SM predictions of the value of the Higgs boson's mass recommend additional contributions from *quantum fluctuations* (higher order or loop corrections) which are very large (can as well be infinite). However, the observed experimentally measured value of the Higgs mass ($m_H \approx 125$ GeV). This unobserved large corrections to the experimentally measured value requires some understanding. A possible explanation is that these various contributions cancel on average producing a net zero effect on the true Higgs mass such that the physically observed mass is as measured. If such cancellation is a true phenomenon in nature, then it is only logical to inquire the origin of this cancellations. Obviously this cannot be understood within the frame work of the SM.

Consequently, theories beyond the SM like *supersymmetry* provide a natural understanding of how these various contributions cancel on average arriving at the physically observed and measured Higgs mass. To expand further, the mass of a particle can be expressed as

$$m_{\text{physical}}^2 = m_{\text{bare}}^2 + \delta m_1^2 \quad (2.7)$$

where m_{physical}^2 is the physically measured mass of the Higgs boson, m_{bare}^2 is the true universe given mass of the particle which cannot be calculated or measured. δm_1^2 are corrections from quantum fluctuations to the true mass which can be calculated. Using the measured mass and the calculated quantum corrections, one can obtain the true Higgs mass. These contributions from quantum fluctuations can arise from both bosons and fermions. Since the Higgs boson can interact (by coupling) with every particle through interactions of the general form $\lambda_f H \bar{f} f$ for fermions and $\lambda_S |H|^2 S^2$ for scalar or bosons; with λ_f and λ_S representing the coupling constants which need not be equal. The Feynman diagrams in 2.3 represents a few of such quantum fluctuations with both fermion and boson contributions computed as:

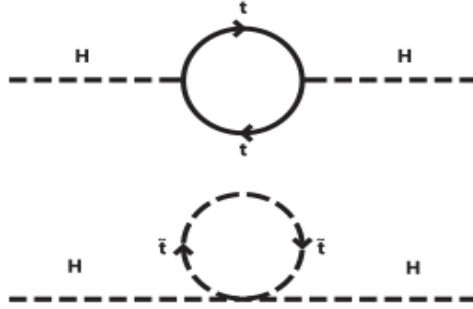


Figure 2.3: Higgs self energy diagrams showing how the higgs boson mass is computed from both Higgs field and supersymmetric partner particle contributions.

$$\delta m_{1,f}^2 = \frac{1}{16\pi^2} |\lambda_f|^2 \left(-2\Lambda^2 + 6m_f^2 \ln \left(\frac{\Lambda}{m_f} \right) + \dots \right) \quad (2.8)$$

$$\delta m_{1,S}^2 = \frac{1}{16\pi^2} |\lambda_S|^2 \left(\Lambda^2 - 2m_S^2 \ln \left(\frac{\Lambda}{m_S} \right) + \dots \right) \quad (2.9)$$

Λ is some *cut-off* energy scale where another kind of physics interaction like gravity at a much higher energy scale is needed to regulate the low energy behavior of the SM. Λ could be the reduced Planck scale(10^{18} GeV). A quick observation from this calculations is that; first, corrections to the higgs bare mass, m_{bare}^2 are not proportional to the Higgs mass. Second, these corrections are of the order of $\approx 10^{36}$ GeV 2 bringing positive and negative contributions from fermions or scalar bosons respectively. Even with these corrections to the true Higgs mass, the measured (physical) Higgs mass squared, $m_{H,\text{physical}}^2$, is of the order $\approx 10^4$ GeV 2 . Since the true Higgs mass, $m_{H,\text{bare}}^2$, is never measured or known, an agreement between these quantum fluctuation contributions and physical Higgs mass is realized if only the true Higgs mass, $m_{H,\text{bare}}^2$, is *fine-tuned* with a precision of about 1 in 10^{17} . This enormous fine-tuning is considered a fundamental issue of not enough understanding of the Higgs mechanism of the SM and is considered *unnatural*. On the other hand, in supersymmetry, the fermion one loop quantum correction which comes with an opposite sign to the scalar quantum fluctuation corrections and $\lambda_f = \lambda_S$, there is a complete cancellation and this discrepancy of the unobserved effects of these quantum fluctuations to the $m_{H,\text{bare}}^2$ in the $m_{H,\text{physical}}^2$ is understood.

In addition to explaining the origin of this perceived *fine-tuning* issue, supersymmetry also provides a natural framework for the unification of fundamental forces, not possible in the SM. If the SM is believed to be an incomplete and low energy description of nature of a possible parent and more fundamental theory like supersymmetry, then one would expect that the symmetry groups of the SM be a subset of some larger parent group, \mathcal{G} ; i.e $SU(3)_C \otimes SU(2)_L \otimes U(1)_Y \subset \mathcal{G}$. In supersymmetry, This unification of forces or couplings of electromagnetic, weak and strong interactions occur at the *Grand Unified Energy* (GUT) energy scale of $\approx 10^{15}$ GeV [11].

2.2.1 Supersymmetry

In relativistic Quantum Field Theory (QFT), the idea of symmetry or group theory is used to provide a better understanding of fundamental particles and their properties. These symmetries belong to two broad categories: space-time symmetries known as Poincaré(i.e rotation and translation) symmetries and gauge (such as $SU(3)_C \otimes SU(2)_L \otimes U(1)_Y$ with quantum numbers; color, weak and hypercharge respectively of the SM) symmetries. With the SM viewed as a low energy version of a more large and unified theory, it was believed that combining these two classes of symmetries into one big class of symmetry could lead the way towards the development of this unified theory. However, Coleman and Mandula[12], in their so-called “*no-go*” theorem in 1967 showed that pursuing the approach of *direct product* of the two super groups was not possible. The challenge was finding a scenario where the generators of both space-time P^μ , $M^{\mu\nu}$ and gauge groups T^a , do not commute with each other; i.e $[M^{\mu\nu}, T^a] \neq 0$ and yet remains a direct product of both symmetry groups, considering that the direct product of these groups do commute; i.e $[P^\mu, T^a] = [M^{\mu\nu}, T^a] = 0$.

This *no-go* theorem prevents the possibility of finding a parent group where its generators are constructed from *Lorentz* tensors. Thus, only symmetries generated from *spinoral* (particle’s spin) charges instead of *tensorial* (space-time) charges were possible. In 1975, Haag, Lapuszanski and Sohnius [13] found such a group theorem known as the *Haag-Lapuszanski-Sohnius* theorem with its corresponding generator algebra called the *Lie-superalgebra* or the *supersymmetry algebra*. This supersymmetry algebra extended the commutative aspect of the Poincaré algebra to include *anticommuting* symmetry generators.

Lie-superalgebra generators, Q_i , $i = 1, \dots, N$, where N is the number of supersymmetry generators, anti-commute with the group and space-time generators. Supersymmetry is a well developed and advanced branch in theoretical physics where the number of supersymmetry generators can be any number. However, this thesis only considers the case where there is only one generator of supersymmetry; i.e $N = 1$. This is the minimal version of supersymmetry. The generators $Q_1 \equiv Q^\alpha$, where $\alpha = 1, 2$ is labeling *Weyl* or *two spinor* components, and its hermitian conjugate, \bar{Q}_α , must satisfy the relations

given in equation 2.10.

$$\{Q_\alpha, \bar{Q}_\beta\} = 2(\gamma^\mu)_{\alpha\beta} P^\mu, \quad [Q_\alpha, P^\mu] = 0, \quad [Q_\alpha, M^{\mu\nu}] = \frac{1}{2} (\Sigma^{\mu\nu})_\alpha^\beta Q_\beta \quad (2.10)$$

Where $\{\gamma^\mu, \gamma^\nu\} = 2g^{\mu\nu}$ and $\Sigma^{\mu\nu} = \frac{i}{2} [\gamma^\mu, \gamma^\nu]$. These relations in equation 2.10 reveal two very fundamental consequences of supersymmetry:

- Particles in a given state (*supermultiplet*) have the same mass but differ in their spin by half \hbar unit.
- In every irreducible representation of supersymmetry, there is an equal number of fermionic and bosonic degrees of freedom.

Thus, supersymmetry is the symmetry which transforms particles from one spin into another with the same mass. As a consequence, supersymmetry generators transform fermions into bosons and bosons into fermions with the same mass.

$$Q|\text{Fermion}\rangle = |\text{Boson}\rangle, \quad Q|\text{Boson}\rangle = |\text{Fermion}\rangle \quad (2.11)$$

This reveals that, in supersymmetry, every particle has a supersymmetric partner with the same mass lying in the same representation or supermultiplets. These supermultiplets are either *Chiral*, *Vector* or *Gravity* multiplets. The minimal supersymmetric extension of SM uses Chiral and Vector supermultiplets. The following table shows the different supermultiplets as encountered in supersymmetry.

Supermultiplets	Spin in SM,	Spin in Supersymmetry
<i>Chiral</i>	0	$\frac{1}{2}$
<i>Chiral</i>	$\frac{1}{2}$	0
<i>Vector</i>	1	$\frac{1}{2}$
<i>Gravity</i>	2	$\frac{3}{2}$

Table 2.2: Supermultiplets and particle spin in SM and Supersymmetry.

In addition to an algebraic approach to supersymmetry described so far, in order to build models (supersymmetric Lagrangians) and make predictions, we return to the idea of fields as used in supersymmetry. Supersymmetric fields are called *superfields* (

proposed and realized by Abdus Salam and Strathdee [14, 15]) are fields defined on a superspace; an ordinary Minkowski space-time, x^μ and four anti-commuting *Grassmann* numbers, θ . More on this can be seen in [15]. These superfields are operator-valued functions, Φ , on a superspace represented by, $\Phi(x^\mu, \theta, \bar{\theta})$. Its components consist of ordinary scalar fields (real or complex), Lorentz vector fields and Left-handed or Right-Handed Weyl(2 degrees of freedom) spinor fields, $\Phi(x^\mu, \theta, \bar{\theta}) \supset (\phi, \psi, A_\mu, F)$. Table 2.3 shows an example of the components which make up the superfield (or supermultiplets) with each component representing a SM particle and its super partner with the same mass. Only the Chiral and Vector superfields are used in constructing the minimal supersymmetric version of standard model

Superfields or supermultiplets	Components
<i>Chiral</i>	(ψ, ϕ, F)
<i>Vector</i>	(A_μ, λ, D)
<i>Gravity</i>	$(G_{\mu\nu}, \dots)$

Table 2.3: Supermultiplets and components in Supersymmetry.

2.2.2 Minimal Supersymmetric Standard Model

The Minimal Supersymmetric Standard Model (MSSM) is an extension of the SM to include supersymmetric particles. Supersymmetric particles have almost the same name as SM particles with the only difference being the addition of an s in front of the SM particles's name e.g a *selectron* is the supersymmetric particle of an electron, *squarks* are the supersymmetric particles of SM quarks. There are exceptions to this nomenclature. In order for supersymmetry (SUSY) predictions to be agreement with observations from experiments, SUSY must be realized as a broken symmetry in nature. The type of SUSY which is broken allows for different models with different phenomenology to be expected from predictions made by these models. If the SUSY breaking is communicated through gravitational interaction, such class of models are called *Gravity Breaking SUSY Models* (mSUGRA) with instead of the 19 fundamental parameters as in the SM, only 6 parameters are needed to explain all our observed particle phenomenology. If instead SUSY breaking is purely because of gauge interactions, this class of models are

Gauge Mediated Supersymmetry Breaking (GMSB) models with only 5 fundamental parameters. Other SUSY models like Anomalous Supersymmetry Breaking (ASB) having 6 parameters have been proposed.

This thesis only discusses GMSB models as they have favorable theoretical benefits like being flavor blind as well as predict the existence of long lived particles which opens up a whole new technique to search for supersymmetric particles in hadron collider or related particle physics experiments. Table 2.4 and 2.5 shows SM particles and their supersymmetric counterparts as understood through the MSSM framework.

Particle Names	Symbol	spin 0	spin 1/2	$SU(3)_C \otimes SU(2)_L \otimes U(1)_Y$
squarks, quarks ($\times 3$ families)	Q	$(\tilde{u}_L, \tilde{d}_L)$	(u_L, d_L)	$(\mathbf{3}, \mathbf{2}, \frac{1}{6})$
	\bar{u}	\tilde{u}_R^*	u_R^\dagger	$(\bar{\mathbf{3}}, \mathbf{1}, -\frac{2}{3})$
	\bar{d}	\tilde{d}_R^*	d_R^\dagger	$(\bar{\mathbf{3}}, \mathbf{1}, \frac{1}{3})$
sleptons, leptons ($\times 3$ families)	L	$(\tilde{\nu}, \tilde{e}_L)$	(ν, e_L)	$(\mathbf{1}, \mathbf{2}, -\frac{1}{2})$
	\bar{e}	\tilde{e}_R^*	e_R^\dagger	$(\bar{\mathbf{1}}, \mathbf{1}, 1)$
higgsinos, Higgs	H_u	(H_u^+, H_u°)	$(\tilde{H}_u^+, \tilde{H}_u^\circ)$	$(\mathbf{1}, \mathbf{2}, +\frac{1}{2})$
	H_d	(H_d°, H_d^-)	$(\tilde{H}_d^\circ, \tilde{H}_d^-)$	$(\mathbf{1}, \mathbf{2}, -\frac{1}{2})$

Table 2.4: Chiral supermultiplets and representation in Minimal Supersymmetric SM (MSSM). Super symmetric particles (sparticles) have a $\tilde{\cdot}$ on them. Spin -0 fields are complex scalars while spin-1/2 fields are left-handed two component Weyl fermions.

Particle Names	spin 1/2	spin 0	$SU(3)_C \otimes SU(2)_L \otimes U(1)_Y$
gluino, gluon	\tilde{g}	g	$(\mathbf{8}, \mathbf{1}, 0)$
winos, W bosons	$\tilde{W}^\pm, \tilde{W}^\circ$	W^\pm, W°	$(\mathbf{1}, \mathbf{3}, 0)$
bino, B boson	\tilde{B}°	B°	$(\mathbf{1}, \mathbf{1}, 0)$

Table 2.5: Gauge supermultiplets and representation in Minimal Supersymmetric SM (MSSM). Super symmetric particles (sparticles) have a $\tilde{\cdot}$ on them.

In SUSY, the superpotential which allows for SUSY breaking defines the phenomenology and particle mass spectrum in any given SUSY model. In MSSM, this superpotential

is given as seen in eqn 2.12.

$$W_{\text{mssm}} = \bar{u} \mathbf{y_u} \mathcal{Q} H_u - \bar{d} \mathbf{y_d} \mathcal{Q} H_d - \bar{e} \mathbf{y_e} \mathcal{L} H_d - \mu H_d H_u \quad (2.12)$$

Where the objects H_u , H_d , \mathcal{Q} , \mathcal{L} , \bar{u} , \bar{d} , \bar{e} are Chiral superfields corresponding to the Chiral supermultiplets given in table 2.3 above. The dimensionless couplings $\mathbf{y_u}, \mathbf{y_d}, \mathbf{y_e}$ are 3×3 matrices known as the Yukawa couplings. rather than a single Higgs double as in the SM, SUSY breaking allows for two Higgs double to be present; H_u and H_d to provide masses to up-type and down-type quarks and leptons. The superpartners of these Higgs particles which are fermions and those of the gauge bosons called *gauginos* mix to produce new neutral and charged fermions called *Neutralinos* and *Charginos* respectively.

R-Parity Symmetry

In MSSM, a combination of baryon (B) and lepton number (L) symmetries is combined to give a fundamental symmetry called *Matter Parity* or *R-Parity*. From a multiplicative combination of B and L numbers, we get R-parity expressed as:

$$R_P = (-1)^{3(B-L)+2S} \quad (2.13)$$

where S is the spin of the particle. R-parity is a conserved quantum number which originates from a discrete Z_2 -symmetry [11]. R-parity symmetry commutes with supersymmetry. Therefore, particles in a given supermultiplet do not have the same R parity. SM particles like quarks have an even parity $R_P = 1$ while SUSY particles like squarks have odd parity $R_P = -1$. R-parity has important phenomenological consequences such as the following:

- In the decay of SUSY particles, the lightest SUSY particle (LSP) have odd parity $R_P = -1$ and thus are considered absolutely stable. If in addition to being stable, the LSP is neutral an interacts only very weakly with ordinary matter, then it is a good candidate for non-baryonic dark matter as required by cosmology[16].
- Every SUSY particle produced which is not the LSP, will eventually decay into the LSP or an odd number of LSPs.

- SUSY particles can only be produced in pairs in a collider experiment.

Thus in generic SUSY models with minimal particle content, where the superpotential include terms which violate Lepton (L) and baryon (B) numbers; R-parity conservation can be imposed giving rise to *R-parity Conserving* (RPC) models with the LSP stable while R-parity can be violated resulting to *R-parity Violating* (RPV) models where the LSP is unstable and decays to SM particles.

RPC models are those discussed in this thesis as our search is motivated towards the search for neutral stable particles as possible candidates particles for dark matter (DM).

If SUSY is a theory which describes nature, then its prediction of components within the same supermultiplets with the same mass, i.e $m_B = m_F$ is not realistic, since experiments are yet to find a selectron (SUSY partner of electron) with a mass of 0.512 MeV for example. Therefore, SUSY must be realized through a spontaneously broken way. Spontaneous Supersymmetry Breaking (SSB) means the lowest energy state or vacuum expectation value of a scalar field (or auxiliary field as is the case with SUSY) must be non-zero. The type of breaking determines the phenomenology of any given model. We focus on models with gauge interactions responsible for communicating SUSY breaking from a higher energy level to our observable collider experiments energy levels. Gauge Mediated SUSY breaking models (GMBS) can be Pure, General or minimal Gauge Mediation (GGM) depending on the model parameters. The presence of the hadron colider in CERN, has encouraged the development of SUSY models whose predictions are about a few TeV for the mass range of some of these SUSY particles and also the energy scale which the most powerful particle colliders can probe for new particles. These kind of models are called Soft SUSY Breaking models. We would focus on such models in particular the *Snowmass Point and Slopes* (SPS8) [12] models with phenomenology within the reach of the LHC. Soft breaking mean the SUSY breaking terms in the SUSY potential (eqn 2.12) consists of only masses and terms whose couplings have positive mass dimension. This ensures the existence of sparticles with masses around a few TeV where they can possibly be produced at current particle colliders such as the large hadron collider (LHC).

2.2.3 Soft Supersymmetry Breaking

Soft SUSY breaking is such that the spontaneous breaking must be caused by couplings with positive mass dimension and not dimensionless coupling. This allows for the already observed hierarchy between the Electro-Weak energy scale of ≈ 100 GeV and the reduced Planck energy scale $\approx 10^{18}$ GeV. The Lagrangian for soft SUSY breaking terms can be written as thus:

$$\mathcal{L}_{\text{soft}}^{\text{mssm}} = -\frac{1}{2} \left(M_3 \tilde{g} \tilde{g} + M_2 \tilde{W} \tilde{W} + M_1 \tilde{B} \tilde{B} \right) + c.c + \dots \quad (2.14)$$

$$- \left(a_u \tilde{u} \tilde{Q} H_u - a_d \tilde{d} \tilde{Q} H_d - a_e \tilde{e} \tilde{L} H_d + c.c \right) \quad (2.15)$$

where M_1 , M_2 and M_3 are the superpartners of the gauge bosons of the SM symmetry group. They are referred to as the *Bino* (\tilde{B}), *Wino* (\tilde{W}) and *gluinos* (8 gluinos because there are 8 gluons in the SM). I have intentionally omitted scalar mass terms in this Lagrangian, if interested in the rest of the terms see [11].

The SUSY particle mass spectrum for particles within the SPS8 and GGM benchmark models framework after SSB is shown in figure 2.4.

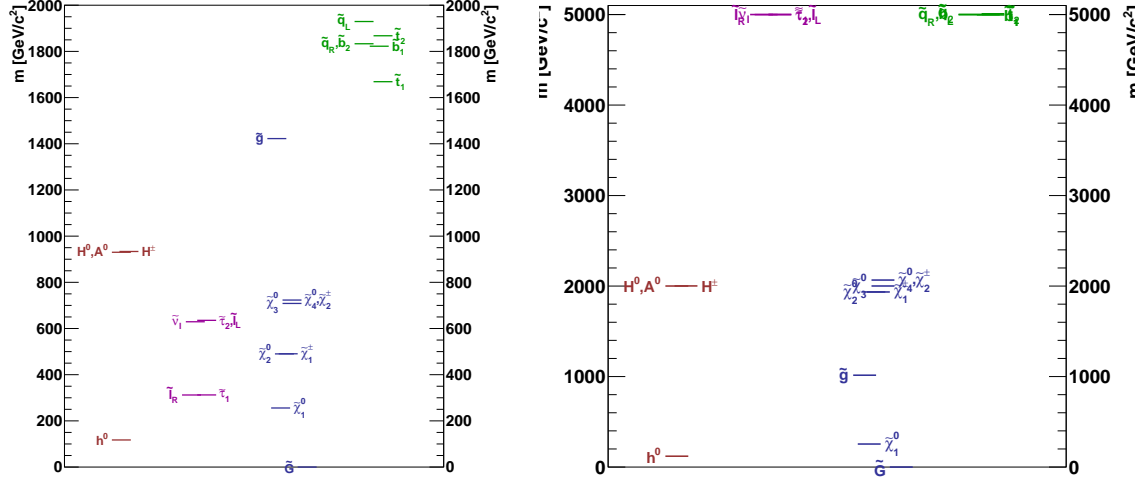


Figure 2.4: SUSY Mass spectra in the mGMSB SPS8 model (left) and GGM Model (right) with mass of gluino ($M_{\tilde{g}} = 1.0$ TeV)

In summary, MSSM in addition to SM particles, contains new particles whose spin (S) differ from their SM counterparts by half-integer. Bosons (fermions) in the

SM have superpartners which are fermions (bosons) respectively. The superpartners of SM fermions are scalars called *sfermions* (\tilde{l}), sneutrinos ($\tilde{\nu}$) and squarks (\tilde{q}) while *gluinos* (\tilde{g}) being fermions are the superpartners of the massless gauge bosons of strong interaction, gluons. The scalar Higgs (2 needed) bosons and the vector gauge bosons of Electro-Weak interaction have fermionic superpartners called *higgsinos*, *Winos* and *Binos*. These can mix to form a pair of mass eigenstates called *charginos* ($\tilde{\chi}_j^\pm, j = 1, 2$) i.e $\tilde{\chi}_{1,2}^\pm$ is from mixing $\tilde{W}^+, \tilde{W}^-, \tilde{H}^+, \tilde{H}^-$ and a quartet of mass eigenstates called *neutralinos* ($\tilde{\chi}_i^0, i = 1, \dots, 4$), i.e $\tilde{\chi}_{1-4}^0$ is from mixing $\tilde{B}^0, \tilde{W}^0, \tilde{h}^0, \tilde{H}^0$.

2.2.4 Gauge Mediated Supersymmetry Breaking and Phenomenology General Model

Constructing a SUSY model requires that the model has gauge group describing the nature of particle interaction, a superpotential, and since the SUSY prediction of equal masses of boson and fermions is not observable, one must provide explicitly the method for spontaneously breaking supersymmetry. We have in the MSSM scenario seen the gauge groups to be exactly those of the SM, the superpotential with soft terms, however, we are yet to understand how supersymmetry is broken. SUSY breaking means that we find the lowest energy state for which the vacuum expectation values of the SUSY generators $Q_\alpha |0\rangle \neq 0$ or $\bar{Q}_\alpha |0\rangle \neq 0$. Since one can always express the Hamiltonian of the system, H in terms of the SUSY generators, SUSY breaking can also be equally expressed as $H|0\rangle \neq 0$. Neglecting spacetime-dependent effects and condensates, SUSY breaking is equivalently expressed as $V|0\rangle \neq 0$, where V is the standard superpotential expressed in terms of the F and D terms. Thus, spontaneously breaking SUSY is equivalent to finding superpotentials for which neither F nor D terms simultaneously vanish in the lowest energy state. Superpotentials with non vanishing F terms are called *O'Raifeartaigh* or F-term SUSY breaking models while those with nonvanishing D terms are called *Fayet-Illiopoulos* or D-term SUSY breaking models. Since in GMSB models, it is the F term which has a non-vanishing lowest energy state expectation value or vacuum expectation, this thesis only considers *O'Raifeartaigh* SUSY breaking models.

In GMSB models, this superpotential is termed the *Hidden Sector* (hidden because it

couples only indirectly and very weakly to our “observable sector” of SM particles and their superpartners) and it is its dynamics which spontaneously breaks supersymmetry. The nature of this breaking is not relevant for phenomenology but rather the “*mediators*” which communicate the effects of this breaking to the superpartners of the SM particles. Therefore, these mediators or agents must couple to this “Hidden Sector” as well as the “observable sector”. This *Messenger fields* in GMSB, have the usual SM gauge interactions and through loops couple with the SM superpartners. As a result MSSM particles (gauginos and sfermions) obtain SUSY breaking masses referred to as *soft terms* through loop level interactions. This procedure allows for the observed mass and energy scale hierarchy is maintained. The mass of these messenger fields, M_{mess} , along with $\langle F \rangle$ defines the energy scale at which supersymmetry breaking is felt at the MSSM energy scale. If $M_{mess} \ll M_{Planck}$, $M_{Planck} \approx 10^{19} \text{ GeV}$, then supersymmetry breaking occurs at a much lower energy scale instead at the Planck energy scale where gravitational interactions become very significant and the effects of the breaking is first felt by these Messenger fields and later communicated to the observable sector through SM gauge interactions. In terms of energy scales, the picture is such that spontaneous supersymmetry breaking occurs at an energy scale, $\langle F \rangle$ which we denote as \mathbf{F} , for simplicity. This energy scale defines the mass, as seen in equation 2.16, of the *gravitino* which is the supersymmetric partner of gravity mediating particle, the *graviton*. The gravitino has the same quantum number as the Nambu-Goldstone particle, the massless neutral Weyl fermion, the *goldstino*, originating from supersymmetry breaking.

$$m_{3/2} = \frac{\mathbf{F}}{\sqrt{3}M_{Pl}} \quad (2.16)$$

where $M_{Pl} = 1.3 \times 10^{19} \text{ GeV}$.

In GMSB models, the energy scale for which supersymmetry breaking is transmitted to the Hidden sector, \mathbf{F}_s might not be the same as the original or fundamental supersymmetry breaking energy scale, \mathbf{F} . If $\mathbf{F}_s < \mathbf{F}$ then the interaction between the hidden sector and the fundamental SUSY breaking is weak interaction and if $\mathbf{F}_s \approx \mathbf{F}$ and the interaction is strong. It is necessary that this interaction is weak, as in this case GMSB models do not suffer from flavor violating interactions which are not observed in nature. The consequences of this is that one would no longer expect the mass of the

gravitino $m_{3/2}$ to be given as in equation 2.16 but rather suppressed by M_{mess}/M_{Pl} in GMSB models. In this mass spectrum scenario, the gravitino mass can be varied to a very small value only bounded by cosmological results, thus making it the lightest supersymmetric particle (LSP). Spanning the gravitino mass is expressed as a fundamental parameter in GMSB models, C_{grav} which directly determines the lifetime of the next-to-lightest supersymmetry sparticle decaying to the gravitino. We will see more of this ahead. Thus the parameters \mathbf{F}_s and M_{mess} , determines the masses of the gauginos and sfermions of the MSSB in GMSB models.

A minimal GMSB model is one where the messenger sector consists of chiral supermultiplets of leptons and quark with the same quantum numbers $SU(3)_C \times SU(2)_L \times U(1)_Y$ as the SM gauge groups. That is, the messenger fields belong to some $SU(5)$ gauge group. The representations of these messengers fields are given in equation 2.17.

$$\tilde{\ell} \sim (1, 2, 1) \quad \tilde{\ell}' \sim (1, 2^*, -1) \quad (2.17)$$

$$\tilde{q} \sim (3, 1, -\frac{2}{3}) \quad \tilde{q}' \sim (3^*, 1, \frac{2}{3}) \quad (2.18)$$

These messenger fields, via a superpotential as in equation 2.19 of a gauge singlet chiral supermultiplet S , couple with an F-term as in the O’Raifeartaigh model [11].

$$W_{\text{mess}} = \lambda_\ell S \tilde{q} \tilde{q}' + \lambda_q S \tilde{\ell} \tilde{\ell}' \quad (2.19)$$

We thus obtain SUSY breaking by allowing vacuum expectation values (VEV) for both S and its auxiliary component F term as $\langle S \rangle$ and $\langle F_s \rangle = \mathbf{F}_s$, where the \mathbf{F}_s does not have to coincide with \mathbf{F} as mentioned earlier. The parameter representing this non equivalence, C_{grav} is defined as shown in equation 2.20. It is one of the fundamental parameters in GMSB models responsible for the lifetime of NLSP particle.

$$\mathbf{F} = C_{\text{grav}} \cdot \mathbf{F}_s \quad (2.20)$$

This equation indicates that the non-zero VEV for the F term is responsible for fundamental SUSY breaking which is transferred to the messenger particles through radiative interactions as C_{grav} is a dimensionless parameter. Leptons and fermions masses(2.21) of the messenger particles together with their scalar superpartners are obtained from

diagonalizing the mass matrix.

$$m_{\tilde{\ell}\tilde{\ell}'}^2 = |\lambda_\ell \langle S \rangle|^2, \quad m_{\tilde{\ell}\text{scalars}}^2 = |\lambda_\ell \langle S \rangle|^2 \pm |\lambda_\ell \langle F_s \rangle| \quad (2.21)$$

$$m_{\tilde{q}\tilde{q}'}^2 = |\lambda_q \langle S \rangle|^2, \quad m_{\tilde{q}\text{scalars}}^2 = |\lambda_q \langle S \rangle|^2 \pm |\lambda_q \langle F_s \rangle| \quad (2.22)$$

By observing equation 2.21, a general energy scale, \mathbf{M}_{mess} , for messenger particle's masses which is also an additional fundamental parameter in GMSB models can be defined as shown in equation 2.23.

$$\mathbf{M}_{\text{mess}} = (\lambda_q, \lambda_\ell) \langle S \rangle \quad (2.23)$$

A common assumption in GMSB models according to [18, 15] is that $\lambda_q \simeq \lambda_\ell \simeq \lambda$ and so $\mathbf{M}_{\text{mess}} = \lambda \langle S \rangle$. However, in Pure gauge mediated SUSY breaking models (PGGM), $\lambda_q \neq \lambda_\ell$ [19]. In the MSSM sector, gauginos and scalars obtained their mass through one-loop and two-loop level interactions respectively given according to equation 2.24.

$$\mathbf{M}_a = \frac{\alpha_a}{4\pi} N_5 \boldsymbol{\Lambda} \quad (2.24)$$

$$\mathbf{m}_{\phi_i}^2 = 2\boldsymbol{\Lambda}^2 N_5 \sum_{a=1}^3 C_a(i) \left(\frac{\alpha_a}{4\pi}\right)^2 \quad (2.25)$$

where $C_a(i)$ are constants of $O(1)$, α_a are coupling constants and

$$\boldsymbol{\Lambda} = \frac{\mathbf{F}_s}{\lambda \langle S \rangle} = \frac{\mathbf{F}_s}{\mathbf{M}_{\text{mess}}} \quad (2.26)$$

N_5 is an additional parameter in GMSB models, specifying the number of messenger vector-like supermultiplets transforming under $SU(5)$. A motivation for $SU(5)$ is for the unification of gauge couplings at the GUT energy scale ($M_{GUT} \approx 10^{16}$ GeV) which is one of the major predictions of supersymmetry in unifying fundamental forces. N_5 is chosen to be not very large so as to avoid gauge couplings diverging before GUT scale. In the minimal GMSB models such as the SPS8 benchmark working point model $N_5 = 1$.

On the other hand in PGGM models ([19]), gauge and scalar particles have separate

mass definitions (eqn:2.27) since $\lambda_q \neq \lambda_\ell$.

$$\Lambda_G = \frac{F_s}{\lambda_q \langle S \rangle} \quad (2.27)$$

$$\Lambda_S = \frac{F_s}{\lambda_\ell \langle S \rangle} \quad (2.28)$$

Λ is the energy scale defining SUSY breaking at the MSSM level. It is known as the *effective supersymmetry breaking scale* and determines the mass spectrum of gauginos and scalars in the MSSM. Λ as defined in equation 2.26 is considered to be a model parameter in GMSB models especially in minimal GMSB models like the SPS8 benchmark model.

It is important to note that GGM models, [20, 21, 22, 23, 24], the mass of the gauginos $M_a, a = 1, 2, 3$ defines the parameter space for these models. Using equation 2.20, the fundamental SUSY breaking scale \mathbf{F} can be redefined in terms of the effective SUSY breaking scale Λ and the Messenger particle mass scale M_{mess} :

$$\mathbf{F} = C_{\text{grav}} \cdot \Lambda \cdot M_{\text{mess}} \quad (2.29)$$

and from equation 2.16, the gravitino mass is re-written shown in equation 2.30

$$m_{\tilde{G}} = C_{\text{grav}} \cdot \frac{\Lambda M_{\text{mess}}}{\sqrt{3} M_{\text{pl}}} \quad (2.30)$$

In summary, the parameters Λ , N_5 , and C_{grav} determines the phenomenology of GMSB models. The gravitino can become very light with its mass bounded only by cosmological observations and as such is identified as the least stable supersymmetry particle (LSP). By changing the value of C_{grav} , which is equivalent to scaling the induced supersymmetry breaking energy scale, allowing for weak interactions between the hidden sector and the messenger particles, the mass of the gravitino, $m_{\tilde{G}}$, is changed. This influences the decay rate and lifetime of the next-to-lightest supersymmetry particle (NLSP) decaying to the gravitino which can vary from being an instantaneous or prompt decay to being a long-lived particle decay.

Phenomenology of GMSB Models

The presence of light gravitinos and a unique gravitino-scalar-chiral fermion and gravitino-gaugino-gauge boson interactions as shown in figure 2.5 in GMSB models attract a lot interests in GMSB phenomenology as gravitino masses can be allowed to be as low as a few eV and only bounded by cosmological models making them an excellent candidate particle for Dark Matter (DM).

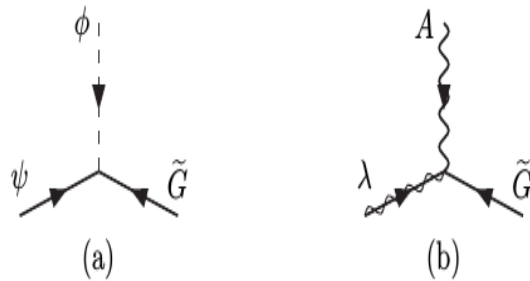


Figure 2.5: Feynman diagrams of gravitino/golstino, \tilde{G} , gaugino and scalar interactions with superpartner pairs (ψ, ϕ) scalar (a) and (λ, A) gaugino (b) decay to gravitino.

These light gravitinos with weak gravitino-gaugino or gravitino-scalar interactions allows for the decay of any next-to-lightest MSSM particle to a gravitino. This decay rate depends on the mass of the gravitino $m_{\tilde{G}}$ as long as R-parity is conserved. Thus, in the decay of every MSSM particle, the gravitino will likely or eventually be included in its final states. We can parametrised this decay rate by using C_{grav} . It is easy to see that $C_{grav} \geq 1$. It is important to note that there are other GMSB phenomenological observations which do not entirely considered the gravitino as the lightest supersymmetric particle. Thus in order to study the phenomenology of GMSB models, one can define a parameter space using the following parameters given in equation 2.31.

$$\{\Lambda, M_{mess}, N_5, \tan(\beta), sgn(\mu), C_{grav}\} \quad (2.31)$$

Where the additional parameters $\tan \beta$ and $sgn(\mu)$ are related to the two Higgs bosons necessary for supersymmetry breaking. $\tan \beta$ is the ratio of the vacuum expectations values for both Higgs bosons and $sgn(\mu)$ defines the sign of the Higgs potential. These sets of parameters given in equation 2.31 are those we will be studying within the minimal GMSB (mGMSB). In the SPS8 benchmark model $M_{mess} = 2\Lambda$,

$\tan(\beta) = 15$, $\mathbf{N}_5 = 1$, Λ and C_{grav} are allowed to vary,[12]. In other gauge mediating supersymmetry models like the General Gauge Mediation SUSY breaking (GGM), $\{M_3(\text{gluino mass}), M_2(\text{Wino mass}), M_1(\text{Bino mass}), \tan(\beta), \text{sgn}(\mu), c\tau_{NLSP}\}$ is the parameter space,[21, 22]. In GGM models, colored sparticles are not required to be heavier than their Electro-Weak sparticles allowing for greater discovery potential at hadron collider[25]. Thus, allowing for possibility of many candidates NLSP particles and not only the neutralino as in the case with mGMSB models like the SPS8 model. For Pure General Gauge Mediation SUSY breaking (PGGM), the parameter space is rather scan using $\{\Lambda_G, \Lambda_S, M_{mess}\}$ parameter set.

Of all other possible decay modes in GMSB models, this thesis is interested only in decays where eventually, the Next-To-Lightest SUSY particle (NLSP) decays to the lightest SUSY particle (LSP) which is the gravitino and its SM partner; i.e if particle, \tilde{p} is the NLSP, then it will decay is given according to equation 2.32.

$$\tilde{p} \rightarrow p + \tilde{G} \quad (2.32)$$

In the SPS8 model, \tilde{p} is the lightest neutralino ($\tilde{\chi}_1^0$). There are four types of neutralinos which are a mixture of the supersymmetric particles Bino (\tilde{B}°), Wino (\tilde{W}°), higgsino ($\tilde{H}_u^\circ, \tilde{H}_d^\circ$), depending on the choice of parameters M_1, M_2, M_3 , or Λ , $\tan\beta$, and $\text{sgn}(\mu)$. While particle p could be a photon (γ), Z boson (Z) (or Z') and a higgs boson (h). This thesis, for experimental convenience, will focus on the parameter space for which the the particle p is a photon (γ) and $C_{grav} > 1$. This ensures that the lifetime of the NLSP is long enough such that its decay happens within the detector volume and the resulting photon is delayed or non-prompt on length scales of the detector.

The decay rate for a NLSP to its SM partner and a gravitino can be approximated as in equation 2.33 (More details can be found in [11, 18, 26]).

$$\Gamma(N\tilde{LSP} \rightarrow \gamma \tilde{G}) \approx \frac{m_{NLSP}^5}{\mathbf{F}^4} \quad (2.33)$$

This approximation is almost the same for the non-minimal GMSB models except that additional parameters are present showing explicit dependence of the neutralino life time on neutralino mixing.

2.3 Long-Lived Particles in GMSB Models

In addition to mass, charge and spin being experimental handles use in the search for new physics, a particle's life time or decay length is a very relevant for discovering new fundamental interactions. Since through life time measurements, one has direct access to measuring and understanding and in some cases excluding the energy scale and fundamental parameters involved in a new interaction.

2.3.1 Production of supersymmetric particles at Hadron Colliders

Producing a supersymmetric particle at a hadron collider like the LHC is a probabilistic process. This process is quantitatively expressed as the production cross-section. The production cross-section expresses the probability of a given process happening. The mass of supersymmetric particles is much higher than those of SM particles and as a result, the cross-section for producing supersymmetric particles at a hadron collider is much smaller than that for SM particles.

The cross-section of a given process in supersymmetry (SUSY) happening at the particle collider can be computed and compared with experimental measurements. The cross-section depends on the type of processes involved. Each process can be expressed in diagrammatic forms called *feynman* diagrams and the probability of that process happening is computed using its represented feynman diagrams.

Supersymmetric processes that can lead to neutralino production and decay at a proton collider at the LHC can involve Electro-Weak and strong interactions. SUSY production through strong processes have larger cross-sections compared to Electro-Weak processes as can be shown in figure 2.6.

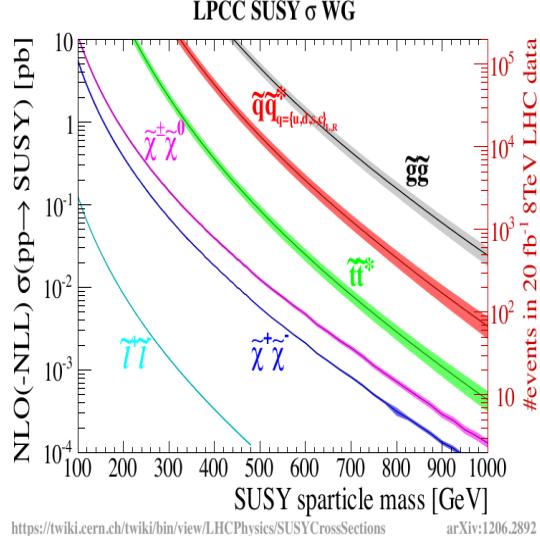


Figure 2.6: Supersymmetry production cross-section against sparticle mass for different modes of supersymmetry production at a proton-proton collider. $pp \rightarrow \tilde{g}\tilde{g}$ processes have the dominant production cross-section.

Electro-Weak production of neutralinos through Electro-Weak interactions are known as *direct* production of neutralinos while those due to strong interactions which is the dominant mode of supersymmetry production at the LHC, produce neutralinos through the production and decay of much heavier supersymmetric particles like squarks (\tilde{q}) and gluinos (\tilde{g}). This is referred to as *indirect* or *cascade decay* production of neutralinos. Examples of strong interaction processes include $pp \rightarrow \tilde{g}\tilde{g}$, $\tilde{q}\tilde{q}^*$ and their feynman diagrams are shown in figure 2.7. The produced squarks and gluinos do not decay directly into the gravitino but through a cascade decay process eventually decay to the gravitino through the neutralino. This is because, first, in R-parity conserving GMSB models, due to conservation of R-parity, SUSY particles are produced in pairs, and secondly because in GMSB models, as we saw in figure 2.5, they are no gravitino-gluino-gauge boson or gravitino-squark-gauge boson interactions but rather gravitino-gaugino-gauge boson or gravitino-scalar-chiral fermion interactions. Thus, the squark or gluino do not directly couple with the gravitino and so cannot directly decay into the gravitino but rather through a cascade decay.

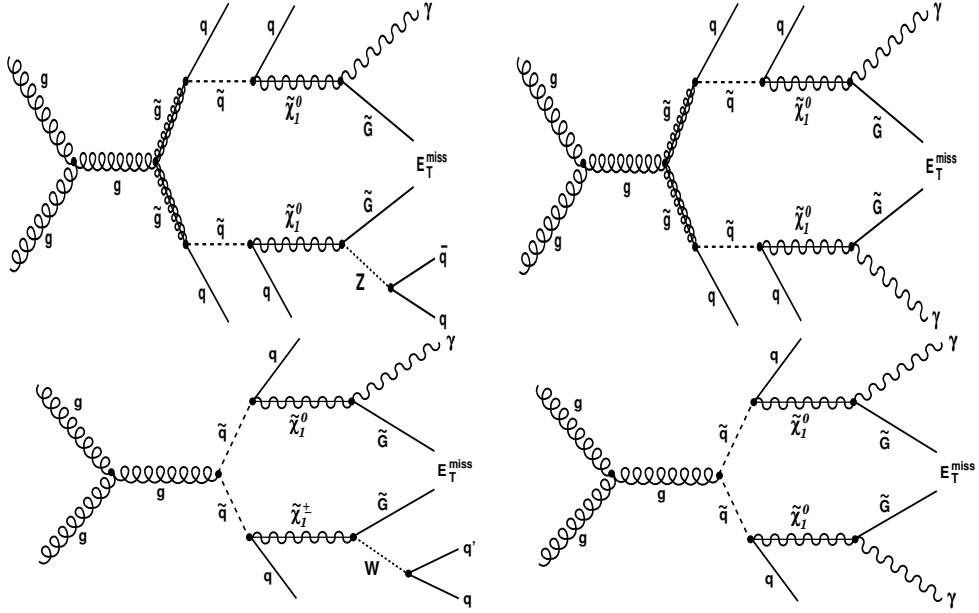


Figure 2.7: Feynman diagrams for gluino single (*top left*) and double (*top right*) photon and squarks single (*bottom left*) and double (*bottom right*) photon production from cascade decays of gluino and squark at LHC.

The list of feynman diagrams presented for SUSY processes in figure 2.7 is not exhaustive. As previously mentioned, SUSY production cross-sections are very small compared to SM production processes. A production cross-section is express in term of a unit called a *barns* (b). ($1 \text{ b} = 10^{-28} \text{ m}^2$). Because this number is quite small it is usually further express with suffix in front of the unit barn such as *nano* (n) or *pico* (p) or *femto* (f). The typical cross-section of producing a SUSY particle at the LHC is of the order of $1 \text{ pb} = 10^{-12} \times 10^{-28} \text{ m}^2$ or at times $1 \text{ fb} = 10^{-15} \times 10^{-28} \text{ cm}^2$ for extremely rare SUSY processes. While a typical production of a standard model process such as the production of the Z or W bosons is of the order of a few $nb = 10^{-9} \times 10^{-28} \text{ m}^2$. Thus, finding a SUSY particle in an environment such as the LHC is very challenging, since most SUSY production cross-section are very small compared to an overwhelming high cross-section processes from the standard model.

2.3.2 Particle Production Cross-section and Decay Rate

Almost all particles disintegrate or *decay*, most very rapidly. Collectively particles which disintegrate are said to be unstable while the few which do not are said to be stable. Those which take a long time to disintegrate are termed meta-stable or “*long-lived*” particles. The length of the decay time and context will tell whether a particle is meta-stable or long-lived. The stability of a given particle is measured with respect to the age of the universe (13.7 billion years). The only understood stable particles in nature are the **electron**(and anti-electron) (e), **up** (u) and **down** (d) quarks and their anti-quarks, the **photon** (γ), the lightest neutrino (ν_e) and the **graviton**. Particles decay by transforming from one type of particle or generation unto another either through interactions, radiation or oscillation. This decay, in analogous to our everyday experience depends on the their interaction strength with possible particles they can decay into. For example, strongly interacting particles will decay almost immediately while weakly interacting particles will naturally take some time. However, this is not the whole story, as quantum effects will also determine the particles nature of decay. Meta-stable particles which are composite (bound states of elementary particles), are more unstable and easily decay into particles with smaller mass. An example of a meta-stable particle is the **neutron** (udd) which on its own, outside the atomic nucleus can remain stable for about 15 or so minutes. While, neutrons living inside some atomic nuclei can live for a period of time comparable to the age of the universe. Another meta-stable particle like the proton (uud) seem very stable but can possibly decay after a very long period of time. It is speculated that the proton can remain stable for up to a period of about 10^{33} years. Atomic nuclei can also be considered as meta-stable living for about a tiny fraction of a second. Thus for all practical purposes, the proton is considered a stable particle while the neutron is considered a *long-lived* particle. It is believed that if *dark matter* is made of particles then those particles must be very, very, very long-lived with time also comparable to or beyond the age of the universe.

The stability of a particle is determined by the properties of the particle combined with conservation laws of a quantum number or conserved quantity like energy, spin, momentum, angular momentum and charge. Other factors may also play an important role such as phase space (availability of lighter particles to decay into), violation of some fundamental property like *strangeness* or the mediating particle usually a boson being

very massive compared to the momentum transfer between the parent and the daughter particle. These laws combined with particle's properties leads to a set of rules which are (almost) entirely determine whether a particle can decay or not or at most decay very rarely. These set of rules can be summarized as follows:

- All particles must and should decay to two or more particles.
- The mass of the decaying (parent) particle must exceed the sum of the mass of the particles produced (daughter particles) in its decay.
- There must be charge conservation i.e, the total electric charge of the parent particle must equal or match the total electric charge of the daughter particles.
- The total number of fermions or spin-1/2 particle before and after the decay must change only by an *even* number.
- The total number of quarks minus the total number of anti-quarks must not change in any decay.
- The nature of interaction and degree of phase space available must all be satisfied in order for any decay to take place.

The rate at which a given particle disintegrate is known as it's *decay rate*, symbolized as Γ . It is an experimentally measurable quantity which can also be computed in theory. A particle's decay rate Γ can depend on the strength of a given interaction involved in the decay. As such the experimental measurement of decay rate provides access towards understanding the type of interaction involved and important parameters governing the underlying interaction or mediating particles involved in a given decay. Thus, measuring a particle's decay rate can be used as a direct access to search for other interactions beyond the known interaction and thus provide evidence for new physics.

A single particle can decay into more than one type of particles. Provided the conditions for decay are satisfied, its decay into potential particles is possible. The decay into a specific set of particles is known as a *decay channel*. Different decay channels can be quantified with respect to the overall *total decay rate* of the parent particle. This quantification is expressed as a *branching ratio (BR)*. Thus the BR gives quantitative estimate of the possibility or probability of a parent particle decaying to

specific daughter particles or through a given channel.

The inverse of a decay rate is the *proper life time*, denoted as τ .

$$\tau = \frac{\hbar}{\Gamma} \quad (2.34)$$

τ is a measure of the time lived as measured in the frame of reference of the decaying particle (rest frame) by a particle before disintegrating. A convenient way to express life time is by instead of the time lived use the distance traveled by a particle before it decays denoted by $c\tau$, where c is the speed of light in vacuum and τ is the *proper life time*. This is called the *proper decay length*. However, nearly impossible to measure the proper decay length inside a particle's rest frame, thus laboratory measurements are performed while the decaying particle is moving with some velocity, v with respect to a stationary laboratory. In making these measurements, we take into consideration this difference in motion of frames (the moving particle frame and the stationary laboratory frame) or relativistic effect in understanding our measurement of the decay length in the laboratory translated into the proper decay length of the particle. The laboratory measured decay length is expressed as:

$$\vec{L} = \vec{\beta}\gamma c\tau \quad (2.35)$$

where $\vec{\beta} = \frac{\vec{v}}{c}$, \vec{v} , the velocity of the moving particle and $\gamma = \frac{1}{\sqrt{1 - \frac{v^2}{c^2}}}$ is a factor accounting for the relative motion between the two frames. Equation 2.35 can also be expressed in as $\vec{L} = \frac{\vec{p}}{m}c\tau$, in terms of the particle's momentum p and mass, m . Thus, the larger the particle's momentum, the further is its distance traveled from its point of production as measured in the laboratory frame. On the other hand, the larger the particle's mass, the slower its traveling speed and hence shorter its distance traveled.

Because particle's decay rate Γ can depend on the strength of a given interaction involved in the decay. Thus the decay length, $c\tau$ for electromagnetic interaction, can be very different to that of weak and strong interactions. The decay length for strong interactions is the shortest because of the strong nature (coupling constant ≈ 1) of strong interaction. The weak and electromagnetic interactions have much smaller coupling constants thus often leads to longer decay length. There are some exceptions to this due to other factors playing a key role than only the strength of a given interaction such

as the size of the available phase space and the difference in mass between the parent and the sum of the mass of the daughter particles.

In order to avoid misunderstanding of what we mean by long-lived particles in this thesis, we cover mostly *massive neutral meta-stable* particles referred here as **Neutral Massive Long-Lived Particles** (NMLLP). These are either elementary or composite neutral particles with life-time within the detectable range of a collider detector i.e few nanoseconds. In general, long lived could mean life-times from a few nanoseconds (10^{-9} s) to the age of the universe or equivalently from a few μm to billions of km. Thus, our interpretation of neutral long-lived particles will be particles whose decay length ranges from a few μm to few meters or decay length is within the detectable size of the LHC detectors and in particular electromagnetic calorimeter sector of LHC detectors.

2.3.3 Decay of supersymmetric particles in CMS detector

Neutralino as NLSP Decay Length

The neutralinos produced from the cascade decay of squarks and gluinos can decay into a gravitino and a gauge boson or scalar particle. This decay is also a probabilistic process and can be expressed and quantified as a single real number. There are always many options for a given particle to decay into and each of these options is quantified by a number known as the *Branching Fraction* or *Branching Ratio*. Summing all the branching ratios for all the different decay processes gives the total *Decay Width*. The total decay width, can also be computed and expressed as a single real number in units of GeV or MeV (GeV = giga electron volt = 10^9 eV).

The probability for a neutralino ($\tilde{\chi}_1^0$), produced with an energy E having mass m to travel a distance x before decaying to a photon and gravitino in the laboratory frame is given as:

$$\mathcal{P}(x) = 1 - \exp\left(-\frac{x}{L}\right) \quad (2.36)$$

where

$$L = c\tau_{\tilde{\chi}_1^0} \cdot (\beta\gamma)_{\tilde{\chi}_1^0} \quad (2.37)$$

Equation 2.37 gives the decay length of the neutralino particle as measured in the

laboratory or a particle detector. This measured decay length depends on two major factors. First, The boost or $\beta = v/c$ which indicates the motion kinematics for a decaying particle. For slow moving particles which usually lead to large arrival time at the measuring detector, it is required that $\beta \ll 1$. These are known as slow moving particles. For the case of the neutralino, β can be redefined as given in equation 2.38.

$$(\beta\gamma)_{\tilde{\chi}_1^0} = \frac{|p|}{m} = \sqrt{\left(\frac{E}{m}\right)^2 - 1} \quad (2.38)$$

Equation 2.38 shows that in order for the condition $\beta \ll 1$ to be true, one would require that the momentum (in this case transverse momentum, p_T) with which the neutralino is produced from gluino or squarks decays must be much smaller than the neutralino mass i.e $m_{\tilde{\chi}_1^0}$. Thus, slow moving neutralino, whose ratio, $p_T_{\tilde{\chi}_1^0}/m_{\tilde{\chi}_1^0} \ll 1$ will be good candidates for detectable long-lived neutralinos.

Since mass of SUSY particles like gluino, squarks and also neutralino is kept fixed by the SUSY effective breaking scale Λ as shown in equations 2.24, the neutralino p_T will depend on the number of associated quarks observed as *jets* produced during the gluino or squark decay. Gluino or squark decays with very low jet multiplicity will lead to the production of large p_T neutralinos which eventually leads to more boost factor while high jet multiplicity will lead to low p_T neutralinos and hence low boost or β factor. It is important to note that in either case, this depends also on the measured p_T of the jets whether is low or high jet multiplicity cases. It is also worth mentioning that the photon produced from neutralino decay can also be arrived with large delayed time in situations where the photon arrival path to the detector is not a direct straight path but rather deviated as a result of a highly boosted neutralino produced from gluino or squark decay.

In addition to the boost factor, the inherent proper decay length, $c\tau$, will also determine the extend to which a long-lived neutralino is detectable at a particle detector. Neutralino with very long lifetime, $c\tau$, beyond the detectable length of the particle detector will obviously travel out of the detector before decay and as a result are often not detectable while neutralinos with very short lifetime may also be undetectable as their decay length travel is not enough to be able to separate them for background events in a detector environment like the LHC unless other methods are employed like using its

impact parameter distance travelled. However, this is only applicable in scenarios where the neutralino decays into a charged particle with tracks in the detector such that its decay production vertex can be used to correctly calculate and extract the neutralino impact parameter or in other sophisticated detectors which the direction of the particle from neutralino decay is accessible. This is the case with ATLAS particle detector and not so with CMS detector. One can always estimate the neutralino proper decay from theory using equations like the one given in equation 2.39.

$$c\tau_{\tilde{\chi}_1^0} \approx \left(\frac{m_{\tilde{\chi}_1^0}}{\text{GeV}} \right)^{-5} \left(\frac{\sqrt{\mathbf{F}}}{\text{TeV}} \right)^4 \quad (2.39)$$

It is important to observe here that, varying \mathbf{F} changes the lifetime of the neutralino. This variation can be easily be performed in GMSB models using the parameter C_{grav} . Equation 2.39 now becomes equation 2.40 which is the equation used to simulate and produce simulated samples (Monte Carlo) of neutralino production and decay when studying neutralino properties in a particle detector.

$$c\tau_{\tilde{\chi}_1^0} \approx C_{grav}^2 \left(\frac{m_{\tilde{\chi}_1^0}}{\text{GeV}} \right)^{-5} \left(\frac{\sqrt{\mathbf{F}_s}}{\text{TeV}} \right)^4 \quad (2.40)$$

Using the LHC as the proton-proton collider and the CMS detector as the instrument for detecting and measuring the lifetime of delayed photons produced from long-lived neutralino decays. We have simulated neutralino production and decay according to the mGMSB SPS8 benchmark model, where the neutralino is the NLSP decaying into a photon and the gravitino as LSP. Figure 2.8 shows some kinematic properties and the neutralino proper decay length distribution and the delayed photon in different SUSY parameter choices. The CMS Software (CMSSW) packaged is used to simulate and study the neutralino production and decay in CMS detector while using root data analysis framework, we also performed some fit analysis on the generated and simulated decay length distribution to extract its proper decay length as produced during the MC generation and compare this to theoretical expectations to check for consistency. Our choice of parton distribution function is CTEQ6L1 with LHAPDF for producing GSMB MC samples from SLHA files. Most studies are performed by varying Λ and C_{grav} or the neutralino proper decay length, $c\tau$. The results are expressed in a two dimensional

Λ or $m_{\tilde{\chi}_1^0}$ against $c\tau$ for a particular model.

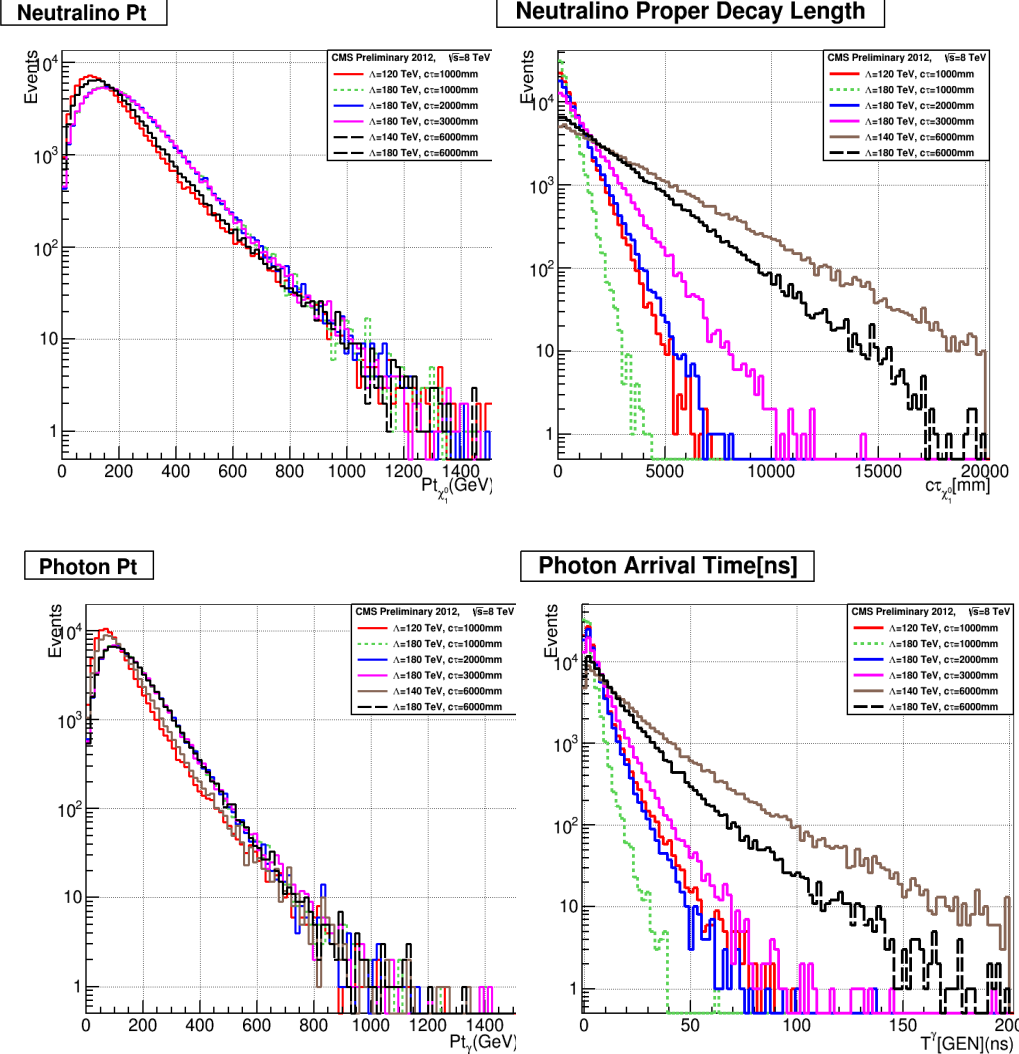


Figure 2.8: Neutralino transverse momentum distribution (top left) and proper decay length (top right) with its decayed photon transverse momentum distribution (bottom left) and time of arrival at ECAL (Bottom right) for GMSB SPS8 model.

2.4 Previous Search Experiments and Results

The hunt for the discovery of DM and new particles, has led to several experimental search for neutral long-live particles decaying to photons. Obviously, negative results from these experiments has led to the putting limits of the lifetime, mass and cross section of possible existence of SUSY particles in different models of SUSY. Results from experiments(DO, CDF, CMS and ATLAS)[27, 28, 29, 30, 31] in the search for Neutralino NLSP decaying to photon and gravitino and interpreted within the SPS8 benchmark model with choice of parameters as seen in 2.9. These results show that within the SPS8 model, neutralinos with mass $m_{\tilde{\chi}_1^0} \leq 245$ GeV and proper decay length $c\tau_{\tilde{\chi}_1^0} \leq 6000$ mm cannot exist at hadron colliders and thus their existence has been excluded.

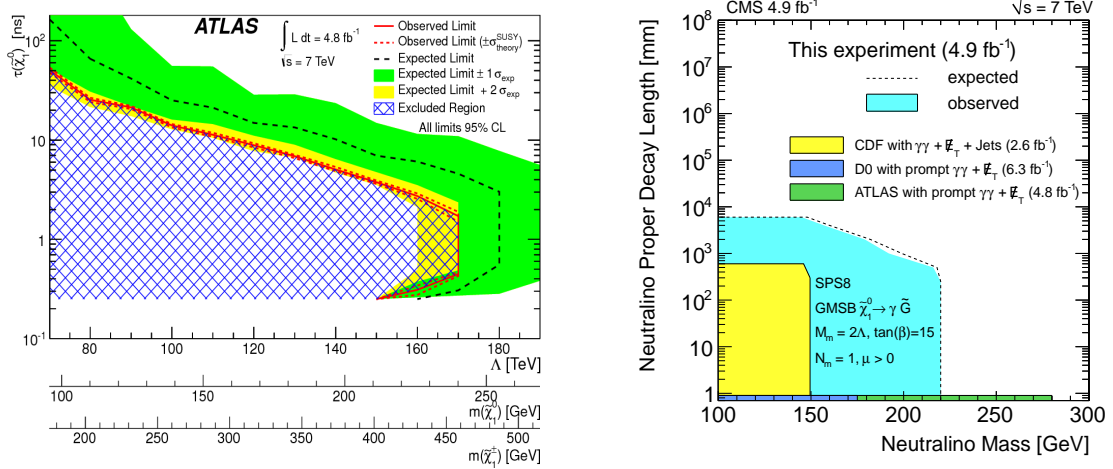


Figure 2.9: Neutralino lifetime and mass upper limit from ATLAS(left) and CMS(right) 7 TeV analysis with non-pointing photons and MET.

Chapter 3

Hadron Collider and Detector

This section describes the particle accelerator and detectors that are used to produce and detect particles at colliders. The first section describes the particle accelerator while the following section describes the CMS detectors with emphasis to those sections which are directly relevant to this analysis. A detailed description of the LHC and detectors can be found in [32] and [30].

3.1 Large Hadron Collider

3.1.1 Overview

The Large Hadron collider (LHC) is a proton-proton and heavy ion collider designed to achieve a center of mass \sqrt{S} energy of 14 TeV. It is hosted and controlled by the European Organisation for Nuclear Research (CERN). Unlike linear colliders, the LHC is a circular collider with nearly 27 km in circumference located at the border between France and Switzerland. It is designed to smash protons and ions against each other controlled by powerful magnets at officially four main locations. At each major collision point are multi-purpose particle detectors ranging from A Toroidal LHC Apparatus (ATLAS) and Compact Muon Solenoid (CMS) both non-fixed target detectors, A Large Ion Collider Experiment (ALICE) for colliding heavy ions and finally Large Hadron Collider beauty (LHCb), a fixed target experiment for investigating the properties of B-Hadrons. We give a full description of the important parts of the LHC in the following subsections,

detail discussion of other interesting parts can be found here [32]. There are three main steps prior to colliding protons or ions at the LHC. The first is ramping up the energy of the beams followed by squeezing the beams at interaction points(CMS or ATLAS) and finally remove the separator bumps that are formed by local corrector magnets. Thus our description of the LHC will follow this three stages.

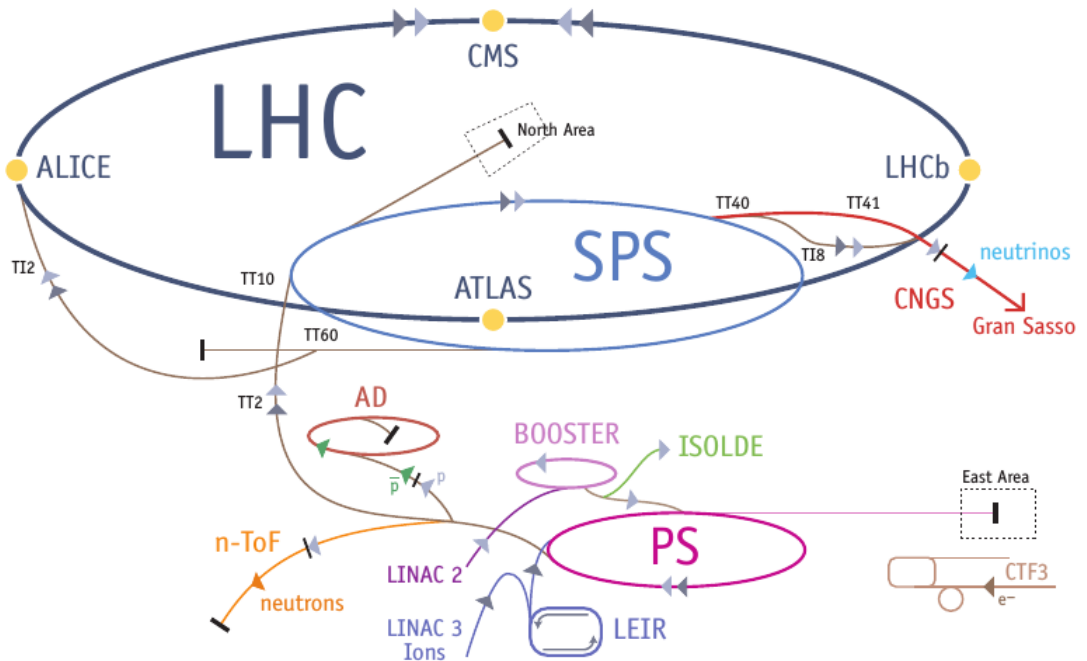


Figure 3.1: Schematic diagram showing the full Large hadron Collider. Image taken from [33]

3.1.2 Colliding Energy

Hydrogen gas is inserted into a linear accelerator called Linac2 where they are stripped off of their orbiting electrons to become hydrogen ions or protons. Under the influence of electric fields, these protons are accelerated to an energy of 50 MeV creating a stream of particles called *particle beams*. These beams are arranged in packets known as *bunches*. Particle acceleration is provided through the use of Radio-Frequency (RF) cavities containing electromagnetic fields which oscillate at a particular frequency. The protons surf this electromagnetic fields and are grouped in troughs of the electromagnetic

waves called RF *buckets*. The circular nature of the synchrotron accelerator ensures that the protons pass many times through a cavity and during each time their energy can be slowly increase to reach the design energy. The 50 MeV protons from the Linac2 are injected into the proton synchrotron Booster (PSB). The PSB accelerates the protons to up to 1.4 GeV and inject them into the Proton Synchrotron (PS) which pushes the protons energy to 25 GeV. These protons travelling at 99.93% the speed of light are sent to the Super Proton Synchrotron (SPS) and accelerated to an energy of 450 GeV. They are finally transferred into the LHC ring(both in a clockwise and anti-clockwise direction) and accelerated for about 20 minutes to their norminal energy of 7 TeV. As this point these protons are travelling with the speed of 99.9999% the speed of light. Powerful magnets are used to keep the beeps travelling in the circular LHC ring. The advantage of circular particle colliders such as the LHC over fix target colliders is that, the energy available to make new particles called the center of mass energy denoted as \sqrt{S} is simply the sum of the energy of the two beams i.e $\sqrt{S} = E_{\text{beam1}} + E_{\text{beam2}}$ compared to $\sqrt{E_{\text{beam}}}$ for fix target experiments. In the case of the LHC, each beam is designed to have energy of 7 TeV and that makes $\sqrt{S} = 14$ TeV. Although in circular collider, an accelerating charge particles like the proton would loose energy in for the form of radiation which is inversely proportional to the mass of the charge particle to the fourth power requiring the need for continuous addition of energy after each turn to maintain the beam energy to a stable value. Since the proton's mass is about 0.938 GeV which is close to 1 GeV, this lost of energy is not very significant unlike electrons whose mass of about 0.000511 GeV making their energy lose through radiation more and thus less preferable to use as the main particles for a circular hadron collider. However, the debris of particles produced when electrons collide is much less compared to that of hadrons making analysis in a hadron collider more challenging.

3.1.3 Luminosity

Luminosity is the measurement of the number of collisions that can be produced in a collider per squared area per second. This is known as the instantaneous luminosity and it is related to the cross-section(a probabilistic measure of the possibility of a given collision process happening) through the equation:

$$N_{\text{events/sec}} = \text{Luminosity} \cdot \text{Cross Section} \quad (3.1)$$

where the luminosity \mathcal{L} is related to the total integrated luminosity (delivered luminosity over time) $L = \int \mathcal{L} dt$ and is defined in terms of accelerator (assuming round beams and equal values of beta function) parameters as:

$$\mathcal{L} = \frac{1}{4\pi} \cdot (f_{rev} n_b N_b) \cdot \frac{N_b}{\varepsilon_N} \cdot \frac{\gamma}{\beta^*} \cdot \mathcal{R}(\theta_c, \varepsilon, \beta^*, \sigma_z) \quad (3.2)$$

where N_b is the number of particles per bunch, n_b is the number of bunches, f_{rev} is the revolutionary frequency, $\gamma = E/m_p$ is the relativistic factor, ε_N is the normalised beam emittance which along with β^* , the value of the amplitude or beta function at interaction point, determines the size of the beam. \mathcal{R} is the geometrical reduction factor arising from the fact that the beams do not collide head-on but at a non-zero angle called the crossing angle or “*Piwinski angle*” ($\phi \equiv \frac{\theta_c \sigma_z}{2\sigma_x}$). This effect is known as the *hour-glass effect*. From the above definition 3.2, it is evident that keeping the emittance (meaning particles in beam are confined to a small distance and have nearly the same momentum) means the likelihood of particle interaction will be greater and thus higher luminosity. However this is often not easy to archive as increasing the beam energy means reducing the beam emittance. The normalized emittance ε_N is often used as its dependence on beam energy is a squared root dependence. In the same way, lower beta values implies the width of beam is narrower or properly “*squeezed*” at interaction point resulting to an increase in number of collisions hence higher luminosity. This squeezing of depends on the quadrupole magnet configuration and powering. In addition to low beam emittance and lowest value of beta function at interaction point (β^*), one can also archive higher luminosity by using high population bunches (N_b) and collide them at high frequency.

Luminosity Measurement Obviously using equation 3.2 to determine the instantaneous and integrated luminosity would involve a lot of uncertainty in the measurements of about 20-30%, as there are so many parameters whose value need to be measured precisely in a normal LHC operation. Rather specialised LHC runs known as “*Van der Meer Scans*”[?] are used to calibrate specialized equipments used for determining luminosity. The method employed by CMS is using the Hadronic Forward (HF) calorimeter

to make luminosity measurements. Using production rates or cross sections of well and precisely calculable processes and rewriting 3.2 as:

$$\mathcal{L} \equiv \frac{\text{Rate}_{tot}}{\sigma_{tot}} = \frac{\mu n_b f_{rev}}{\sigma_{tot}} \quad (3.3)$$

where $\mu = \langle N_{tot}/n_b \rangle$ is the *average number of interactions per bunch crossing*. CMS keeps track of “recorded” and “delivered” luminosity. Delivered luminosity refers to the luminosity delivered by LHC to CMS and one would expect this to be equal to the amount recorded. However, there are instances where the CMS detector is unable to take data either because the data acquisition chain (DAC) is busy or one of the CMS sub-detectors is temporarily down. Part of my job as a sub-detector expert during CMS data taking of LHC Run 1 was to make sure that the period of temporal unavailability of the ECAL sub-detector is as minimal as possible.

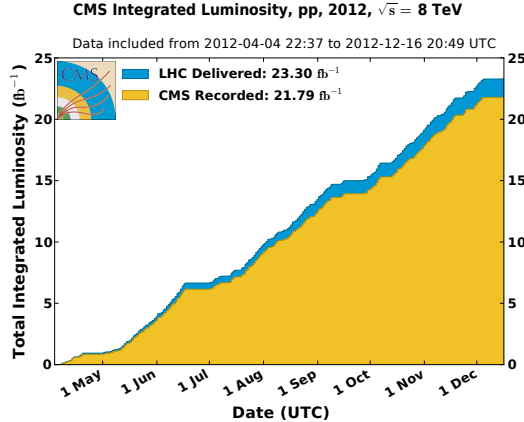


Figure 3.2: Cumulative luminosity versus day delivered to (blue), and recorded by CMS (orange) during stable beams and for p-p collisions at 8 TeV centre-of-mass energy in 2012.

3.1.4 Superconducting Electromagnets

The LHC design and operation uses a total of 9593 powerful magnets of different types for different purposes. Since there are two beams of protons running in clock-wise and anti-clock wise directions, the LHC uses an ingenious technique design of the magnetic field in every dipole magnet generates a vector field \mathbb{B} in each pipe pointing in opposite direction to that of the other but both always perpendicular to the beam directions.

The Lorentz or magnetic force acting on the protons in both pipes always point towards the center thus keeping the beams in circular motion. In circular accelerators as the LHC and its smaller synchrotron rings, given the accelerator radius, R , the beam energy p is determined by the strength \mathbf{B} of the magnetic field. This can be easily understood using the Lorentz force such that $p[TeV] = 0.3\mathbf{B}[T] \cdot R[km]$. The LHC is a 26.659 km in circumference machine using powerful dipole magnets with magnetic field strength of about 8.33 Tesla(T) are 7 TeV to keep the protons circulating in their curved path or orbits. The LHC operates using superfluid helium for heat transport at 1.4 K(-271.3 °C) temperature to prevent these near 1232 dipole magnets, 858 quadrupole and 6208 correcting magnets from overheating due to the energy stored in these magnets. Conventional magnetics aren't convenient for modern particle accelerators with high center of mass energy for both performance and economic reason. Rather, superconducting magnets made with modern technology using niobium-tantanium (Nb-Ti) filaments strands or cables are used to provide the high magnetic field required.

Quadrupole electromagnet and correcting magnets are used to keep the particles in the beam and archive the required focus and de-focusing needed. At interaction point, the quadrupole magnets are held symmetrically around the beam pipe to help squeeze the proton beams to very low values of beta function thus ensuring that many particle collisions as possible necessary for higher luminosity.

3.1.5 Timing

The Large Hadron Collider (LHC) is designed to collide proton-proton (pp) bunches every 24.95 ns at designed luminosity. This means, the distance between each proton bunch is about 7.5 m compared to the nearly 100 m of optical fibre length which is required to transport readout information from the very front end electronics on the detectors to the back end electronics at Point 5 for processing. It is therefore imperative to have a data synchronisation system for the trigger and readout systems of the LHC experiments in order that events from every proton-proton collision are properly assigned to the particular bunch crossing (BX) which produced them. The LHC is equipped with a Timing, Trigger and Control (TTC) system with a bunch clock frequency of 40.07897 MHz whose function is to distribute synchronized LHC time to

all the detectors including CMS. Timing synchronisation in the LHC is achieved using a Beam Synchronous Timing (BST) system which distributes timing using the LHC revolution frequency(at 11.246 kHz) or LHC orbit and the RF bunch crossing frequency(40.07897 MHz at 7 TeV). Thus, the LHC fast timing signals from the RF generators of the machine and orbit signals are distributed from the Prevessin Control Room (PCR) through single-mode optical fibers(about 10.1 km in length for CMS) to all LHC experiments, test beam areas, beam instrumentation around the ring and the SPS transfer lines. At CMS counting room, the LHC clock and orbit signals are recovered in the TTC Machine Interface crate (TTCmi) and later distributed to the Trigger Control and sub-detector master TTC crates. All Level1 (L1) trigger and Data Acquisition (DAQ) pipelines are driven with a 24.95 ns cycle clock locked to the LHC machine clock. The phase difference between the LHC 40 MHz clock and the arrival of detector signals from collision to the front-end electronics must be determined and adjusted for and monitored. The determination and assignment of pulses to bunch crossings depends critically on this initial clock phase adjustments and stability. This amplitude or pattern(also known as trigger primitives) for each trigger and bunch crossing is transmitted to the regional trigger logic in digital form every crossing and is synchronised with the LHC clock. Each trigger primitive digital data is then assigned to clock cycle in a process known as bunch crossing assignment. a Detail expert description of LHC unified timing distribution system can be found here [36, 37, 38, 39].

LHC Operation Parameters 2010-2013				
Parameter	2010 value	2011 Value	2012/13 Value	Design Value
Beam energy[TeV]	3.5	3.5	4.0	7
β^* in IP 5[m]	3.5	1.0	0.6	0.55
Bunch spacing [ns]	150	75/50	50	25
Number of bunches	368	1380	1380	2808
Protons/bunch	1.2×10^{11}	1.45×10^{11}	1.7×10^{11}	1.15×10^{11}
Normalised emittance[mm.rad]	≈ 2.0	≈ 2.4	≈ 2.5	3.75
Peak luminosity[$cm^{-2}s^{-1}$]	2.1×10^{32}	3.7×10^{33}	3.7×10^{33}	1×10^{34}
Evts/bunch crossing	4	17	37	19
Stored Beam energy(MJ)	≈ 28	≈ 110	≈ 140	≈ 362
Int. Luminosity by CMS[pb^{-1}]				-
Circumference[km]	26.659	26.659	26.659	26.659
Dipole Magnet B[T]	8.33	8.33	8.33	8.33

Table 3.1: The LHC operation parameter conditions during RUN 1:2010-2013

LHC Bunch Structure

An LHC orbit is made of about 3564 *bunch* places. However only 2808 are occupied with protons. The bunch structure is archived by breaking a continuous proton beam into pulsed beam of separate bunches using an electromagnetic field with oscillating frequency of 400 MHz(LHC ring) in the SPS and LHC RF cavity. Thus each bunch is in an RF bucket. Each RF bucket has an energy against time profile as can be seen in figure below. The LHC filling scheme is arranged such that not all RF buckets have proton bunches. Thus there are empty buckets or beam gaps with missing bunches. These gaps are necessary to make room for the rise/fall times at SPS/LHC injection and ejection and abort kickers magnets during say LHC beam dump. The time separation between two buckets/bunches filled or unfilled is about 2.5 ns. Filling and acceleration at each RF cavity point is performed so that there are about 10^{11} protons/bunch. However, during filling and eventual bunch splitting at the PS, it is possible that some empty buckets are filled with a much smaller proton population compared to the main bunch.

These less proton populated buckets can be $\Delta t = 2.5, 5.0, 7.5, \dots$ ns, trailing the main bunch labelled as Beam1 or Beam2 otherwise leading the main bunch with $\Delta t = -2.5, -5.0\text{s}, -7.5, \dots$ ns. If these less populated bunches are 2.5 ns spaced in time from each other, they are referred to as *Ghost* bunches and if 5.0 ns, they are referred to as *satellite* bunches see figure (3.3).

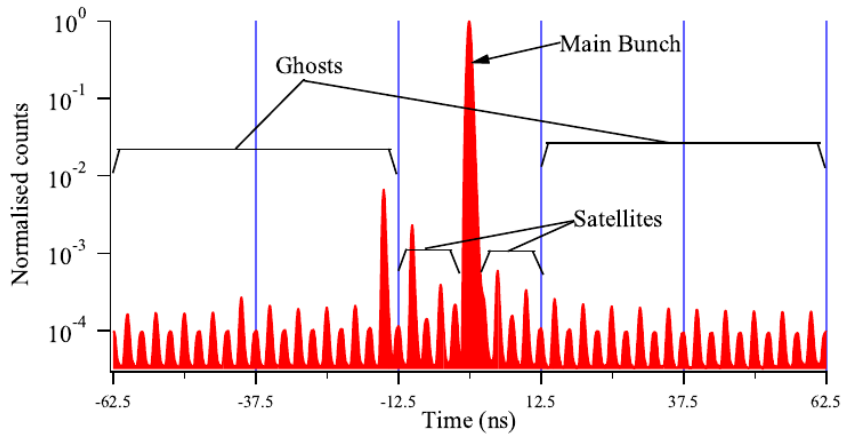


Figure 3.3: Longitudinal Profile taken with LDM detector showing definition of Ghost/Satellite bunches with respect to main bunches.

The presence of ghost/satellite bunches increase the uncertainty in LHC luminosity measurements and can also generate proton-proton interactions in the collision region. Effects on ghost/satellite bunches on instantaneous luminosity measurements have been studied by both CMS, ATLAS and ALICE detectors [?] with their profile compared to main bunch bunches. CMS uses energy deposits in the endcap calorimeters with time space equivalent to those of ghost/satellite bunches while in ATLAS, they have also introduced a new detector called the Longitudinal Density Monitor (LDM) to study ghost/satellite bunches. The results are shown in the figure (3.4).

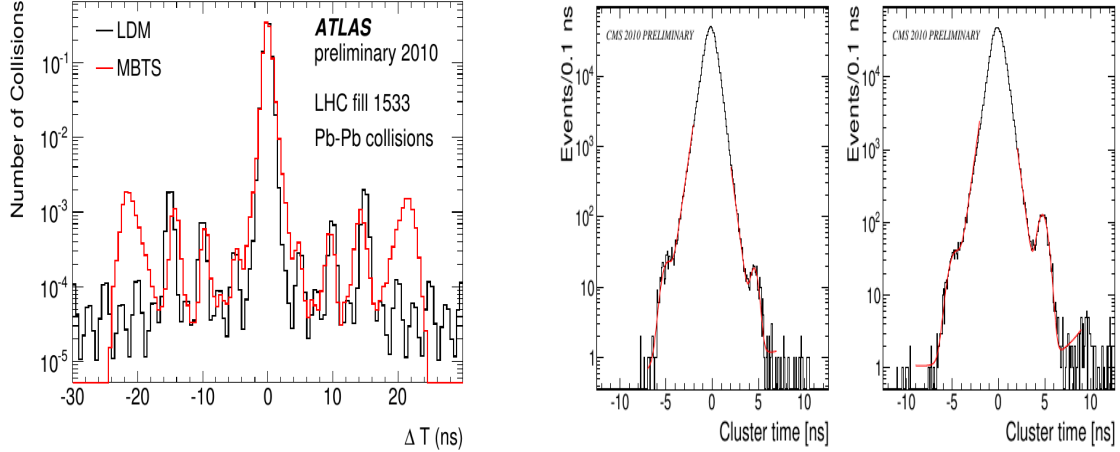


Figure 3.4: (left) Arrival time distribution(red) of ATLAS MBTS for LHC fill 1533 during 2010 Pb-Pb run and LDM profile(black) for Beam2(same for Beam1).

(Right) Timing of Clusters in the CMS endcap calorimeters for fill 1089:Left: EEP detector(left side of IP $z < 0$) Right: EEM detector(right side of IP, $z > 0$). NB: Plots taken from [41] and [42]

There is the possibility that ghost/satellite - ghost/satellite and ghost - Beam1/Beam2 collisions will happen generating events at the CMS detector. This is a major background in the search for delayed photons or objects in general as these collisions can occur *in-time*(Beam1- Beam2) collisions or *out-of-time* collisions. It is thus imperative to be able to quantify this contributions in any search analysis. We will show in future studies we have performs to both “*guesstimate*” and quantify these contributions in our search analysis.

Beam Halo

In addition to ghost/satellite bunches generating collisions events during collision, protons in ghost/satellite bunches can interact with collimators or gases such as H₂, CO₂ and others in the beam pipe leading to the production of high energy muons which later bremsstrahlung and shower directly in the calorimeter detectors. Main bunches due to betatron oscillations(departure of particles from nominal orbit in the transverse direction) can also through inelastic scattering with gas molecules in beam pipe about 550 m up from interaction point (IP)(since beam cleaning in not being 100% efficient), scattering on tertiary collimators (TCT) about $z = 150$ m from IP and beam

dump at about 150 m upstream CMS detector, produce through cascade decay energetic muons(sometimes muons with about 1 TeV) which bremsstrahlung in calorimeter detectors.

This kind of background from beam is referred to as *Machine Induced Background* (MIB) or *Beam-Induced Background* (BIB) and its contribution is called non-collision backgrounds as these are events observed in the detectors but not produced from the interaction point (IP). Throughout these thesis, we will refer to this kind of events as *Beam Halos or halos*. Because, they produce very high transverse momentum photons which can also be miss-identified as jets arriving in-time of out-of-time, they are a very important background in any analysis. In the later section, we will also show how we have developed new methods to identify and reject these kind of events and estimate its possible contribution to our analysis.

3.2 Compact Muon Solenoid

3.2.1 Overview

The goal of the Compact Muon Solenoid (CMS) detector is to identify particles by measuring their energies, momenta and track if applicable, as they pass through the detector. It is for this reason that the CMS apparatus is a general purpose particle detector operating about 330 feet underground at point 5 (P5)LHC in Cessy, France. Its main feature is a superconducting solenoid of 6 m internal diameter providing a field of 3.8 T necessary for good momentum resolution. This field encloses and all-silicon pixel serving as a vertex detector and a strip tracker for charged particle track reconstruction, a lead-tungstate scintillating-crystals electromagnetic calorimeter (ECAL) and a brass-scintillating sampling hadron calorimeter (HCAL). Very long lived particles like muons are measured in gas-ionization detectors embedded in the flux-return iron-yoke located at the outermost section of the detector. It has a simple cylindrical structure consisting of barrel and endcap detectors and an extensive forward calorimetry and detectors to provide a near 4π solid angle assuring good hermetic coverage. The CMS apparatus has an overall length of 21.6 m, a diameter of 14.6 m, and weighs 12,500 tonnes.

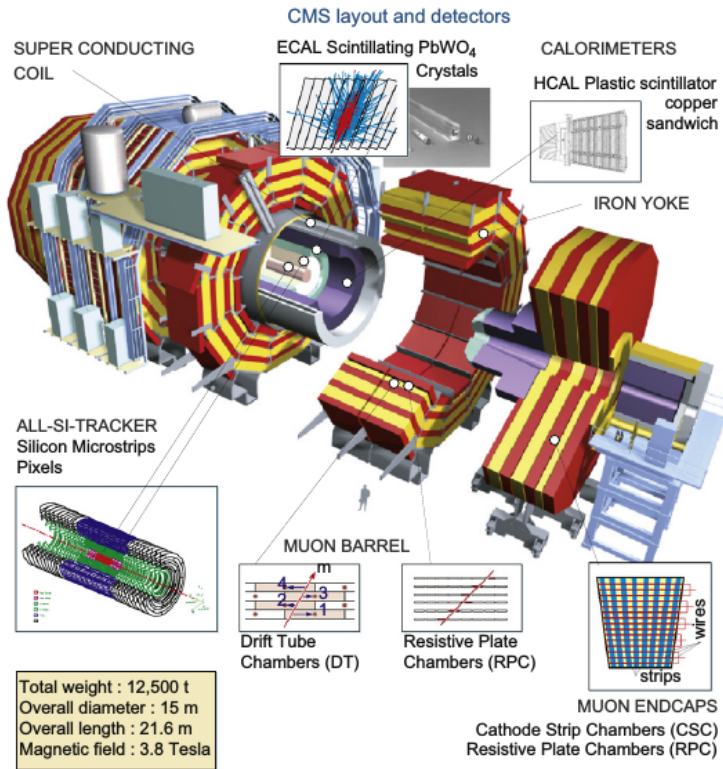


Figure 3.5: CMS Detector showing the different subdetectors and their material.

The CMS detector performance can be summarised as seen in table (3.2.1) with the material type in each sub-detector.

CMS Detector and Resolution			
Subdetector	Quantity	Resolution	Uses
Tracker	Momentum[GeV/c]	$\sigma_T/p_T \approx 1.5 \times 10^{-4} p_T + 0.005$	Silicon Pixels and Strips
ECAL	Energy[GeV]	$\sigma/E \approx 3\%/E + 0.003$	PbWO ₄ Crystals
ECAL	Time[ns]	$\sigma(\Delta t) = \frac{N}{A_{eff}/\sigma_n} \oplus \sqrt{2}\bar{C}$	PbWO ₄ Crystals
HCAL	Energy[GeV]	$\sigma/E \approx 100\%/E + 0.05$	Brass + Scintilator
Muon Chambers	Momentum[GeV/c]	$\sigma_T/p_T \approx 1\% \quad 50 \text{ GeV to } 10\% \quad 1 \text{ TeV}$	inner tracker + Muon Systems
Magnetic field	B-field strength[T]	3.8 T + 2 T	Solenoid + Return Yoke
Triggers	On/Off-line	Levels	L1(On-line) +HLT(Off-line)(L2+L3)

Table 3.2: CMS Detector Material and Resolution (Time resolution: $N \approx 35$ ns, $\bar{C} \approx 0.020$ ns [?])

The CMS uses a coordinate system where the origin coincides with the center of the detector also known as the nominal collision or interaction point (IP). The direction of x , y , and z -axis with the z -axis pointing towards the Jura Mountains from P5 are shown in figure (3.2.1). A more convenient coordinate system used in expressing quantities of particles is the polar coordinates. Here, the CMS uses the azimuthal angle phi measured from the $x - y$ plane with $\phi = 0$ being the x -axis and $\phi = \pi/2$ the y -axis. The radial distance in this plane is denoted R and the polar angle $theta$ measured from the z -axis is related to the *pseudo-rapidity*, η through the relation:

$$\eta = -\ln \tan\left(\frac{\theta}{2}\right)$$

. The co-ordinate system (η, ϕ, z) and its radial distance R defines a point in the CMS detector whose volume is a cylinder.

The CMS Detector at point 5 of LHC

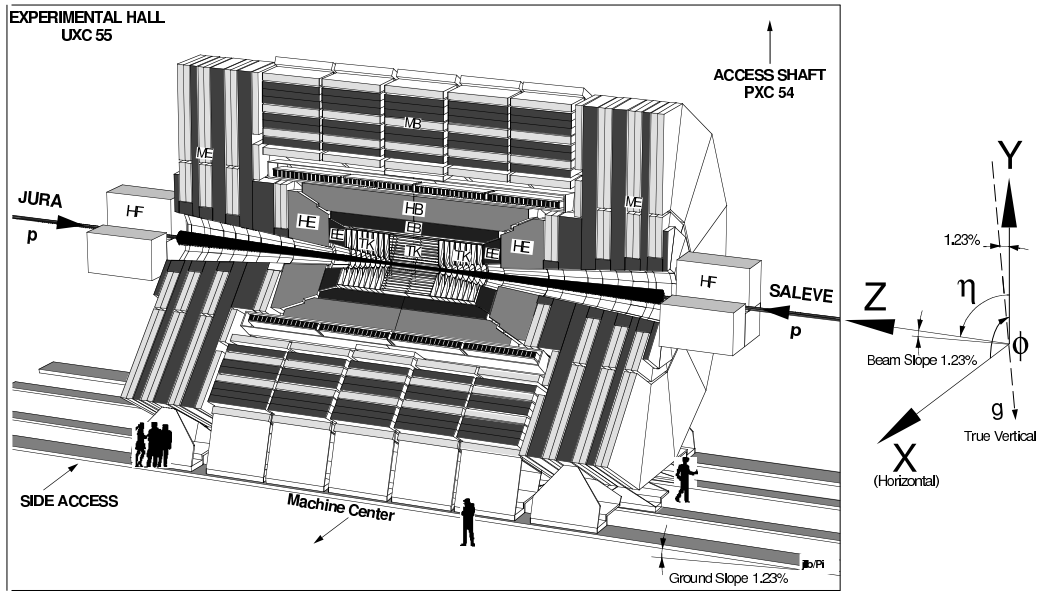


Figure 3.6: Schematic diagram of CMS detector view showing definition of coordinates as used by CMS.

In CMS, quantities such as *transverse momentum* (p_T), *transverse energy* (E_T) and *transverse missing energy* (E_T^{miss} or MET) are used to distinguish a particle's quantities in the transverse plane($x - y$ coordinate) from those along the longitudinal direction(z coordinate) or beam line. In addition to these transverse quantities, cone-like structure with the cone radius is defined as

$$\Delta R = \sqrt{\Delta\eta^2 + \Delta\phi^2}$$

are used to measure the distance between two objects in the $\eta - \phi$ plane. These cone-like structures are used for particle isolation and identification purposes. In the next sections, we describe the characteristics and functionality of each of the CMS subdetectors introducing some additional details for those used in our analysis.

3.2.2 Tracker

Particles produced from proton-proton collision traverse the tracker sub-detector first. The job of the tracker is to measure the trajectory of charged particles, which are curved because of the magnetic field produced by the magnetic coils. By measuring the curvature of these particle, the particle's momentum can be measured and its charge determined. The tracker is a silicon based detector and thus operates under the concept of ionization. It occupies a volume of 2.4 m in diameter and 5.4 m in length, consisting of pixel and strip sections geometrically arranged in cylindrical layers of barrel and disc-shaped endcaps, enclosed within the calorimeters. These sub-detectors all sit inside the 6 m in diameter solenoid magnet operating at 3.8 T. Figure (3.7) depicts a schematic picture of the tracker with three barrel layers covering a region of radius from 4 cm to 15 cm in radius and two endcap discs within 49 cm on either side of the collision point along the z axis; ten barrel layers and twelve endcap disks per side of silicon strip detectors covering a region with radius from 15 to 110 cm and within 280 cm on either side of the LHC beam axis. The total tracker acceptance region in pseudo-rapidity is $|\eta| < 2.5$. The pixel detector is used for identifying the primary and secondary vertices of particles while the inner tracker of strip detector is for tracker reconstruction.

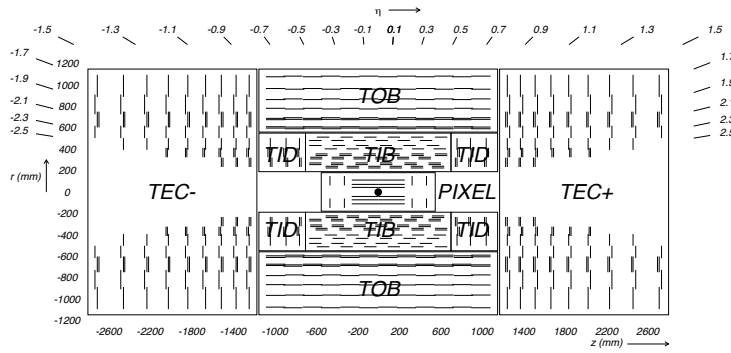


Figure 3.7: Schematic diagram of CMS Tracker showing the silicon pixel detector region (inner closer to LHC beam) and silicon strip region (outer).

Pixel

The pixel vertex detector occupies the inner most region, very close to the interaction region. Providing high-resolution and three-dimensional patterns of space points using

silicon pads as pixels, the primary vertex and secondary vertices arising from the decay of heavy and relatively long-lived particles such as B-mesons containing b-quarks can be identified. This is also known as impact parameter measurements. The pixel covering a region of pseudo-rapidity $|\eta| < 2.4$ complements the track finding by providing additional space points to seeding hits in the inner tracker. Each pixel has a size of $100 \times 150 \mu\text{m}^2$ covering a total area of $\approx 1 \text{ m}^2$ and there are 66 million pixels read out by 16000 readout chips on the silicon sensors. The pixel is organised in three 53 cm long barrel layers (Pixel Barrel=PXB), positioned at radii of 4.4, 7.3 and 10.2 cm and two disks each per side (Pixel Forward=PXF), placed at ± 34.5 cm and ± 46.5 cm from the interaction point and covering a radii between 6 and 15 cm. This guarantees each charged particle track crosses at least two layers of pixels. This arrangement ensures that the pixel detector provides precise tracking points in the $r - \phi$ and z responsible for small impact parameter resolution of about $\sim 15 \mu\text{m}$. Small impact parameter resolution is important for precise secondary vertex reconstruction and position resolution crucial in the identification of objects produced with displaced vertices with life-time of about $\tau \approx 10^{-12} \text{ s}$ like mesons such as $B^{0,\pm}$, $D^{0,\pm}$, τ^\pm , which may travel a distinguishable distance ($c\tau \approx 100 \mu\text{m}$ before decaying). Because of very high radiation dose of about 100 Mrad absorbed by the pixel detector, there is currently upgrade of the complete pixel detector in preparation of LHC Run 2.

Silicon Strip Tracker

CMS silicon inner tracker surrounding the pixel detector allows for the tracks of promptly produced charged particles with $p_T = 100\text{GeV}/c$ to be reconstructed with a resolution in the transverse momentum p_T of about $\sim 1.5\%$. High momentum particles are less curved by the magnetic field than low momentum particles. Therefore, the tracker works complementary with the calorimeter and muon detectors to ensure improved momentum resolution at all particle energies. The silicon micro strip tracker covers a tracking volume up to radius of 1.2 m with a length of 5.6 m. It is organised in three parts: The inner tracker with four barrel layers (Tracker Inner Barrel=TIB) and three disks per endcap (Tracker Inner Disks=TID), 6 outer barrel layers (Tracker Outer Barrel=TOB) closed by 9 wheels on both sides. (Tracker EndCap=TEC). The silicon strip is made of 15148 silicon microstrip detector modules. Each module has a set of sensors. It occupies

an active area of $200\ m^2$ providing a coverage in pseudo-rapidity up to $|\eta| < 2.5$. The TIB/TID delivers up to 4 $r - \phi$ measurements on a trajectory using $320\ \mu\text{m}$ thick silicon micro strip sensors arranged parallel to the beam direction in the barrel and radial on the disks. The strip pitch is $80\ \mu\text{m}$ on layer 1 and 2 and $120\ \mu\text{m}$ on layer 3 and 4 of the TIB, leading to a single point resolution of $23\ \mu\text{m}$ and $35\ \mu\text{m}$, respectively. The TID also have varying pitches with both the TIB/TID enclosed by the TOB. The layering structure can be seen figure (3.2.2). The nearly 9.6 million silicon strips provide a spatial resolution measured to be about $10\ \mu\text{m}$ for $r - \phi$ measurement and about $20\ \mu\text{m}$ for z measurement necessary for particle trajectory reconstruction. The combined pixel and micro strip modules allows for nearly 75 million readout electronic channels in the tracker.

3.2.3 Calorimeter

A calorimeter is a device which absorbs a good fraction of energy of an incident particle and produces a signal with an amplitude proportional to the energy absorbed. This absorption is via a cascade production of secondary particles where the incident energy is directly proportional to the number of secondary particles. CMS uses two types of calorimeters: Electromagnetic calorimeters (ECAL) for absorbing the energy of electromagnetic particles such as photons and electrons and a sampling calorimeter or Hadronic calorimeter (HCAL) made of more than one type of material for absorbing the energy of hadrons such as kaons and pions through hadronic interactions. The combined calorimeter detectors of CMS covers a region in $|\eta| < 5$ making it nearly hermitic for missing energy measurements. The ECAL and HCAL are arranged in a layered manner as seen in figure (3.2.3) such that electromagnetic particles can be distinguished from hadronic particles by comparing the depth of the particle shower penetration in both calorimeters.

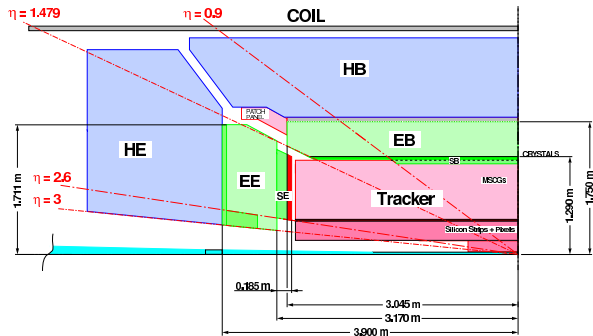


Figure 3.8: Schematic diagram of CMS calorimetry system with HCAL enclosing ECAL in the Barrel and Endcap regions.

Electromagnetic Calorimeter

The main particles to detect using ECAL detectors are photons and electrons. High energy photons and electrons are detected through their interaction with the material of the ECAL detector. During this interaction which can be either through electromagnetic showering also known as *bremsstrahlung* or electron-positron pair production, the incoming photons or electrons deposit practically almost all of their energy. The material for the CMS ECAL detector are lead-tungstate (PbWO_4) crystals. There are 75848 lead-tungstate (PbWO_4) crystals mounted in a barrel (EB) and endcap (EE) structure. PbWO_4 crystal is the appropriate choice for calorimetry by CMS for operation in the LHC environment because of its a high density (8.28 g/cm^3), short radiation length ($X_0=0.89 \text{ cm}$) and a small Molière radius (22 cm). This dense nature allows for the electromagnetic shower to develop early and therefore very likely to be fully contained within a compact device. In a high radiation dose and fast timing (25 ns bunch spacing) environment like the LHC, the choice of PbWO_4 crystals is justified because of their high radiation resistance and short scintillation decay time of the same order of magnitude as the LHC bunch crossing time:about 80% of the light is emitted in 25 ns. Since the ‘amplitude’ or “probability” of a high energy photon or electron interacting with an ECAL material through (*Bremsstrahlung*) and pair production is proportional to the nuclear charge or number of electrons, Z of the material, PbWO_4 which is a high Z material is once again CMS preferred choice for calorimetry. The small Molière radius of PbWO_4 crystals ensures that on average about 95 % of the electromagnetic shower

energy is contained within the crystal volume therefore reducing the transverse spread of the electromagnetic cascade arising from multiple scattering of electrons. This improves on the estimation of the transverse position of impact of the incident particle and the fine granularity provides good precision for measuring the energy of an incoming electromagnetic particle and thus better energy resolution.

The barrel section of the ECAL covers a pseudo-rapidity of $|\eta| < 1.479$. The EB has 61,200 crystals providing a granularity of 360-fold in ϕ and (2×85) -fold in η . The crystals are mounted in a quasi-projective geometry to avoid cracks aligned with a particle trajectories, so that their axes make an angle of 3% with respect to a line vector from the nominal interaction vertex in η and *phi* directions. These EB crystals have approximately 0.0174×0.0174 in $\eta - \phi$ or $22 \times 22 \text{ mm}^2$ at the front face and $26 \times 26 \text{ mm}^2$ on the rear face. each crystal is 230 mm long corresponding to about $25.8 X_0$ radiation length. The crystals are contained in a thin-walled aveolar structure made with aluminium called submodule with their radial distance from the center of the face of the crystals to the beam line is 1.29 m. Each submodule are arranged into 4 modules of different types according to their η position with each module having about 400 to 500 crystals. The four modules make one supermodule containing 1700 crystals. The aluminium surface is coated to avid oxidation hence coloration which causes decrease in transparency. On the rear end of each EB crystals, is glued two Avalanche Photodiodes (APD) whose purpose is to collect the scintillating light from the crystals converting light into current which is further collected by the read-out electronics.

The endcap sector occupy a pseudo-rapidity region of $1.479 < |\eta| < 3.0$ with Preshower (ES) detector made of silicon strip sensors interleaved by lead placed immediately in front of it. The purpose of the preshower detactor is to help separate converted from unconverted photons. There are two endcaps located in the $+z$ side of the nominal interaction and denoted EE+ and on the $-z$ side denoted as EE-. The longitudinal distance between the nominal interaction point and the center of the surface of the crystals in EE is 3.154 cm. Crystals in the EE are of identical shape group in units of 5×5 crystals called *supercrystals or SC*. Each endcap is divided into two halves called *Dees* with each Dee holding 3662 crystals. The crystals are arranged in $x - y$ grid with their front face and rear cross section of $28.62 \times 28.62 \text{ mm}^2$ and $30 \times 30 \text{ mm}^2$ respectively. Ecah crystal is 220 mm ($24.7 X_o$) in length. Vacuum Phototriodes (VPT) is glued on the

rear face of each crystal for scintillating light collecting and conversion into electrical signals. These photodiodes and triodes are used because of their high gain and the fact that they are not affected by the high magnetic field. Although the light-yield for PbWO_4 is rather low ($\approx 70\text{photons/ MeV}$), the photodiodes have internal gain (50 for APDs and 10 for VPTs) and good quantum efficiency of 75 % for APDs and 20 % for VPTs of the emission wavelength. This makes it possible that signals from incident particles with energies from a few to high GeV can be recorded. APDs and VPTs are the standard choice of photo-detectors by CMS because of their high resistance to radiation and smooth operation in a strong magnetic field environment. Photodiodes like APDs and VPTs are similar to silicon photodiodes, with the exception that they have a buried p-n junction reversed-biased at a very high electric field. The photo electrons arriving at the junction undergo avalanche multiplication giving the device a gain. The signals from the APDs and VPTs are digitized by voltage-sensitive analogue-to-digital converters are later converted to light signals which are then transported using long optical fibres to the counting room located adjacent to the experimental cavern.

The energy resolution and geometric structure of the ECAL ensures that the photon or electron's arrival position at ECAL, energy and time and even the direction and shape of its electromagnetic shower in the crystals can be measured and identified respectively with good precision.

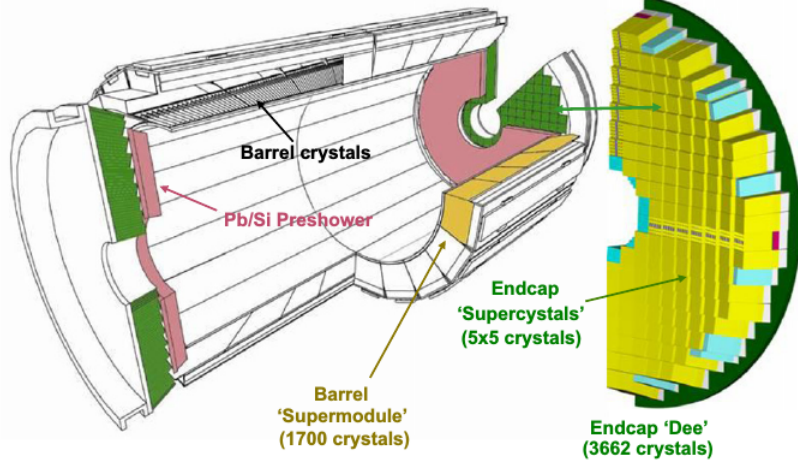


Figure 3.9: Layout of the CMS electromagnetic calorimeter showing the arrangement of crystal modules, supermodules in the barrel with the preshower in front of endcap with supercrystals.

Hadronic Calorimeter

Hadrons like protons, neutrons kaons and pions are unlike electromagnetic particle strongly interacting (strong force is the force that binds nuclei together). A hadronic shower is formed when an incident hadron undergoes an inelastic collision with the nucleus of the absorber material producing secondary hadrons which as they go through successive layers of absorber material interact inelastically with other nuclei to produce further hadrons etc. The hadronic cascade loses about 30 % of incident hadron energy through nuclear excitation of the nuclei of atoms of the absorber material. Hadronic showers start to develop later with more lateral spread and larger in the longitudinal dimensions than electromagnetic showers. This is why the hadronic calorimeter (HCAL) is made of alternating plates of brass and plastic scintillator encompassing the ECAL. The scintillating light is readout using wavelength shifting optical fibres by photosensors in the barrel and endcap. The photosensors are hybrid photodiodes (HPD). There are ongoing upgrades to replacing the HPDs with silicon photon multipliers (SiPM). The hadronic barrel(HB) and hadronic endcap(HE) of the HCAL cover a region in pseudo-rapidity of $|\eta| < 3$. While the Hadronic Forward (HF) occupies a pseudo-rapidity region of $3 < |\eta| < 5$. The HB calorimeter is an assembly of two half barrels each composed of 18 identical 20° wedges in ϕ . Each wedge is made of flat brass alloy absorber plate parallel to beam axis with the innermost and outermost layers made up of stainless steel interleaved by plastic scintillating tiles. The first active layer is situated directly behind the ECAL in order to actively sample low energy showering particles from the support material between the ECAL and HCAL. Each scintillating tile has a size of $\Delta\eta \times \Delta\phi = 0.087 \times 0.087$ and is instrumented with a single wave length shifting fiber(WLS) for better collection of light. The summed optical signals or light are converted into fast electronic signals by photo-sensors called hybrid photo-diode(HPD). This inhomogeneous design gives the HCAL, an energy resolution of $\Delta E/E \approx 0.5/\sqrt{E(\text{GeV})}$ for particles with energy above 250 GeV, much lower compared to that of homogeneous ECAL detector.

The forward hadronic (HF) calorimeters placed upstream have scintillating tiles called Beam Scintillation Counters (BSC) which in coincidence with the beam pick-up monitors (BPTX) detector helps to eliminate beam background contamination at the trigger level and is also useful for detection of hadrons in the forward region. HF

made up of steel absorbers embedded in radiation hard quartz fibers running parallel to the beam axis and providing a fast collection of Cherenkov light. The signal results from Cherenkov light emitted in the quartz fibres embedded in the steel matrix in response to charged particles. The Cherenkov calorimeter have long and short fibers which are positioned alternatively separated by 5 mm with readouts for better sampling of the different shower components. The goal of this hardware design is to give better compensation for different shower components in the hadronic shower. The HF section enables the HCAL to pick up myriad of particles coming out of the collision point. Quartz fibre has high resistance to the high radiation does in the forward detectors and light production is through Cherenkov method than scintillation in HB and HE calorimeters.

The purpose of the HF detector is to provide a full hermetic 4π phase space coverage required for missing transverse energy calculation or MET. MET is the established as signal for very weakly interacting particles like neutrino and supersymmetric particles like gravitino which travel through the detector undetected. For $|\eta| < 1.74$ region, the HCAL cells are 0.0870.087 rad in pseudo-rapidity(η) and in azimuth (ϕ). In the (η, ϕ) plane, and for $|\eta| < 1.48$, the HCAL cells map on to 5×5 ECAL crystals arrays to form calorimeter towers projecting radially outwards from close to the nominal interaction point. At larger values of $|\eta|$, the size of the towers increases and the matching ECAL arrays contain fewer crystals. Within each tower, the energy deposits in ECAL and HCAL cells are summed to define the calorimeter tower energies subsequently used to provide the energy and direction. The ratio of the energy deposit if a particle in the ECAL crystals to that in the HCAL towers is used to distinguish between true photons from neutral hadronic showers.

3.2.4 Muon Chambers

Muons are long-lived particles capable of travelling across the entire lateral section of the CMS detector into the muon chambers producing tracks in the tracker and depositing very little fraction of their energy in the calorimeters. The muon chambers uses ionization and the magnetic field from the return iron yokes to curve the tracks of charged long-live particles like muons, measuring their momentum and finally detecting them. There are three different types of muon chambers: the drift tubes (DT) chambers in the

barrel, cathode strip chambers (CSC) in the endcaps and resistive plate chambers (RPC) glued to the DT and CSC chambers. Four layers or stations of DT/RPC and CSC/RPC are embedded in an interleaved style with the iron yoke for track reconstruction and triggering. Figure (??) provides a longitudinal view of the CMS detector showing the position of the stations. The DT and CSC record track segments characterised by the position of the track and the bending angle which is used to determine the precise transverse momentum and charge of a given particle during off-line reconstruction. The RPCs are dedicated trigger chambers used to determine the candidate muon's approximate transverse momentum and bunch crossing number where the particle originates. The RPC has a timing resolution of about 3 ns.

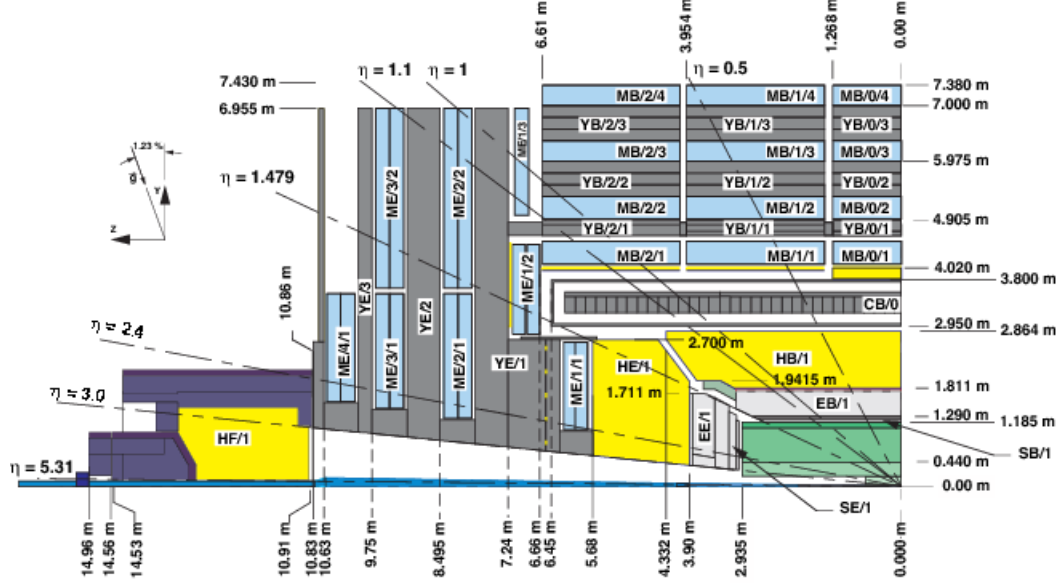


Figure 3.10: Longitudinal view of CMS showing the coverage range of its sub-detectors.

3.2.5 Particle Detection

Particle types that are identified using the CMS detector include electrons, photons, hadrons, neutrinos and other weakly interacting particles. These particles depending on their charge, nature of interaction and lifetime can be identified either using some or all the sub-detectors of the CMS detector. The figure (??) show a transverse slice of the CMS detectors with tracks in the tracker and muon sub-detectors and calorimeter energy deposit showing how different particles interact with the material in

different sub-detectors thus ensuring their unique identification and reconstruction in the detector.

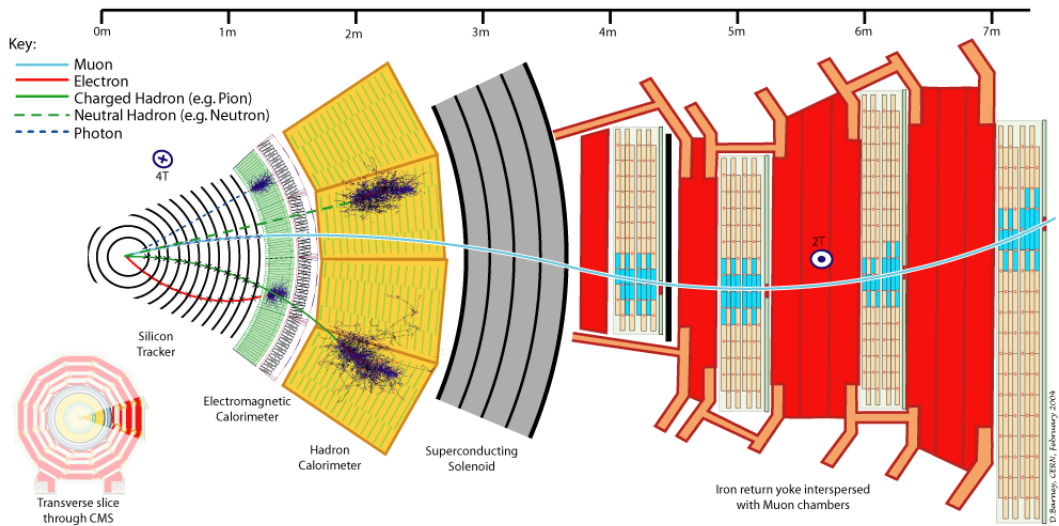


Figure 3.11: Transverse slice of the CMS detector showing how different types of particles interact and hence identified using this detector.

3.2.6 Triggering

In CMS, there are a billion interactions happening every second which means data from protons colliding 40 million times every second equivalent to the 25 ns LHC bunch crossing time interval has to be process and analyse before the next collision happens. Obviously this is impossible and infact, not every proton-proton collision will lead to the production of an interesting physics event. Thus one has to find a way of selecting only events produced from head-on proton collision with sufficient amount of energy. Even with this selection, it is not possible to process a single event in a 25 ns time frame. Thus, the CMS uses a two level triggering system for selecting interesting events and a pipeline system to temporarily store and process information from many interactions at the same time. Thus so as not to confuse particles from two different events, the CMS triggering system has a very good timing resolution and synchronization so that signals from millions of electronic channels and synchronised and identified to be produced by the same event. The CMS triggering system consist of two layers: The Level-1 (L1) and High Level Triggers (HLT) triggers. L1 triggers are hardware designed electronic

system while HLT is a farm of more than 1000 standard computers running the HLT event selection algorithm. Thus event selection begins at the L1 and HLT triggers. The L1 trigger electronics is implemented in FPGA and ASIC technology and consists of a calorimeter, muon trigger and a global trigger boards. The global trigger board makes the final decision based on the calorimeter and muon triggers to reject or keep an event for further processing at the HLT trigger. The L1 trigger is responsible for selecting the best 100,000 events each second from the initial 1 billions events from interactions happening every second. The pipeline system is used during the L1 trigger latency time of about $3.2 \mu\text{s}$. The HLT trigger using assimilated and synchronised information from different parts of the detectors recreates the entire event. the HLT runs complex algorithm relating to physics objects like matching tracks to hits from the muon chambers or energy deposits above a certain threshold in the calorimeters without tracks for electromagnetic objects. By the time this selection process is complete, there are now only 100 events per second with the remaining 99,900 thrown away. With the average event size of about 1 Megabyte, in a stable and effective LHC proton collision year or 10^7 seconds, the CMS produces about a Petabyte of data which is stored in tapes for later offline analysis. Due to the large amount of data, such analysis are performed using clusters of computers geographically connected to each other in a virtual computing environment called the LHC Computing Grid (LCG) to which the CMS is a member. This data is made available to 7 primary and later to secondary tier centres consisting of national research laboratories and universities around the world using a data transport system term Physics Experiment Data Export (PhEDEx).

Chapter 4

Timing Reconstruction and Calibration

The measured arrival time of an electromagnetic object is extracted from its energy deposited on ECAL crystals. The tiny energy hit deposited on each crystal and reconstructed is called a *rechit*. The recorded time of the photon is the crystal calibrated time where its Time-Of-Flight (TOF) and the time used in transmitting the recorded signal from the front-end detectors to the back-end readout electronics is calibrated such that on average the measured ECAL crystal time is zero for a photon produced at the nominal proton-proton collision point traveling at speed of light to when it impinges at the surface of the crystal. There are algorithms for extracting and calibrating ECAL crystals using the rechit time. The calibrated time is the reconstructed time (T_{RECO}) for a given reconstructed ECAL object or particle. Measuring the difference of the ECAL measured time between any two reconstructed objects (which can be individual crystals or electromagnetic objects) arriving from the same nominal point, which in principle are both expected to have the same time, gives a reliable measurement of the timing resolution of the sub-detector including the crystal-to-crystal synchronization factor. In ECAL timing, the photon reconstructed time, T_{RECO} , can be calculated using either of the following methods:

1. **Seed Time:** The time of the highest energy crystal or rechit in the highest energy basiccluster (about 9 crystals) of the photon supercluster (about 25 crystals). We

denote this time as T_{SEED} ,

2. **The Mean Time:** This is the error weighted average time of all the crystals in the photon seed basiccluster denoted as $T_{CLUSTER}$ or T_{MEAN} given by equation 4.1.

$$T_{CLUSTER} = T_{MEAN} = \frac{\sum_{i=1}^N \frac{T_{RECO,i}}{\sigma_i^2}}{\sum_{i=1}^N \frac{1}{\sigma_i^2}} \quad (4.1)$$

N is the number of crystals in seed basiccluster of photon supercluster, T_i and σ_i are the reconstructed time and uncertainty on the time of each crystal respectively.

4.0.7 Electromagnetic Calorimeter Readout Chain

The ECAL electronics readout system fully described in [44] is a light-to-light system. Energy from an incoming electromagnetic object is absorbed and converted into scintillating light by PbWO₄ crystals. The scintillating light from these crystals is received and converted into electrical signals by Avalanche Photo-Diodes (APD) and Vacuum Photo-Triodes (VPT). These electrical signals are transferred to a Multi-Gain Pre-Amplifier (MGPA) which amplifies, shape, digitized and finally convert these signals back into light signals where they are transported using optical fibers into an off detector electronics in a counting room at point 5. We classify the full readout chain of the ECAL electronics readout system into an *on-detector* and *off-detector* electronics. These electronics system are connected by 100 m optical fiber links for transferring the light signals. The on-detector electronics reads a trigger tower consisting of 5×5 crystals arranged in $\eta \times \phi$ grid in barrel (EB) and $x - y$ grid in endcap (EE). Five Very Front End (VFE) boards (reading out data from 5 crystals each), one Front End board (FE), two (EB) and six (EE) Giga Optical Hybrids (GOH), one Low Voltage Regulator (LVR) board and a Mother Board (MB) make up the complete on-detector electronics. Electrical Signals from the APDs (in EB) are accepted by the VFE equipped with a Multi-Gain Pre-Amplifier (MGPA), a 12-bit Analogue to Digital Converter (ADC) and a buffer. The MGPA (an Application Specific Integrated Circuit (ASIC) developed in 0.25 μm technology), pre-amplifies, shapes and then amplifies the signals through three amplifiers with gains of 1, 6 and 12. For the VPT (EE), these signals first pass through a High Voltage (HV) filter card which acts as a moderator separating very high voltages

caused by the increase radiation in the EE. The full scale of the APDs and VPTs are 60 pC and 12.8 pC corresponding to ≈ 1.5 TeV and 1.6-3.1 TeV respectively. The full shaping of the signal takes about 40 ns. The noise for gain 12 is about $8000e^-$ for APD configuration and about $4000e^-$ for VPT configuration. The 3 analog output signals of the MPGA are digitized in parallel by a multichannel 40 MHz, 12-bit analog-to-digital converters (ADC). This ADCs have an effective number of bits of 10.9. The highest non-saturated signal is selected as the output signal and reported as 12 bits of the corresponding ADC with 2 bits coding the ADC number. It is possible, that when the signal is saturated, a wrong signal amplitude can be produced leading to some amplitude dependence of the readout time. This effect has been studied for Gain 1 and 6 transitions and the relevant corrections factors for adjusting timing measurements due to this effect produced, validated and applied. A schematics picture of the showing the readout chain of the FE with its MPGA and ADCs showing the shaping and digitization process is shown in figure 4.1.

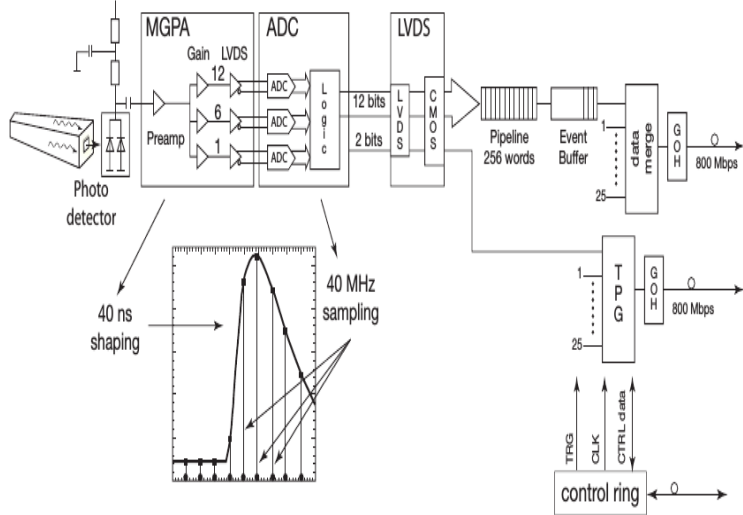


Figure 4.1: Schematic diagram of the CMS ECAL ReadOut Chain.

To protect the electronics from extreme radiating, a radiation-hard buffer (LVDS) adapts a low voltage differential output signal of the ADC to input into the FE. Signals from five identical channels are integrated and read into VFE card with a Detector Control Unit for measuring APD leakage currents. The noise from each VFE is typically

1.1, 0.75, 0.6 ADC counts for gains 12, 6 and 1 respectively. This would be about 40 MeV for gain 12. Digitized data from 5 VFE cards are fed into each FE through the LVDS and stored in 256-word-deep dual-ported memories called pipelines. Data pipelines can be stored for up to 128 bunch crossings. The FE is base on a ASIC called FERNIX holding and the logic is to calculate the energy of 5 channels once every bunch crossing. This energy is summed in strips of 5 crystals along ϕ . This means each VFE is serviced by a FERNIX chip. In the case of the EE, the five strip energy sum are transported by GOH to the off-detector electronics Trigger Concentration Card (TCC) while for EB, there is a sixth FERNIX which sums the five strips energy sums and calculates an electromagnetic bit which is used to identify electromagnetic shower candidates on the basis of their shower profile in a trigger tower. The trigger tower (5×5 crystals) energy sums and the electromagnetic bit is transmitted to the TCC through the GOH. This process is referred to as Trigger Primitive Generation (TPG). Once a Level-1 trigger signal is received, the ten 40 MHz samples for each channel are transmitted to the off-detector electronics Data Concentration Card (DCC) using an identical GOH. This takes about 7.5 μ s. The VFE and FE cards are controlled using a 40 MHz digital optical link system controlled by the off-detector Clock and Control System (CCS). The Off-detector electronics consist of different types of electronic boards (the CCS, TCC and DCC modules) sitting in an 18 VME-9U crates and a 1 VME-6U crate holding the Selective Read-Out Processor (SRP). This system is serving both the trigger and the Data Acquisition Systems (DAQ) paths. In the DAQ path, the DCC performs data read-out and data reduction based on flags of the SRP. While in the trigger path, at each bunch crossing, the trigger primitive generation which began in the FE is finalized and synchronized or time aligned in the TCC before being transmitted to the regional calorimeter triggers. The trigger primitives each referring to a single trigger tower (25 crystal data) consists of the summed transverse energy deposits and the electromagnetic bit characterizing the lateral shower profile of the electromagnetic shower. The accepted signal for accepted events is returned from the global trigger after about 3 μ s and the selected events are read into the data acquisition system to the filter farm where the even rate is further reduced using data from the full detector.

In the regional calorimeter, the ECAL trigger primitives together with the HCAL trigger primitives are used to compute the electron/photon and jet candidates as well

as their transverse energy. The resulting physics objects after passing through the HLT trigger are transferred to the various tier systems for offline full event reconstruction. The ECAL also has a laser calibration systems where laser light is delivered directly to the PbWO₄ crystals using optical fibers. The laser data is used for energy and time calibration of crystals and hardware system. The crystals are energy calibrated because of the decrease in optical transmission due to the formation of color centers in the crystal. The formation of color centers is caused by irradiation. Time calibration using laser data can be performed in case there are hardware timing offset especially during long short down periods of the CMS detectors.

4.0.8 Timing Extraction

The MGPA amplifies and shapes an analog signal from the APD/VPT of a single crystal producing a typical signal pulse shown in figure 4.2.

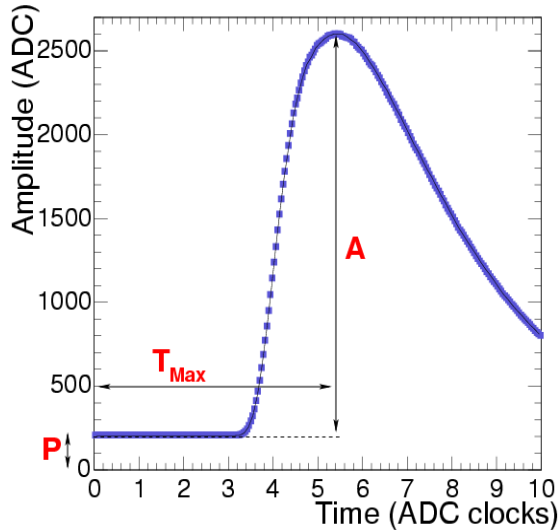


Figure 4.2: Typical pulse shape of a given signal showing signal amplitude and time.

This pulse is digitized into 10 samples by the ADC for data storage purposes. The pulse's amplitude is a measure of the energy deposited in the crystal while the time is extracted from the 10 samples produced by the ADC clock with a sampling frequency of 40 MHz sampling the signal pulse. This extracted time is used as the arrival time of the physics object depositing its energy unto the crystal. The value **P** is the pedestal or

noise read as ADC values in the absence of any signal. A timing algorithm is employed to extract the time. The objective of this algorithm is to use the maximum amplitude value of the pulse, A_{MAX} , and its corresponding maximum value of the ADC time, T_{MAX} to reconstruct an event time. Thus, ECAL timing reconstruction is using the 10 samples of the pulse amplitude to measure T_{MAX} . Obtaining the true A_{MAX} is performed through an energy reconstruction algorithm. Extracting the arrival time is through comparing the pulse shape to a reference pulse shape obtained during early LHC Test Beam results. This reference pulse shape has been obtained from experimental measurements using synchronous LHC events. Figure 4.3(*Left*) shows a distribution of A/A_{MAX} on the vertical axis against $T - T_{MAX}$ on the horizontal axis. T is time and T_{MAX} is the time when the pulse reaches its maximum value, A_{MAX} .

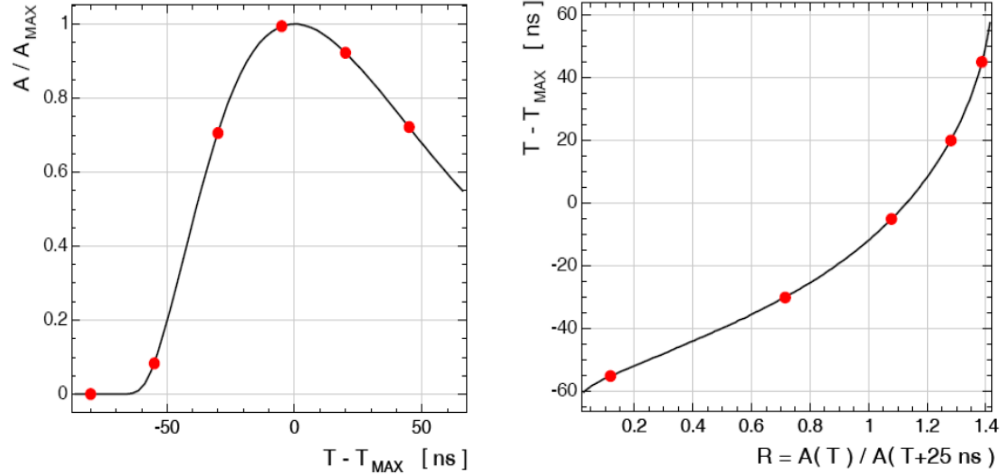


Figure 4.3: *Left*: A measured ECAL pulse shape for each channel. *Right*: $T - T_{MAX}$ Vs $R(T)$ showing the distribution of $T(R)$. Solid line is reference shape or shape from test beam while dots correspond to a 10 discrete samples corresponding to signal from a single event in a single channel or crystal.

This comparison is done by performing an analytic fit to the 10 digitized samples. However, performing this fit directly on the $A(T)$ distribution to obtain A_{MAX} and T_{MAX} is cumbersome and technically inefficient since the amplitude of each sample depends on the pulse shape, the A_{MAX} value and also the relative position of T_{MAX} between each each sample point. This relative position or phase is referred to as “ T_{MAX} phase”. In order to minimize the fit dependence on A_{MAX} and the T_{MAX} phase, we use

a new variable defined as $R(T) = A(T)/A(T + 25 \text{ ns})$ and perform this analytic fit on the distribution of $T - T_{MAX}$ Vs $R(T)$. This $T(R)$ distribution is independent of A_{MAX} and can be very well described using a polynomial of order 7. A distribution of $T(R)$ is shown in figure 4.3(*Right*) with both the four to five samples points (dots) obtained from the ratio $R_i = A_i/A_{i+1}$ from each consecutive pair of samples and the reference pulse shape (continuous line). Each point R_i gives a quick accurate measurement of $T_{MAX,i} = T_i - T(R_i)$. The uncertainty, $\sigma_{T,i}$, on each measurement is a production of the derivative of the function $T(R)$ and the uncertainty on the value of R_i . The uncertainty on the value of R_i depends on three separate uncertainties: the noise fluctuation, σ_n of each sample, the uncertainty in the estimation of the pedestal value which is always subtracted from the measured value and the truncation during 12-bit digitization. These uncertainties are uncorrelated and can be added in quadrature. The reconstructed time and its error of a hit (fraction of energy deposited on a single crystal) is determine using equation 4.2.

$$T_{MAX} = \frac{\sum \frac{T_{MAX,i}}{\sigma_i^2}}{\sum \frac{1}{\sigma_i^2}} ; \quad \frac{1}{\sigma_T^2} = \sum \frac{1}{\sigma_i^2} \quad (4.2)$$

where the sum is over all the 4 or 5 R_i ratios and the assumption is that the weights are uncorrelated.

4.0.9 Timing Resolution

Using the reconstructed time for each channel, we measure the timing resolution for ECAL. First, the timing resolution for ECAL can be parametrized and expressed as a sum in quadrature (uncorrelated) of three major terms contributing to uncertainty in time measurement. These three contributions are: First, the *Noise* (N) term, from electronic noise, coherent movement of the baseline and effects arising in addition to the main or hard proton-proton collision, other soft or less energetic collision producing events called *pile up* (PU) events. Second, the *Stochastic* term (S), from fluctuations in the photon collection time because of finite time during PbWO_4 scintillation. Finally the *Constant* term (C) whose contribution is independent of the energy deposited but rather from effects correlated with the point of shower initiation within the crystal and systematic in the extraction of the time due to different is pulse shape for each channel.

The timing resolution equation showing all these terms is given in equation 4.3

$$\sigma^2(t) = \left(\frac{N}{A/\sigma_n} \right)^2 + \left(\frac{S}{\sqrt{A}} \right)^2 + C^2 \quad (4.3)$$

A is the measured amplitude corresponding to the energy deposited and σ_n is the intrinsic noise for individual sample with a value of ≈ 42 MeV and 140 MeV in the barrel and endcap respectively. $N = 33$ ns measured from Monte Carlo (MC) simulation studies. Contribution from the stochastic term, (S) is considered small, with value of $S < 7.9$ ns·MeV $^{1/2}$.

To measure the timing resolution, a simple experiment was performed in which electron beams with energies between 15 GeV(GeV = Giga electron volts = 10^6 eV, 1 eV = 1.602×10^{-19} joules (J) in energy units) and 250 GeV was directed unto each crystal in a supermodule. The timing resolution measurement is obtained by extracting from the measured distribution of the difference in timing between two crystals sharing energy and from the same electromagnetic shower. The advantage of this approach is that, the contribution from poor synchronization is less as synchronization effects do not affect the spread but rather the average time. However, there are still crystal-to-crystal synchronization effects. Other approaches used to study timing resolution is by taking the time difference between two of a few group of crystals usually 5×5 crystals called basicclusters, between a complete electromagnetic shower.

Using equation 4.3 and neglecting the stochastic term since its contributions are negligible, the timing resolution from two objects (crystal, basiccluster) is expressed as shown in equation 4.4.

$$\sigma^2(t_1 - t_2) = \left(\frac{N}{A_{eff}/\sigma_n} \right)^2 + 2\bar{C}^2 \quad (4.4)$$

where $A_{eff} = A_1 A_2 / \sqrt{A_1^2 + A_2^2}$, $t_{1,2}$ and $A_{1,2}$ correspond to the times and amplitude measured in the two objects and \bar{C} is their residual contribution. We measure the timing resolution by using the standard deviation of a Gaussian fit to the time distribution from each slice in A_{eff}/σ_n distribution. The $\sigma(t_1 - t_2)$ against A_{eff}/σ_n of the extracted standard deviation of each slice is plotted the resulting distribution fitted to extract the noise and constant term. Figure 4.4 show the noise factor $N = (35.1 \pm 0.2)$ ns and $\bar{C} = (20 \pm 4)$ ns as measured from test beams experiments.

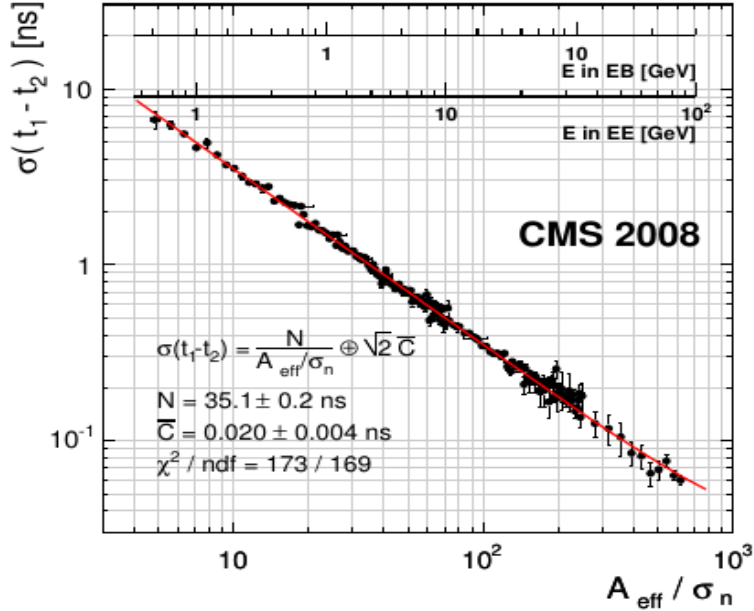


Figure 4.4: Deviation of the timing difference as a function of A_{eff}/σ_n between two crystals sharing an energy in the same electromagnetic shower obtained during electron testbeam measurements. The single crystal energy scales for barrel (EB) and endcap (EE) is overlaid. The fitted results give $N = (35.1 \pm 0.2)$ ns and $\bar{C} = (20 \pm 4)$ ns.

A timing resolution better than 100 ps for energy values A_{eff}/σ_n greater than 400 ADC counts is obtained. This demonstrates that for a perfectly calibrated ECAL crystals and energy deposits of $E > 20$ GeV in the barrel, we can obtain a resolution better than 100 ps.

4.0.10 Timing Calibration Procedure

Timing calibration is performed such that particles traveling along a straight path with speed close to the speed of light, $\beta \approx 1$, produced from proton-proton collisions happening at the CMS luminous region or IP will arrive at the surface of an ECAL crystal with an average time of 0 ns. This implies, particles arriving at an ECAL crystal with significantly and positively large arrival time, are either traveling with very small velocity (slow moving particles, $\beta \ll 1$) or were produced from a decay path which significantly deviates from the obvious straight path connecting the IP to the crystal.

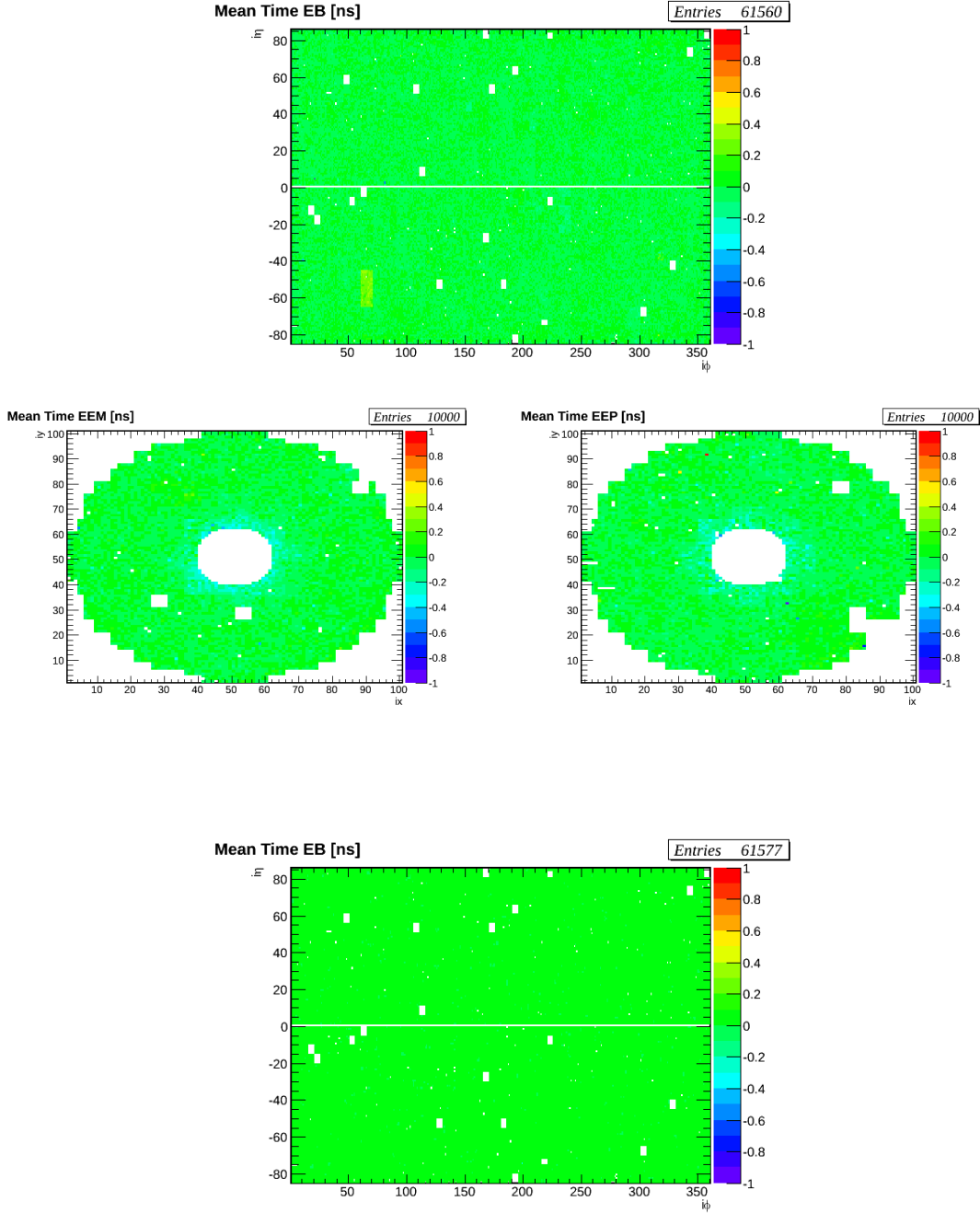
They could also be particles produced in the decay of a temporarily stopped particle inside the detector. To avoid the situation where this significantly large arrival time is caused by timing misreconstruction or mismeasurements, we have to calibrate the time measured by each of the PbWO₄ crystals in ECAL. Timing calibration also ensures the synchronization of all the component objects of a given event and assigns that event to the correct LHC proton-proton collision or bunch crossing. The presence of the “ T_{MAX} Phase”, the difference in pulse shape between each crystal, variation in time of flight by a few nanosecond (ns) and the different intrinsic delays among channels allow for timing calibration at two separate levels. At the level of the front end electronics (FE) consisting of 5×5 crystals, one is capable of performing an initial internal timing synchronization by adjusting in steps of 1.04 ns among these crystals. Determining these values of adjustments to be made is referred to as *Hardware Synchronization*. Offline, during event reconstruction, we can find and assign timing constants such that the measured crystal time is on average zero for true collision events arriving in a straight path from IP.

Offline Timing Calibration

The purpose of the offline calibration is to provide timing adjustments constants for each channel (crystal). These constants are derived from proton-proton collision data and the correct global phase shift in timing measurements caused by shifts in CMS clock relative to the LHC bunch crossings and de-synchronizations introduced during hardware interventions during detector repairs. The global timing shifts caused by CMS clock timing drifts can be about 1 ns while that caused by hardware intervention can be 3 to 5 ns. The calibration constants obtained for each crystal are of opposite sign to the average time measured from the reconstructed hits of each crystal. The constants kept in XML files format is loaded into the online configuration database with existing hardware settings. The calibration procedure starts with identifying timing shift reported in the CMS or ECAL detector running electronic (e-Log) book or the CMS or ECAL data acquisition monitoring (DQM) and followed by using reconstructed crystals hits or rechits from recently recorded or prompt data to measure the calibration constants for each channel. The validated calibration constants in an XML files are uploaded into the online configuration database for reprocessing of CMS full datasets used for

physics analysis. This process is performed throughout the entire LHC proton-proton collision period each year. At the end of each calibration process, the set of calibration constants developed for that period of time known as its *interval of validity* (IOV). The data used in measuring the timing constants is specified by run range of events. During the entire LHC run period in 2011, a total of 17 IOVs were developed while during 2012 LHC run, a total of 44 IOVs were produced. The raw dataset used in producing the calibration constants consists of mostly superclusters with crystal hits from Level-1 triggered events or loosely triggered photons, electrons and hadrons with large electromagnetic contributions. Datasets with such events are called *ElectronHad* or *PhotonHad*. Rechits from these events must pass a selection criteria like the event time (an average over its rechits) must be smaller than 5 ns, and belong to a basic cluster whose transverse energy is atleast 2 GeV. The signal amplitude must not be lower than 26(47) or 100 (in LHC 2012) ADC counts (corresponding to an energy of about 1(3) GeV) for rechits in EB(EE). The reconstructed rehit time must be within 5(7) ns window in EB(EE) respectively and to reduce the presence of anomalous crystal hits, the ratio of the sum of energies of the north, south, east and west neighboring crystals excluding a crystal with the highest energy to that of the energy of the highest energy crystal must be greater than 5% or equivalently $1 - E_4/E_1 < 0.95$ (the *swiss-cross* variable). Swiss-cross variable is very useful for rejecting events with anomalous crystal energy deposits. The selected rechits are used to make a timing distribution for each channel requiring each channel to have at least 10 rechits. After extracting the average time per crystal, the reverse of its value measured is the time calibration constants or inter-calibration coefficient used for correction. The variance represents the spread in measurement of the calibration constant. For channels with less than 10 valid rechits, the average time of all the other channels is assigned to them as their inter-calibration coefficient. We validate these constants obtained by performing a closure test by applying the reversed values of these constants to the same or different set of events and showing that the measured average time over rechits per channel is 0 ns to within the accuracy of the calibration method and small event migration in the event sample. The event migration effects are of the order of 10 ps. The figures 4.5 show a two dimensional distribution mean time for each crystal for all the 61,200 crystals in the EB and 1468 crystals in EE showing the mean time distribution prior (*top 3 plots*) to calibration and after (*bottom*

3 plots) the measured calibration constants have been applied. Further details of the full IOVs produced for the entire LHC Run 1 can be found here [47].



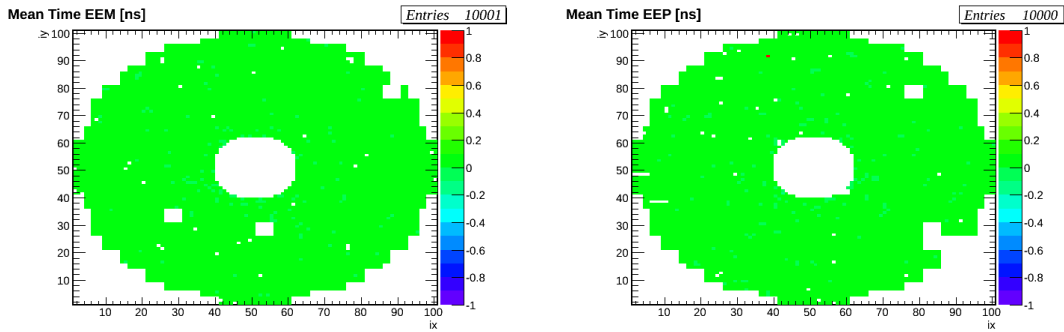


Figure 4.5: *Top 3*: Timing calibration maps showing the distribution of mean time for each channel/PbWO₄ crystal in EB (top) and EE (below: EE-(left), EE+(right)) before calibration. *Bottom 3*: Timing calibration maps showing the distribution of mean time for each channel/PbWO₄ crystal in EB (top) and EE (below: EE-(left), EE+(right)) after calibration. After calibration most crystals have an average time of zero(Green).

Hardware Timing Calibration

There are cases where a timing offset is introduced during hardware repairs at ECAL front end electronics. These timing offsets are not easily adjusted in event offline reconstruction. Hardware settings for readout electronics with timing offsets not properly aligned or calibrated can contribute to worsening of the timing resolution. The traditional method of correcting for this hardware timing offsets or latency during LHC stable proton beam collision has been to wait and collect enough data with the maladjusted hardware settings with timing offset, stop the entire CMS data taking process while LHC proton collisions are still ongoing, use the collected data to extract the hardware timing offsets, use these extracted timing offsets to adjust the hardware settings and continue with recording data with the CMS detector. These offsets are extracted from Data Quality Monitoring (DQM) and data certification hardware readout electronics performance histograms. Although this method is reliable, it encourages long and intermittent downtime as stopping the ECAL section of the CMS detector in order to adjust the settings of the hardware readout electronics causes lost in time which is equivalent to loss in data recorded during LHC stable proton beams. In order to improve on the total luminosity of data recorded by the CMS compared to data delivered by the LHC, CMS had to find a way of reducing these downtime. We developed a new approach to investigating and

adjusting the hardware latency settings for timing offsets at the readout electronics after a CMS or LHC machine intervention during technical stop or machine development. Our approach is to use laser data instead of proton-proton collision data. Laser data was already being used to adjust for crystal energy resolution due to loss of crystals transparency due to radiation. We use crystal time from laser data to measure hardware timing offset and use these timing offsets to provide new hardware settings prior to proton-proton collision. This adjustment is performed online *in-situ* through ECAL readout electronics condition database system. The full procedure including technical details for performing hardware latency adjustments online is well described in [48]. The ECAL laser system comprise of two lasers, a 440 nm wavelength (close to peak emission for PbWO₄ crystals) laser for monitoring crystal transparency lose and a 796 nm wavelength laser for monitoring readout electronics chain from APDs to ADCs. Both lasers have jitter of less than 4 ns every 24 hours run. To account for this jittery effect, the timing from the laser is averaged over 600 event pulses. The time for each crystal from laser is expected to be the same as the time from data and is represented as T_{MAX}^{APD} . The ECAL laser system is also equipped with a fast acquisition card called MATAcq. The time for each channel recorded using the Matacq is also averaged over 600 event pulse denoted as T_{Matacq} . The difference in $T_{MAX}^{APD} - T_{Matacq}$ between these two times averaged over a Clock and Control Unit (CCU) comprising of 25 crystals gives the time for each CCU denoted as $t_{CCU} = \langle T_{MAX}^{APD} - T_{Matacq} \rangle$ averaged over 25 crystals. In order to calculate the timing shift of 25 crystals belonging to the same Front End (FE) electronics, we monitor for any changes to this average value before (t_{CCU}^B) and after (t_{CCU}^A) hardware intervention. This difference $\Delta t_{CCU} = t_{CCU}^A - t_{CCU}^B$ after correcting for any global shift is the average time i.e. $\langle t_{CCU}^A - t_{CCU}^B \rangle$, shift and calibration constant for all the CCUs in an entire supermodule (SM) or front end detector (FED) (single readout unit from the data acquisition point of view). Any global timing shift of all the crystals in a given FED is due to the laser light distribution in-homogeneity or evolution of the laser pulse due to different optical fiber supply of laser light to each CCU. Each FED or SM has 1,700 PbWO₄ crystals. The plots in figure 4.6 show our current observation of monitoring for any shift in time within each CCU using laser. It shows the distribution of the CCU timing difference Δt_{CCU} with its root mean squared (RMS) value for each CCU before and after machine intervention. Considering the subtraction of the global

shift per FED also reduces the possibility of false timing shift in a given CCU. Using the average time subtraction method with laser data, we can measure each CCU timing shift to within 0.2 (0.5) ns EB (EE) in precision. This tool and procedure allow for adjusting the hardware timing settings during CMS data recording in Point5 at Cessy, France. However some validation studies for the reliance and efficiency of this tool is yet to be performed.

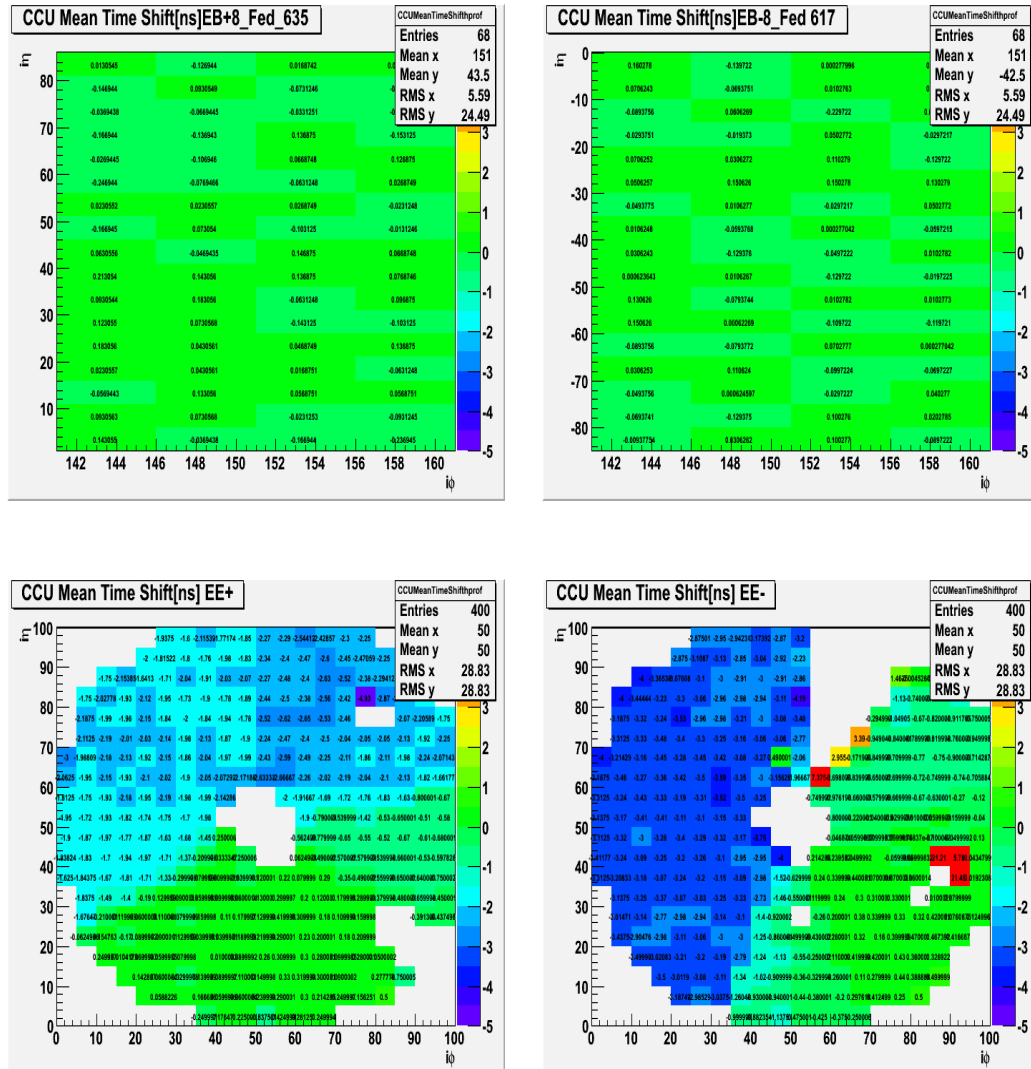


Figure 4.6: *Top*: Crystal mean time distribution for crystals in readout electronics EB \pm 8. Crystal time obtained from Laser data. *Bottom*: Crystal mean time distribution for crystals in readout electronics EE+ and EE-. The adjustment for global timing shift per FED due to difference in light source for each CCU has been shown to reduce the possibility of CCU showing false timing shift. The figures show the distributions of the Δt_{CCU} with corresponding RMS values after the global shift has been removed.

Timing Bias

The Ratio algorithm described in section 4.0.8 for extracting the amplitude and time of an event from the ten digitized samples in any given crystal or channel is assumed to perform efficiently for all energies of a given initial particle impinging on the crystal. However, during LHC Run 1 proton-proton collision, it has been observed that this is not the case, especially for very energetic particles. An inherent bias in the timing measurement is introduced for incoming electromagnetic particles with energy above the gain transition point by the MGPA. The energy in GeV deposited by an incoming particle on each crystal, i is given by the signal amplitude, A_i , in ADC counts and other correction and conversion factors is given by equation 4.5.

$$E_i = G \cdot S_i(t) \cdot C_i \cdot A_i \quad (4.5)$$

G is an ADC-to-GeV conversion factor equal to 0.039(0.063) in EB(EE). C_i is the inter-calibration coefficients accounting for individual channel response and $S_i(t)$ is the correction term (usually from laser data) accounting for radiation-induced channel response, it changes as a function of time. The Gain 1 transition point occur at 4096 ADC counts corresponding to 159.744 GeV in EB and 258.048 GeV in EE. The subsequent Gain 6 and 12 transitions are at energy values of TeV. The bias in timing introduced by these gain transitions cannot be calibrated at hardware, so we developed a method of applying these timing bias corrections at the CMS event reconstruction level. Using reconstructed hits with same selection as offline timing calibration, selected hits are also required to be part of a basic cluster (usually 9×9 or 25×25 matrix of crystals). These hits must have amplitude with channel noise consideration above 10 ADC counts. We reject hits with very large timing biased and large swiss-cross variable beyond our selection threshold (0.99). A distribution of the hit time against its amplitude is plotted

and then sliced in bins of amplitude. Each bin with at least 7 hits is fitted using a Gaussian function constrained within ± 7 ns. The average or mean and standard deviation or RMS of this distribution is extracted and plotted against its corresponding amplitude or energy bin content to give a distribution of mean against amplitude and standard deviation or resolution against amplitude. This procedure is performed for different *Modules* or pseudo-rapidity (η) ranges starting from $\eta = 0$ which is *Module 1* in barrel to $\eta = 3$ for high-eta in endcap. Figure 4.7 shows these distribution for different CMSSW releases; CMSSW44X where these bias corrections have not been applied during reconstruction and for CMSSW5XY where they have been applied. The dataset used for this reconstruction is the *DoubleElectron* and *Photon* dataset processed using CMSSW44X release during LHC RUN 1 and later reprocessed using CMSSW53X with the bias corrections applied. All CMSSW releases beyond CMSSW5XY now have these bias corrections applied.

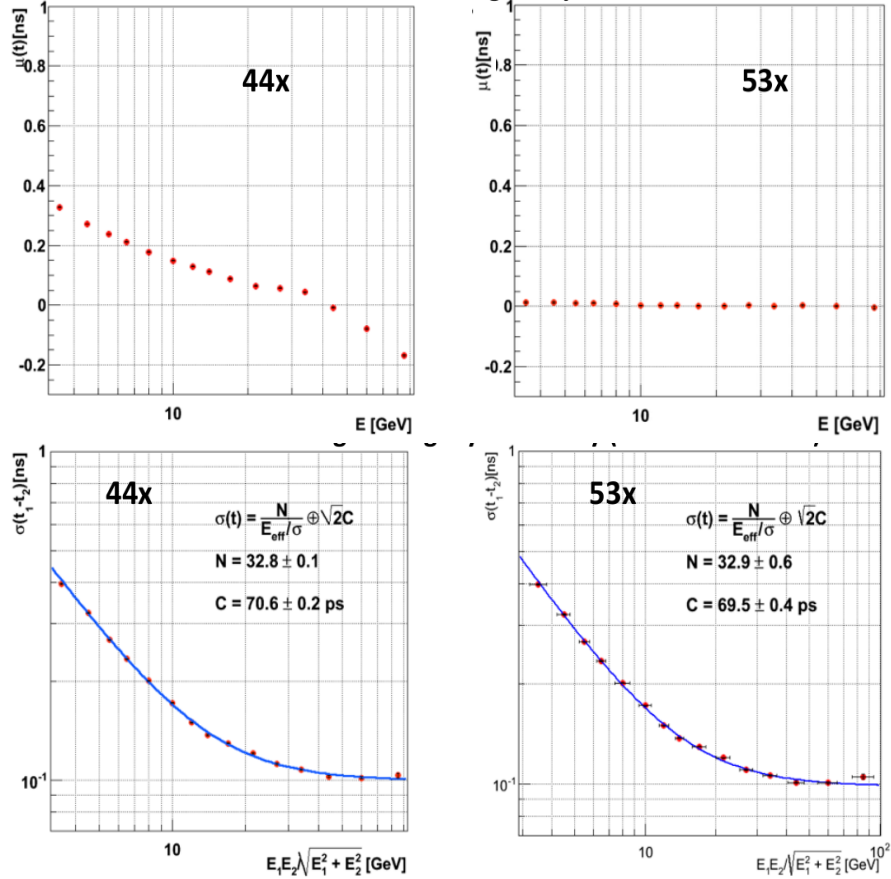


Figure 4.7: *Top Row*: Distribution of mean time as a function of crystal energy for EB prior (left) and after (right) timing bias corrections depending on amplitude have been applied. *Bottom Row*: Distribution of timing deviation (sigma) as a function of crystal energy for EB prior (left) and after (right) timing bias corrections depending on amplitude have been applied.

We have also performed detail studies to check for any η and run dependence on these timing bias. In figure 4.8, we show the distribution of the mean and standard deviation for different modules in barrel and sections in endcap. The timing resolution do not show any dependence on pseudo-rapidity (η), however minor dependence on event run number and different electronics or trigger towers have been observed. These small effects are yet to be understood and left for further investigation.

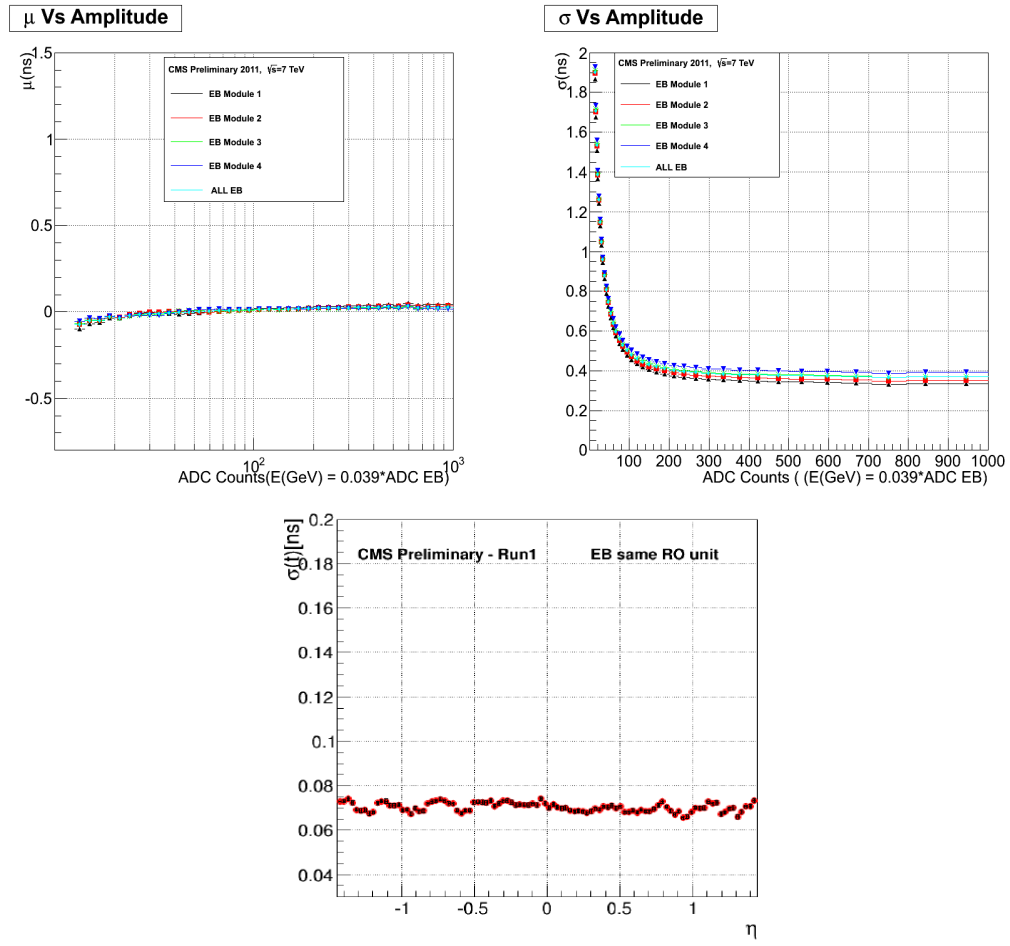


Figure 4.8: *Top*: Distribution of mean time as a function of amplitude (left) and Resolution as a function of amplitude (right) for different pseudo-rapidity regions in the barrel. *Bottom*: All modules in EB combined timing resolution as a function against η crystals in the same readout electronics in barrel (EB).

4.0.11 Electromagnetic Calorimeter Timing Performance

Timing calibration is performed to properly align the time of an incoming event which can be misaligned because of poor inter-calibration between different front end electronics, biased on timing due to timing dependence on energy, reduction in PbWO_4 crystal transparency due to radiation, hardware intervention during machine repairs and other effects. To measured the performance of time calibration procedure, we study the time measurements of ECAL crystals using events with double electrons produced from the decay of a Z boson i.e $Z \rightarrow e^-e^+$, which we understand most of its kinematics. The decay of a Z boson is well understood and effects due to poor event reconstruction or detector effects are well measured. The idea is to use the two electrons which in principle should have the equal arrival time and use their measured time difference to estimated the timing resolution performance of the PbWO_4 crystals in ECAL. In order to understand different source of poor timing measurements, we study the following different methods for measuring the time of the two electrons:

1. The time of two crystals in a single electron super cluster.
2. Neighboring crystals in a single electron supercluster sharing the same supercluster energy. This has the advantage of minimizing shower propagation effects.
3. Two crystals each from the different electron superclusters.
4. Two well reconstructed and energy corrected superclusters of each electron in the Z decay.

Here are additional sources of contributions to the electron time which we take into consideration:

1. The bending of the electron path due to the presence of the 3.8 T magnetic field of the CMS detector.

2. Displaced collisions because “partons” (quarks inside a proton) in the proton bunches did not collide at exactly the same collision point or nominal interaction point (IP).
3. The collision developed over the full duration and overlap of the proton bunches. This causes a spread in collision timing and account for about 183 ps in worsening of timing resolution measurements.

In the time calibration algorithm, the photon flight path is a straight path from IP to ECAL crystal. However, for electrons, being charged particles moving in the presence of a magnetic field, this is not the case. In addition to flight path, there are slight variations due to differences in the vertex position of electrons. Since it is possible to reconstruct the true vertex position of the electron, these small Time Of Flight (TOF) variations can be corrected. On the other hand this is not possible for photons as it is almost impossible to know its true vertex position. There are active investigations on how to reconstruct the true primary vertex of a photon using information of its arrival time in the ECAL, cluster position and energy. This study is motivated by Higgs decay. In summary, we use photons for timing calibration studies and electrons for studying the timing performance. Figure 4.9, shows the time resolution obtained using the time of the seed crystal (crystal with highest energy) in the electron supercluster and figure 4.10 shows using the time difference of both electrons adjusted for time of flight corrections. In the absence of timing uncertainties arising from individual proton collisions across the entire beam luminous region of nearly 5.5 cm(referred here as *proton collision time* of about $\sigma(t_{\text{colision}}) = \sigma(t_Z) = 183 \text{ ps}$) the measured ECAL timing resolution is 232 ps in EB and 384 ps in EE using Z events. Subtracting the proton beam collision time of 183 ps, we get a timing resolution of 142 ps for EB and 338 ps in EE. The selection requirements for the electrons include isolation using simple cluster shape selection requirements to differentiate them from hadrons, transverse energy bigger than 10 GeV. Both electrons must also have their invariant mass bounded from below (above) by a 60(150) GeV cut i.e. $60 \text{ GeV} < m_{\text{inv}}(e_1, e_2) < 150 \text{ GeV}$ to make a good Z boson candidate.

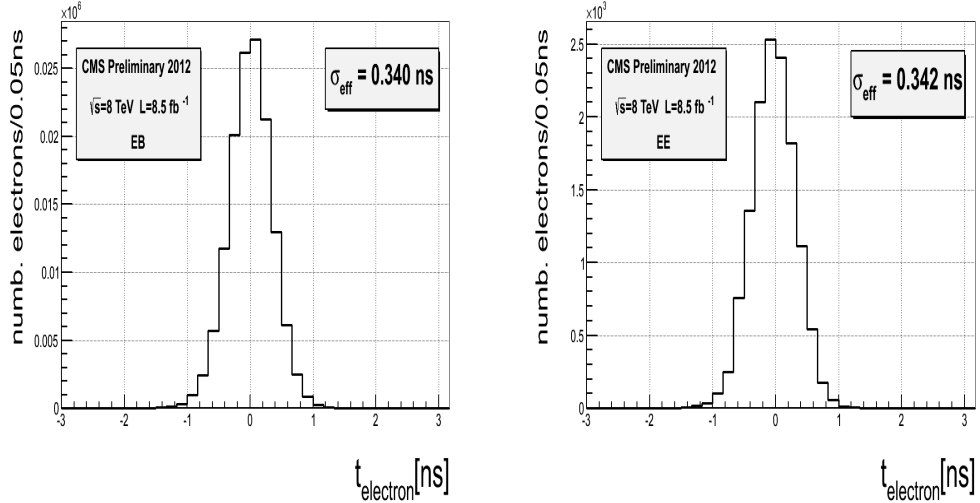


Figure 4.9: Ecal absolute time of a single reconstructed electron in $Z \rightarrow e^-e^+$ decay. The electron time is the seed (crystal with highest energy deposit) time of the electron in EB and EE

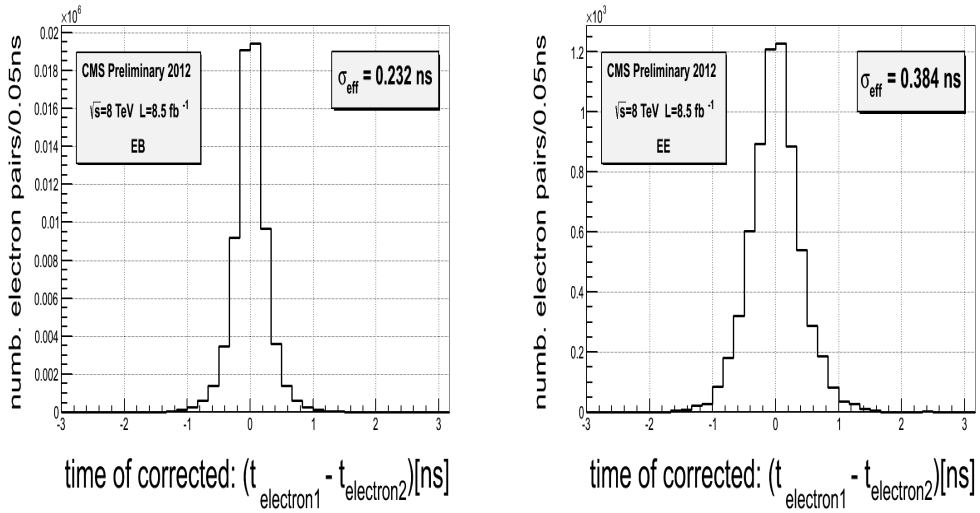


Figure 4.10: Ecal time difference between the two reconstructed electrons in $Z \rightarrow e^-e^+$ decay. The electron time is the seed (crystal with highest energy deposit) time with additional correction due to the time of flight of the electron in EB and EE

To compare the timing resolution obtain during test beam studies to that obtained at the end of LHC Run 1, a similar figure is made shown in figure 4.11 produced from the

$Z \rightarrow e^-e^+$ decay events with the time difference between the two electrons plotted as a function of the effective amplitude normalized to the noise in ECAL barrel for LHC Run 1. The noise term is consistent with results obtained during test beam while the constant term is about 150 ps, much larger than test beam results (70 ps). It has been shown that effects such as poor inter-calibration between two different front end electronics, run dependence and radiation might be the reason for this large constant term. Figure 4.11(left) show the time resolution against effective amplitude with the constant term $\bar{C} = 67$ ps if both crystals are from the same front end electronics while figure 4.11(right) is the time resolution against effective amplitude with $\bar{C} = 154$ ps if both crystals are from different readout unit or trigger tower. The noise term N is the same as test beam for both measurements. This indicates an effect due to different inter-calibrations for different electron shower initiation points in different trigger towers.

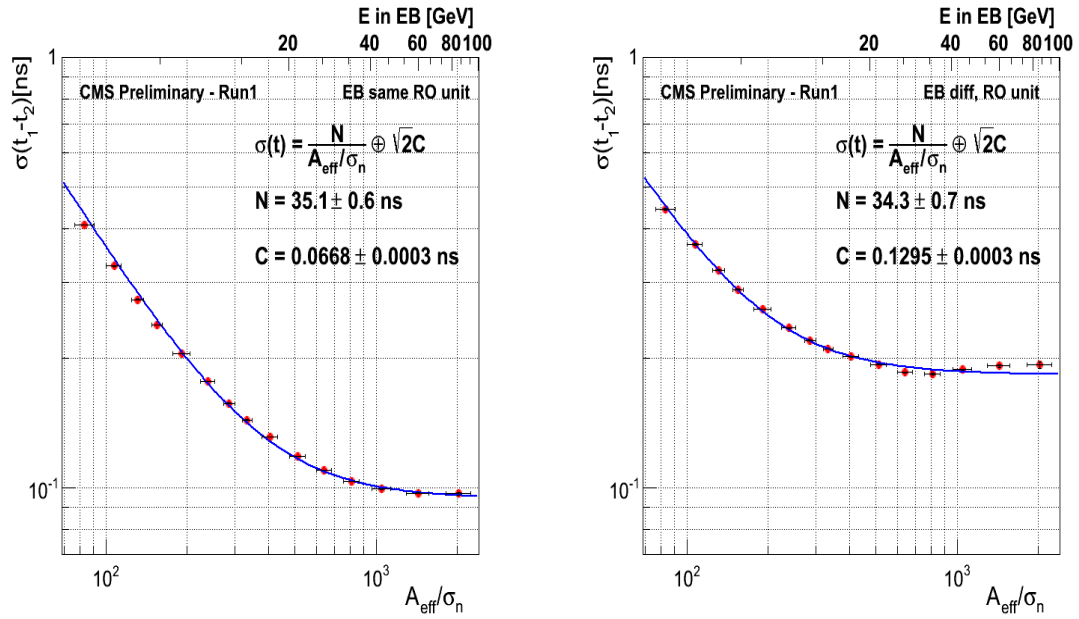


Figure 4.11: Resolution of time difference between : *Right*: Two most energetic crystals in the same readout unit, *Right*: Two most energetic crystals belonging to different readout units, as a function of effective amplitude($A_{eff} = A_1A_2/\sqrt{A_1^2 + A_2^2}$) normalized to noise in EB. Both crystals are from reconstructed electrons in $Z \rightarrow e^-e^+$ events.

Table 4.1 shows ECAL timing resolution for 2011 and 2012 LHC Run 1.

ECAL Timing Resolution		
2011		
$\sigma_{eff}(t_{seed})[\text{ps}]$	Absolute time	$\sigma_{eff}(t_{e1} - t_{e2})/\sqrt{2}[\text{ps}]$
EB	376	190
EE	356	282
2012		
$\sigma_{eff}(t_{seed})[\text{ps}]$	Absolute time	$\sigma_{eff}(t_{e1} - t_{e2})/\sqrt{2}[\text{ps}]$
EB	340	164
EE	342	272

Table 4.1: Table Comparing Timing Resolution performance of 2011 with 2012

Chapter 5

Physics Objects Reconstruction and Identification in CMS

5.1 Physics Objects Reconstruction

Reconstruction is the operation of constructing physics quantities from raw data collected in the experiment. It is a software process whose objective is data reduction to higher-level objects used for data analysis. An event observed by the CMS detector is reconstructed using information from the different sub-detectors. This information represents the raw data from the DAQ which is in a format called digitised hits or *digi*s. A local reconstruction is performed with the output from these reconstruction units called *RecHits*. The local reconstruction algorithm search for pixel or strips with a signal exceeding a threshold and use these as seeds for clusters. RecHits are typically position measurements (from times or clusters of strips or pixels) in tracking type detectors (Muon and Tracker systems) and energy deposits or hits from Calorimetry systems. For example in the Muon Cathode Strip Chambers (CSCs), local reconstruction provides position and time of arrival of muon hit from the distribution of charge induced on the cathode strips. For the case of the Electromagnetic Calorimeter (ECAL) and Hadronic Calorimeter (HCAL), local reconstruction identifies, the position, time of arrival and energy of localised electromagnetic and hadronic energy depositions respectively. The typical software package for local reconstruction is labeled as RecoLocalTracker as in the case of tracks indicating only local modules of the sub-detector have been used. Global

reconstruction takes these rechits as input to produce higher-level objects like charge particle tracks. This is where information from different modules in the same sub-detectors are combined. Clustering, tracking and fitting algorithms are used at this stage. For example, in ECAL and HCAL, global reconstruction provides a Calorimetric Tower (CaloTower) links matching clusters in ECAL and HCAL to produce a projective tower in the calorimetric system. These towers have a definite position in (η, ϕ) plane and are used as basis for Jet reconstruction as described later in the sub-sections. In the Tracker, global reconstruction uses tracker hits and track segments and use the seeds for Kalman fitter which builds trajectories with a χ^2 cut applied to reject hits unlikely to be associated with tracks. The typical software packaged is label RecoTracker again as in the case of full charge particle tracks. The final reconstruction combined reconstructed objects from individual sub-detectors to produce higher-level reconstructed objects suitable for high-level triggering or physics analysis. Further selection requirements may be further applied until the final physics objects such as electron, photon or jet belonging to the event is fully reconstructed.

5.1.1 Supercluster Reconstruction

The basis of all object reconstruction is the supercluster or basic cluster. Electromagnetic showers of photons and electrons are deposited in several crystals. Usually about 94% (97%) of the incident energy is deposited in a 3×3 (5×5) matrix crystals in the (η, ϕ) plane. The presence of 3.8 T magnetic field, material in front of the calorimeter causes bremsstrahlung electrons and converted photons to deposit their energy in calorimeter in the form of small clusters spread in ϕ . This energy is recovered using clustering algorithms where by starting with a seed crystal containing the maximum of energy, superclusters (clusters of cluster) are built within a narrow window in η by summing the crystal energy along the ϕ which is the direction of energy spread due to the magnetic field. Figure 5.1 shows a simple picture how these super clusters are built.

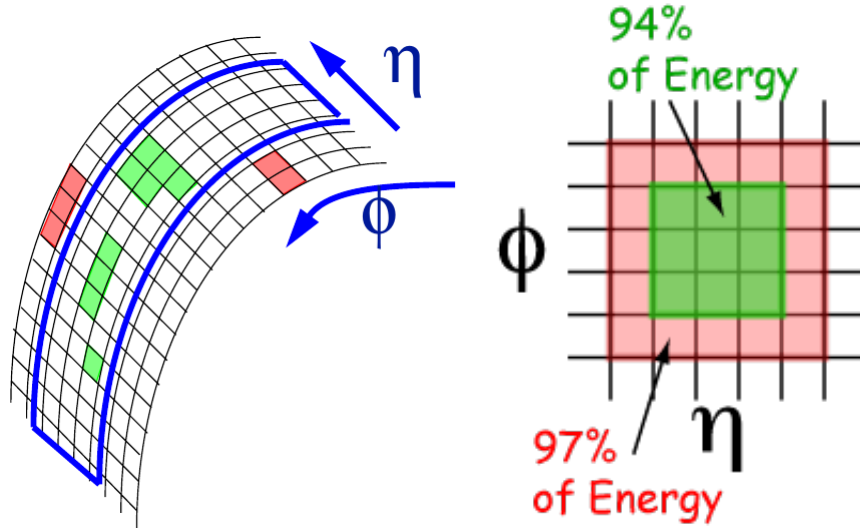


Figure 5.1: Superclustering algorithm in ECAL for both hybrid (EB) and island (EE) clustering algorithms.

There are two major clustering algorithms used:

- **Hybrid Superclusters:** This algorithm is used to make super-clusters in the barrel (EB). It takes advantage of the $\eta - \phi$ geometry of barrel crystals by taking a fixed 3 or 5 crystals in η and dynamically search and sum separate crystals energy along ϕ . The Hybrid algorithm takes advantage of our knowledge of the lateral shower shape along the η direction. The supercluster is made of basic clusters. The figure 5.2 shows an example of how the hybrid clustering algorithm performs clustering.

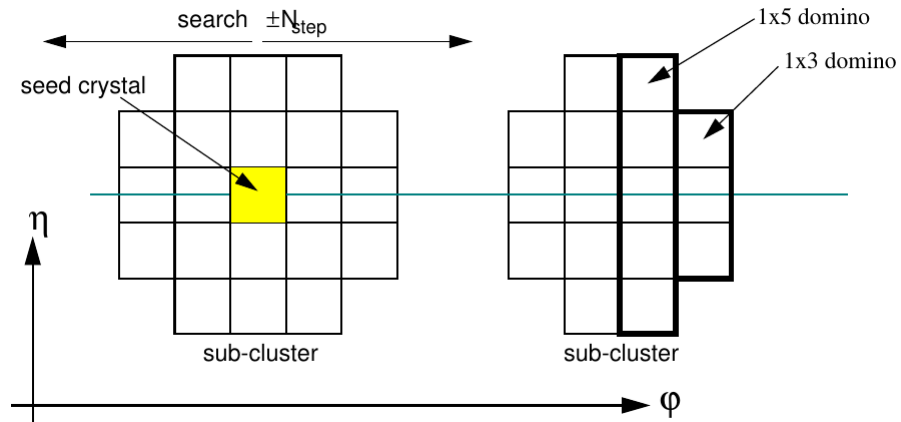


Figure 5.2: Superclustering in ECAL for hybrid clustering algorithm in barrel.

- **Island Basic cluster or Superclusters:** After Local reconstruction leading to the production of *EcalRecHits*, the island algorithm is applied in both barrel and endcap (EE) to produce superclusters. This algorithm begins by finding the seed crystal with a local energy maximum above a certain threshold. from the seed position, adjacent crystals are examined starting first along ϕ and then in η adding crystal energy to cluster until a crystal belonging to another cluster or crystal that has no readout is reached. For each crystal to be added to the cluster, the crystal must contain a rechit with positive energy, the crystal has not been assigned to another cluster and the previous crystal added in the same direction has higher energy. These non-overlapping clusters are then made into superclusters. A search is performed for the most energetic cluster and then collect all the other narrow window clusters in η and wide window in ϕ . The figure in 5.3 provides a pictorial view of how the island algorithm works.

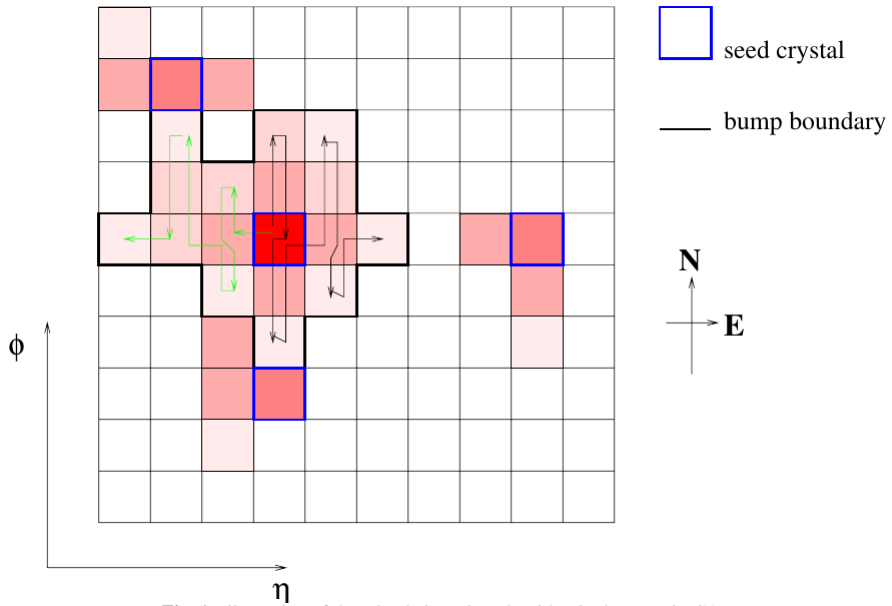


Figure 5.3: Superclustering in ECAL for Island clustering algorithm in barrel.

5.1.2 Vertex and Track Reconstruction

The reconstruction of track candidates of a charge objects such as an electron begins by selecting an initial parameter which a pair or triplet of hits constraint by the interaction region or a given beam spot in the pixel detector. This if followed by the search of other pairs of hits in pairs of tracker layers as well as hit pairs in the strips or strips an pixels to allow for reconstruction of vertices beyond the pixel volume. To prevent the combination factor and reduce fake rates when using the Combinatorial Track Finder (CTF), hits are selected in a small restricted region in ϕ compatible with a super-cluster in the ECAL. This seeding strategy is known is *tracker-driven*. Another powerful approach is to start with the ECAL super-cluster and match the seed super-cluster hits back towards hit in the tracker particular the pixel. It is term *ECAL-driven* seeding and this super-cluster-driven pixel seed finding presents advantage for comparable reconstruction efficiency and increasing the purity by reducing the presence of fake tracks in the sample of candidate tracks. This is particularly useful for electron reconstruction and is used by the Higher Level Trigger (HLT) for tagging primary electron-like objects.

In selecting the seed cluster, the cluster which initiates the bremsstrahlung recovery procedure, this seed is required to have a minimum Transverse Energy (E_T) of 1 GeV is $E_T > 1$ GeV. This requirement allows the reconstruction of electron super-cluster for with low Transverse Momentum (p_T). In a study using back-to-back e^+e^- events, a supercluster reconstruction efficiency of about 93% is achieved for electron $p_T^e = 10$ GeV/c when $E_T^{seed} > 1$ GeV. Using this seed cluster, the hits in the pixel layer are predicted by the propagation of an energy weighted mean position of the super-cluster backward through the magnetic field under the charge hypothesis(positive or negatively charged particle) towards the pixel detectors. A first compatible hit is looked for in the inner most (barrel) of the pixel detector within a loose $\Delta\phi$ window adapted to the uncertainty of ϕ measurement of the super-cluster (ϕ_{SC}) and loose Δz interval adapted to the spread of the interaction vertices. In case no hit is found in the innermost pixel layer, the first hit is looked for in the next-to-innermost layer. Once a compatible hit is found, a new estimate of the z_0 on the z coordinate of the primary track vertex is calculated by combining the pixel hit found and the information from the calorimeters in the RZ plane. Using this predicted trajectory, we propagate once more to look for the second pixel hit in the next pixel layer(s).

Starting from this seed (pair hits), a trajectory is created. This trajectory creating begins by first searching for the next silicon layer hits, then extrapolation is performed using a model based on the non-gaussian nature of energy losses by Bethe and Heitler, then Gaussian Sum Filter (GSF) algorithm is used to perform a fit on the track. This procedure is repeated until the last trackers layers unless no hit is found on the subsequent layers. If many hits are found on a compatible layer, many candidate tracks are built in parallel and using the χ^2 from the GSF fit, the best two GSF track candidates with the smallest χ^2 are selected and kept. A minimum of five hits is required to create a track. The difference between electrons and photons at this stage is that photons because they are neutral have no pixel hits and as a result have no reconstructed tracks. Thus, from the ECAL driven track reconstruction, super-clusters with no pixel matched seeds fall into the photon candidate sample collection. However, 50% of the time photons due to the tracker material will convert into e^+e^- conversion pairs. These are known as *converted photons*. These converted photons are usually low p_T photons and don't always travel to the ECAL but those that do and if happen to arrive late can be candidates for clear signal of physics beyond the SM. Because electrons have a GSF tracks , they are normally referred to as GSF electrons. Using the selected GSF tracks, important particle kinematic information such as the vertex pseudo-rapidity (η), the track p_T and the vertex ϕ coordinate are well measured with good resolution.

The primary interaction vertex in an event is reconstructed from a collection of tracks. A group of tracks in clusters based on the z coordinate position of their track with respect to the point of closest approach to the beamline. The track clusters, as previously mentioned are fitted with an adaptive vertex fitter and the tracks are assigned weights between 0 and 1 based on their closeness in proximity to the common vertex. This ensures a dependence on the primary vertex resolution to the number of tracks used in the fitting and p_T . This primary vertex resolution dependence on the number of tracks is studied using tracks in an event with just one vertex while for p_T , the resolution is studied for a number of tracks with different average p_T of tracks in the vertex. It is important to recall that tracks can only be reconstructed up to $|\eta| < 2.5$ which defines the tracker volume, beyond which these objects are assumed to have no tracks.

5.1.3 Photon or Electron Identification

Electron and photon identification depends of the ability to reject minimum biased events, underlying events or Pile Up (PU) produced from multiple proton-proton interactions, electrons embedded in hadronic showers or Jets and anomalous events. Pre-selections are applied at the level of track seeding and clusters so as to reject tracks from underlying or low energy proton-proton collision events called Pile Up (PU). Based on kinematic and nature of electromagnetic showers in the ECAL, some variables have been developed and their performance studied for optimal identification and isolation of electrons and photons. This is in compatibility with the fact that the two electron reconstruction algorithms compliment each other in specific p_T range. The tracker seed driven algorithm is more suitable for low p_T electrons as well as better performance for electrons inside jets while ECAL seed driven algorithm which selects seeding clusters with transverse energy $E_T > 1 \text{ GeV}$ is optimised for isolated electrons $p_T > 10 \text{ GeV}/c$ up to p_T relevant for the mass of Z or W bosons.

The goal of the ECAL is to obtain the best estimate of energy deposited by an electron or photon in the ECAL, $E_{e/\gamma}$. This from the detector point of view, the energy deposit is given as:

$$E_{e/\gamma} = F_{e/\gamma} \cdot [G \cdot \sum_i S_i(t) \cdot C_i \cdot A_i] \quad (5.1)$$

where A_i is the signal amplitude in ADC counts, C_i is the inter-calibration coefficient, $S_i(t)$ is the time-dependent corrections for response variable usually obtain from laser, G is the global scale calibration allowing one to move form energy in ADC counts to GeV and $F_{e/\gamma}$ is the particle energy corrections for geometric, clustering and other effects. The sum is over all the crystals belonging to the photon or electron super-cluster. In order to measure and reconstruct the true energy of the detected particle, energy corrections depending on η such as $F_{e/\gamma}$ are applied at the level of super-cluster reconstruction to account for detector effects hence better identification of particles, in this case electrons and photons. Figure 5.4 shows energy scale and resolution obtained when these energy corrections are applied compared with when no corrections are applied. Figure 5.5, shows the scenario for applying these corrections at the level of super-cluster reconstruction which at this stage are only electromagnetic objects.

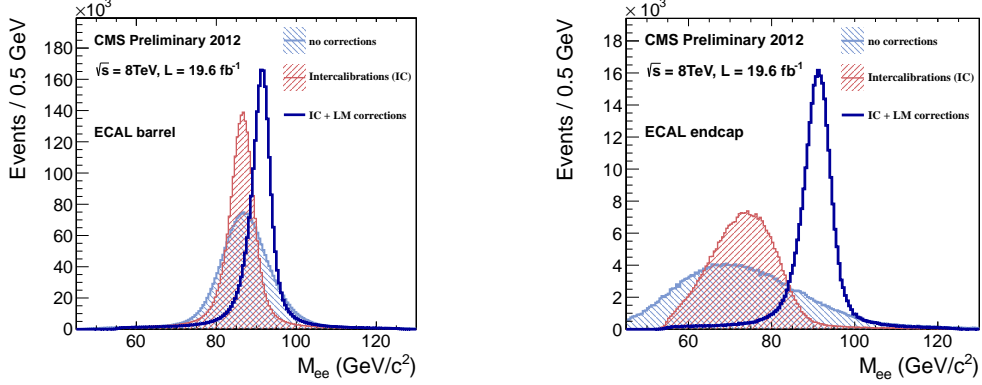


Figure 5.4: $Z \rightarrow e^+e^-$ mass plot showing resolution and energy scale that is obtained from applying energy scale corrections to account for intrinsic spread in crystal and photo-detector response and time-dependent corrections to compensate for channel response loss for EB (right) and EE (left)

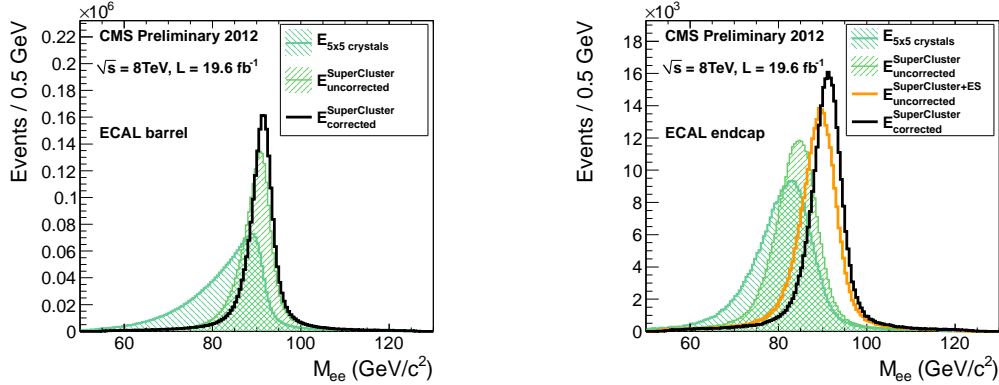


Figure 5.5: Super-clusters showing resolution and energy scale that is obtained from applying energy scale corrections for EB (right) and EE (left)

With these electron or photon candidates, further selections using variables constructed from information on the spread of the electromagnetic shower in η and ϕ , the ratio of the energy deposited in ECAL and HCAL, the track p_T and ECAL E_T to further identify photons and electrons. Pre-electron candidates based on cut elections such as minimum transverse energy, $E_T > 4$ GeV, η and ϕ geometrical matching; $\Delta Eta < 0.02$, $\Delta\phi < 0.1$ and a cut on Ratio of hadronic to electromagnetic energy cluster: $H/E < 0.2$ is enough to suit physics analysis, however, additional elections and identification criteria are added depending on the purpose of the particular analysis to fully defined an electron or photon. These identifications and isolation criteria can also be categorised

in terms of flavours as being very loose (VL), loose (L), medium (M) and tight (T). The typical variables used for electron and photon identification are defined as follows:

- Ratio of energy of HCAL behind super cluster to super cluster energy: H/E
- Energy momentum matching variables between energy of the super cluster or of the super cluster seed and electron track measured momentum at the vertex or at the calorimeter: E/p_{in} , E_{seed}/p_{in} , E_{seed}/p_{out}
- Geometrical matching between the electron track parameters at the vertex extrapolated to the super cluster and the measured super cluster position: $\Delta\eta_{in}$, $\Delta\phi_{in}$.
- Calorimeter shower shape variables: the width of the ECAL cluster along the η direction computed for all the crystals in the 5×5 block of crystals centered on the highest energy crystal of the seed cluster, $\sigma_{in,\eta}$ and the ratios of the energy sums over 3×3 and 5×5 matrices centered on the highest energy crystal of the seed cluster: $R_9 = E_{3 \times 3}/E_{5 \times 5}$ or $R_9 = \sum E_9 / \sum E_{Supercluster}$. This R_9 variable makes a good separation between unconverted photons (energy not spread in tracker) and converted photons (energy spread by B-field before reaching ECAL).
- Bremsstrahlung fraction: $(track\ momentum\ at\ vertex - track\ momentum\ at\ ECAL) / track\ momentum\ at\ vertex$.
- $1/E(\text{Super cluster}) - 1/p(\text{track at vertex})$

Due to the very high photon conversion rate s as a result of the tracker material in front of the ECAL cuts like:

- Calorimeter shower shape: R_9
- Impact parameter: $d0$, minimum separation of the electron track computed with respect to the reconstruction vertex.
- Missing Hits: Number of cross layers without a compatible hits in the back-propagation of the track to the beam-line.

Isolation variables in addition to the identification variables are used to improve on the performance of identification. Below are the following isolation variables as defined and used by the CMS:

Electron Photon Isolation

- Tracker Isolation: sum of p_T of tracks with $p_T > 0.7 \text{ GeV}/c$ and maximum distance to the vertex of 0.2 cm in a cone of 0.3 with an inner veto cone of 0.04.
- ECAL Isolation: sum of energy of ECAL RecHits with a Jurassic footprint removal (Jurassic width of about 1.5 crystals) in a cone of 0.4 with veto cone of 3 crystals. A RecHit noise cut of 0.08 GeV in energy (E) in barrel and 0.1 GeV in transverse energy (E_T) in the endcap is applied.
- HCAL Isolation: sum of HCAL Calorimeter Towers in a 0.4 cone with a 0.15 veto cone.

In general the major difference between an electron and a photon as identified by the CMS detector is that electrons which have no pixel strip hits are automatically classified as photon candidates and further isolation and shower shape variables are used to arrive at the ultimate photon as required by a given analysis. Table ?? shows the Simple Cut-based selection criteria variables and cut thresholds used to identify electrons and photons in the CMS detector.

Particle Flow Algorithm

An alternative criteria for reconstructing and identifying physics objects in the CMS detector which is now widely acceptable is the *particle flow* (PF) algorithm.

The particle flow algorithm takes into consideration information from every sub-detectors like the tracker, ECAL, HCAL and muon section before identifying a particular physics objects. The goal of this algorithm is to reconstruct higher level physics objects like Jets, missing transverse energy (MET), and the identification of tau (τ) and b-jets by making use of the content of these objects in terms of more fundamental objects like electrons and photons or super clusters and tracks. The algorithm constitutes of steps like calorimeter clustering, tracking and extrapolation to calorimeters, muon identification, electron pre-identification, linking of topological elements and finally particle

identification and reconstruction. The result is a list of reconstructed particles consisting of photon, charge hadron, neutral hadron, muon and electron. From this list high level objects such as jets, MET and taus can be reconstructed. In the case of electrons reconstructed using the PF algorithm, tracks, electron energy seeds, 4-momentum, super cluster energy calibration, Bremsstrahlung tracks are used as base objects to reconstruct the entire electron. The PF is very useful in MET reconstruction where information about all the particles making up a single event is necessary to calculate MET.

Simple Cut Based Electron Photon Identification		
ID Variable	Electron	Photon
H/E	0.05(EB), 0.10(EE)	0.05
$ \Delta\eta_{in} $	0.005(EB), 0.007(EE)	0.015(EB)
$ \Delta\phi_{in} $	0.09(EB), 0.09(EE)	N/A
$\sigma_{i\eta i\eta}$	0.01(EB), 0.03(EE)	0.011(EB), 0.03(EE)
Pixel Veto	No	Yes
$ d0 (vertex)$	0.02(EB), 0.02(EE)	Veto
$ dZ (vertex)$	0.1(EB), 0.1(EE)	0.02 (cm)(Veto)
$ 1/E - 1/p $	0.05(EB), 0.05(EE)	N/A
PF isolation / p_T (cone dR=0.3)	0.15(EB),0.10(EE)	N/A
ECAL Isolation	same	$4.2 + 0.006 * E_T^\gamma + 0.183 * \rho(\text{EB})$
HCAL Isolation	same	$2.2 + 0.0025 * E_T^\gamma + 0.062 * \rho$
TRACK Isolation	same	$2.0 + 0.001 * E_T^\gamma + 0.0167 * \rho$
Rho corrected PF photon isolation	N/A	$1.3 + 0.005 * p_T^\gamma(\text{EB})$

Table 5.1: Simple Cut-Based criteria for High energy electron and photon identification in CMS

5.1.4 Muon Reconstruction

The are three different types of muons reconstructed using the muon system detection all making up one huge collection of muons. They are Stand-alone, Global and Tracker Muons. Reconstructed hit positions within each DT and CSC are matched to form “segments” which are then collected and matched to generate seeds used as starting point for actual track fit of DT, CSC, and RPC hits. The resulting product of the fit in the muon spectrometer is a “stand-alone muon”. “Global muons are formed when these stand-alone muon tracks and matched to tracker tracks in the tracker while ”tracker muons“ are muon objects reconstructed starting form silicon tracker tracks compatible with segments in the muon chambers. Using muon isolation variables defined using the calorimeter and tracker tracks, a collection of muon objects is identified in CMS. Thus is summary, stand-alone muons contain only hit position information from the muon chambers, global muons contain this information in addition to tracker information while Tracker muons are muons reconstructed starting with information from the inner tracker which is matched with calorimeter and muon chamber information. Using the beam spot as a constraint ensures that muons produced from proton-proton collision are distinguished from those produce from cosmic rays known as *cosmic muons* or from beam splash/gas 150 m upstream proton beam dump known as *beam Halos*. The 2 T **B**-field with a multi-stage flux-return yoke shields the muon detectors from hadrons ensuring that the measured particles can be identified as minimum ionizing muons. The barrel muon detector consists of 4 stations forming concentric cylinders $|\eta| < 1.2$ around the beam line while the endcaps system consists of 468 cathode strip chambers (CSC) arranged in groups as 72 ME1/1, 72 ME1/2, 72 ME1/3, 36 ME2/1, 72 ME2/2, 36 ME3/1, 72 ME3/2and 36 ME4/1 and the 72 ME4/2. A muon in pseudo-rapidity range of $1.2 < |\eta| < 2.4$ crosses a total of 4 CSCs. Muons in the encaps-barrel overlap region; $0.9 < |\eta| < 1.2$ are detected by both the barrel drift tubes (DT) and endcaps CSCs while in bother barrel and endcaps RPSc are used for triggering. RPCs are capable of tagging the time of an ionizing event in a much shorter time than the 25 ns between 2 consecutive LHC Bunch Crossings as a result triggering based on RPC can be used to unambiguously identify the relevant Bunch Crossing to which a muon track is associated even in the presence of high rate and background expected in the LHC.

Cosmic and Halo Muons

Muons produced centrally or from proton-proton collision are reconstructed a bit different from other muons. Halo muons originating from machine-induced particles travelling along the beam line and cosmic muons originating from cosmic rays require global information in order to distinguish them from centrally produced muons. Both cosmic and halo muons are considered to be background muons in most physics analysis. The stand-alone muon reconstruction software suited from reconstructed muons from proton-proton collision assumes these muons to be moving radially outward in seen in figure 3.11 while cosmic muons originate from the outside of the CMS detector and can traverse only a small part of a detector depending on its energy and direction. Figure 5.6 show an illustration of different trajectories for the different types of muons.

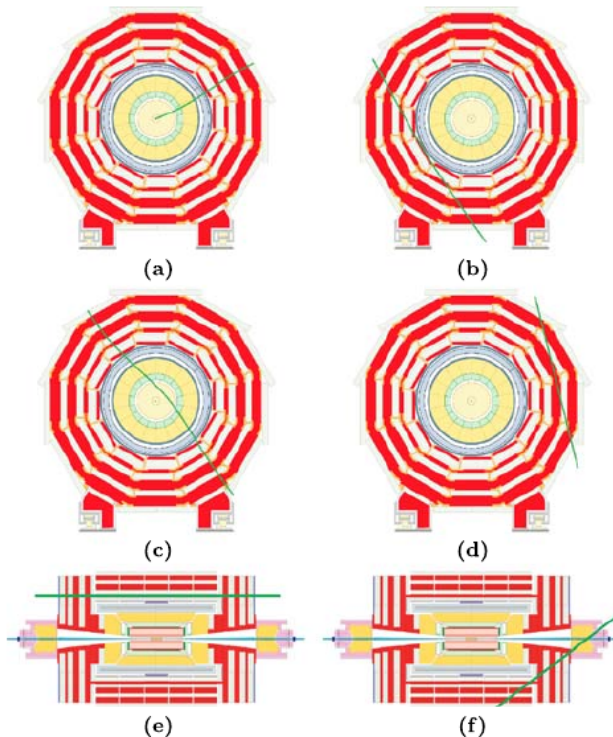


Figure 5.6: Illustration of the differences between proton-proton collision muons, cosmic and halo muons. (a) Muons from collision propagating from the center and moving outwards in a well defined pattern, (b) Cosmic muons penetrating the detector and leaving signals in opposite hemispheres of the muon system, (c) Cosmic muons leaving signals in the tracker and opposite hemispheres, (d) cosmic muons entering and leaving the detector without passing through the muon detector layers, (e) beam halo muons penetrating the detector and leaving signals in the endcaps and (f) Cosmic muons entering the detector through the endcap and leaving through the barrel and which can happen in a vice-versa manner.

A new stand-alone and global muon reconstruction software with the assumption that muons originate from outside the CMS detector and according to the properties of cosmic and halo muons has been optimised to reconstruct and identify both cosmic and halo muons which are used studies involving calibration and aligning the muon detectors.

5.1.5 Jet Reconstruction

Jets are experimental signatures of quarks and gluons produced in high energetic processes such as hard partons scattering in proton-proton collisions or gluon radiation processes. CMS reconstructs four types of jets which each combine individual contributions from sub-detectors to form inputs to a jet clustering algorithm. The four types of jets include Calorimeter jets, Jet-Plus-Track (JPT) jets, Particle-Flow (PF) jets and track jets. The clustering algorithm is the Anti- k_T clustering algorithm with a size parameter of $R = 0.5$. Calorimeter jets are reconstructed using energy deposits in the combine ECAL and HCAL calorimeter cells called calorimeter towers. A calorimeter tower is a single or group of HCAL cells with their geometrically corresponding ECAL crystals. In order to suppress both noise and contributions from event pile-up (additional proton collisions within the same bunch crossing), thresholds are applied to both the individual cells when building the calorimeter towers as well as a transverse energy (E_T) cut on the calorimeter tower energy. Typical $E_T^{towers} > 0.3 - 0.7$ GeV is often used. Of particular importance to our analysis is the Particle Flow jets (PFJ). PFJ are reconstructed using the PF algorithm. The PF algorithm uses as input a list of reconstructed particles which include charge hadrons from tracks in central tracker, photons and neutral hadrons reconstructed from energy clusters in the HCAL and ECAL,

neutral particles as clusters separated from extrapolated position of tracks in calorimeters and electrons from tracks matched to clusters in the calorimeters. The PF algorithm exploits the high granularity in ECAL to precisely measure charge hadrons and photons inside jets, which makes up a larger portion of the jet energy. The quality of the jet is determined by variables making up the "Jet ID". For example, a high quality jet is required to have an electromagnetic energy fraction (EMF), $EMF > 0.01$, within the ECAL fiducial region $|\eta| < 2.6$; the number of calorimeter cells containing more than 90% of jet energy must be $n_{jet}^{90} > 1$; and the fraction of jet energy in the hottest Hybrid Photo Detector (HPD) unit of HCAL readout within a jet must be $f_{HPD} > 0.98$; the charge hadron fraction $CHF > 0.0$ if within $|\eta| < 2.4$, neutral hadron fraction $NHF < 1.0$, charge electromagnetic fraction $CEF < 1.0$, and neutral electromagnetic fraction $NEF < 1.0$. These requirements are used to remove fake jets arising from spurious energy deposition in a sub-detectors. Because the measured jet energy is usually different (usually unwanted energy) from the true corresponding particle jet energy due to miss-reconstruction, non-linear response of the calorimeters, electronic noise and additional energy contributions from PU, jet energy corrections during jet energy calibration (JEC) are applied to correct for this energy miss-match between the reconstructed measured jet energy and the true energy of the jet particle. This JEC to determine the jet absolute response is a source of systematic uncertainties in a given physics analysis.

5.1.6 Missing Transverse Energy Reconstruction

A typical collider detector can only be nearly hermetic despite its nearly 4π solid angle coverage as there is always room for passage of the colliding beams. As a result the use of the total energy balance constraint is not very useful since low p_T energetic interaction products moving in the forward direction can always escape detection. Thus, although these forward moving particles can carry significant longitudinal momentum (momentum along the direction of the beams), their transverse momentum (momentum transverse to the direction of the beam), p_T is always smaller than their total momentum. In the case of the CMS detector which has pseudo-rapidity $|\eta| < 5.0$, therefore only particles with $|\eta| > 5.0$ can escape detection, as we can easily find that the p_T of any given particle in CMS detector given as $p_T = E/\cosh \eta < E/\cos(5) < 0.013 \times E$.

Thus even if the particle carried the whole 7 TeV energy of a single proton beam, its $p_T < 100 \text{ GeV}/c$. Partons inside a protons which collide to produced moving particles typically have only a fraction of the energy of the colliding proton. Each fraction is determine by parton distribution function (PDF). PDF are rapidly falling functions, thus a typical momentum for forward moving particles in hard collisions on interests for physics goals of an experiment is significantly less than the full beam energy. As a result, the transverse momentum carried away by particles beyond the acceptance of a calorimeter is very small, thus the detector allows for a precise test of 2-D momentum conservation of the plane perpendicular to the direction of the beams. In the case of the CMS detector, this plane in the $x - y$ plane. Thus the measurement in the calorimeter of a significant imbalance in the transverse momentum will indicate the production of a weakly interacting particle in the collision. Among SM particles, such an imbalance would indicate the presence of a neutrino or a muon which deposits a very small amount of energy in the calorimeters. However, the momentum of the muon can very precisely be measured using information from the tracker and muon chambers, and the calorimeter based missing transverse momentum can be measured and corrected for the muon's presence. Thus only the neutrino would truly escape detection, and its presence would be inferred from the remaining imbalance in the total transverse momentum as measured in the calorimeter and muon detectors. Other extensions of the SM, also predict the existence of other weakly interacting stable and quasi-stable particles, thus if an excess of events with a significant amount of transverse momentum imbalance is observed after accounting for all the SM processes, it would constitute a strong evidence for new physics beyond the SM. In the case of the minimal GMSB, the gravitino (\tilde{G}) would be the new physical particle. Thus the total transverse momentum imbalance or *missing transverse momentum* is an important variable to use in the search of new physics particles. On the other hand, poorly reconstructed objects, detector malfunctions, electronic noise and miss-measured transverse momentum can all lead to missing transverse energy thus mimicking the signal for new physics. Thus careful studies of the performance of the missing transverse energy variable in identifying neutrinos in the SM with high efficiency and accuracy is needed in order to depend on the use of it. The missing transverse momentum represented as the Missing transverse energy or MET (E_T^{miss}) which is itself a scalar quantity defining the magnitude of the missing

transverse momentum which has both direction ($\phi_{E_T^{\text{miss}}}$) and magnitude E_T^{miss} . The missing transverse energy is defined as the magnitude of the negative transverse vector sum over all energy deposits in uncorrected, projective Calorimeter Towers produced in a given event:

$$E_T^{\text{miss}} = \left| - \sum_n (E_n \sin \theta_n \cos \theta_n \hat{\mathbf{i}} + E_n \sin \theta_n \sin \theta_n \hat{\mathbf{j}}) \right| = |\cancel{E}_T^x \hat{\mathbf{i}} + \cancel{E}_T^y \hat{\mathbf{j}}| \quad (5.2)$$

Where n is the sum over all calorimeter input objects including energy deposits in towers, reconstructed hits or generator -level particle energies. The E_T^{miss} values in physics processes of interest include processes with small E_T^{miss} such as the decay of W bosons and top in the SM to large E_T^{miss} as in the decay of SUSY particles. Thus in order to use small E_T^{miss} for searches, SM processes like QCD, JEC and low energy resolution must be well understood while to use large E_T^{miss} for searches, machine induced background processes and poor event reconstruction which processes with sources of large E_T^{miss} must equally be well understood.

5.2 Anomalous Signals

Neutrons and charged hadrons such as protons may by pass the PbWO₄ without scintillating and striking and thus directly ionizing the silicon of the APDs to produce anomalous signals. These kind of events produced large isolated energy deposits thus are referred to as "punch through" events or "spikes". Because of the lack of scintillation, they appear much earlier (negative) in Ecal time and often populate the earlier time of the rechit time distribution. Their energy deposit ranges from a few GeV to ECAL saturation energy of ≈ 1.7 TeV. Since they do not electromagnetically shower in PbWO₄, their electromagnetic energy shower shape is very isolated, meaning only one or two crystals may make up their energy cluster. Spikes may also have positive time and thus appear late or delayed in their arrival at ECAL which is seen in the tails of the rechit time distribution. Their late arrival time is due to the slow propagation of neutrons through the CMS detector. A lot of test beam, collision data and simulation study has been performed to study and analyse the characteristics and rejection of spikes as seen in here [53]. As a result, most of the results presented in this thesis are

taken directly from [53] or redone for 2012 dataset which this analysis is based upon. It has been observed through studies using minimum bias data set(highly populated with neutrons and charged hadrons) at different center of mass energy, that the number of spikes increases with the proton collision rate as well as the charged tracks per event i.e there is a strong linear correlation between spike rate and the center of mass energy of pp collision. The reason for this is because more neutrons and charged hadrons with enough energy are produced which "punch through" the APD and produce hikes in the rechit energy profile as read from the APDs. It is understandable that spike production is most common in the barrel compared to the endcap. Thus with increases rate of proton collision and $\sqrt{S} = 8$ TeV, it is imperative to have robust variables which can identify and reject spikes in the barrel in this analysis. The above studies show that variables defined using timing and EM energy deposits are reliable. Other variables using the timing pulse shape and EM shower profile can be used in addition to identify and rejects spikes with efficiency of 90 to 95%.

Rejection of spikes is done at online(CMS Level-1 trigger level) as well as offline and analysis level.

At online, the strip Fine-Grained Veto Bit(sFGVB) is set to 0 or 1 use to flagging an object as either a spike or a good event respectively. A detail of this can be found in [54]. For example if the sFGVB is set to 0 and the trigger tower(5×5 crystals) transverse energy is below 12 GeV, the energy deposition is considered spike-like and the corresponding tower will not contribute to CMS triggering of that event. The sFGVB was implemented in 2011 data taking process and was measured to reject over 95% of spikes with transverse energy greater than 8 GeV (12 GeV) in 2011(2012). The figure **Figure of sFGVB** shows the difference between an good EM-cluster and a spike-like cluster at sFGVB level.

At Offline, variables making using of the single(at times double) channel(crystal) energy deposit and early arrival time of spikes are defined. In figure **Figure of Swiss X and Rechit Time**, we show the difference between spikes and normal events energy clusters explaining the variables used to identify spikes in the offline. The topological variable constructed as $1 - \frac{E_4}{E_1}$ also known as "Swiss-cross" where E_1 is the energy deposit of the central(highest energy) crystals and E_4 is the sum of the energy of the neighbouring crystals in an $\eta - \phi$ plane is used for identifying isolated spikes. The figure **Figure of**

Spike energy topology and Distribution of SwissX shows the construction of the swiss-cross variable as well its distribution in data and simulation events. The peak at 1.0 in data of the distribution is due to the presence of spikes. A cut in Swiss-cross > 0.95 rejects more than 99% of isolated spikes with transverse energy greater than 10 GeV with very little impact on the efficiency of selecting electromagnetic EM showers. Other topological energy deposit variables such as $1 - \frac{E_2}{E_6}$ and $1 - \frac{E_2}{E_9}$ where E_2 is the sum of the energy of two crystals sharing the energy deposited and $E_6(E_9)$ is the sum of the neighbouring 6(pairs-of)(9) crystals in the $\eta - \phi$ plane. The $1 - \frac{E_2}{E_6}$ variable is used for the identification of isolated spikes whose energy deposit spread in two adjacent crystals while the $1 - \frac{E_2}{E_9}$ is used to identify non-isolated spikes or spikes which are found embedded in a normal Ecal supercluster.

The figure **Put figure of di-spike and non-Isolated spike construction and distribution** A cut on $1 - \frac{E_2}{E_6}$ ($1 - \frac{E_2}{E_9}$) greater than 0.95 (0.98 for tight) gives an efficiency close to 95% for events with transverse energy greater than 10 GeV for rejecting spikes with very little effect on normal EM shower reconstruction.

Another very important variable used for rejecting spikes with greater efficiency is rechit ECAL timing. Spikes and EM energy deposits show very distinct signal pulse shapes. Since spikes do not in the PbWO₄, when the pulse shape is fitted to extract the timing of a signal, the spikes appear "early" due to faster rise time of the spike pulse. The figure **Fig of spike pulse shape and rechit time distribution for data and simulation** shows the comparison between the pulse shape for a spike candidate pulse and true PbWO₄ scintillated event. The adjacent plots shows the distribution of the rechit time for simulation(where there are no anomalous signals) and collision data where anomalous signals have a significant contribution to out-of-time signals. A cut on timing of ± 3 ns gives greater than 90% efficiency for rejecting spikes however, in this thesis, we do not employ this timing cut as we are actually searching for delayed objects whose timing can be beyond the ± 3 ns window.

However, it is worth noting that, these anomalous signals if not rejected will lead to a biasing in the reconstruction of other physics variables such as missing transverse energy(E_T^{miss}) as well as being miss-identified as a possible signal for delayed photons. Infact the spike rate per bunch crossing as observed in [54] was approximately 1×10^{-3} in collisions bunch crossings while in non-collision bunch crossing is of the order of 2×10^{-6}

in non-collision bunch crossings. This spike rate from non-collision rate is obtained from cosmic muon data recorded during June-August 2009 while the spike rate for collision is obtained from Minimum biased(Soft proton-proton) collision events data. Thus, in this thesis, we have restricted ourselves to using only the energy topological variables discussed in previous paragraphs to identify and reject anomalous signals.

5.3 Using Timing for Event Cleaning

Energy RecHits and clusters used in the reconstruction of higher level objects are required in addition to cluster cleaning conditions, to pass certain selection criteria using transverse energy and ECAL timing. For the case of photon, electron, PF jets and E_T^{miss} reconstruction, the basic and super-clusters are required to be seeded by seed crystals whose time is within approximately 3 ns in the barrel and 7 ns in the end-caps. These are called *in-time* RecHits. These RecHits are the standard RecHits used in the reconstruction for most physics objects used in physics where timing is not an important variable. The choice for using timing, is because, timing combined with other topological variables is an excellent variable to identifying and rejecting readout electronic crystals with large noise, poorly reconstructed RecHits, RecHits from anomalous signals, RecHits from machine induced events and cosmic muons as well as improved timing calibration. However, for physics analysis like our case of searching for long-lived particles, this cleaning procedure is not useful. As rejecting RecHits with time more than 3 ns also known as *Out-Of-Time* RecHits will remove super clusters from potentially delayed electrons and photons which defines the signal for new physics. Thus in this analysis, we combined all classes of RecHits, and do not reject RecHits with large reconstructed time except if the time is well beyond expected time for physics objects produced in proton-proton collisions within the required Bunch Crossing time spacing of 25 ns or 50 ns. The electromagnetic objects in this analysis are reconstructed from the combined sample of time cleaned and unclean RecHits. All other RecHit cleaning is applied except that which involves RecHit timing information.

Chapter 6

Search Analysis for Long-Lived Particles

6.1 Analysis Strategy

Our analysis performs a search for delayed isolated photons produced with large transverse momentum. It is possible, at least in theory, that events with such photons are produced from the decay of a lightest neutralino, $\tilde{\chi}_1^0$, produced from the cascade decay of gluinos and squarks or other massive supersymmetry particles or an entirely new particle. Within the context of supersymmetry, in addition to the delayed high p_T , isolated photon, an associated gravitino, \tilde{G} , also produced in neutralino decay, is very weakly interacting with detector material. As a result, its presence is indirectly inferred using missing transverse momentum whose magnitude is E_T^{miss} , as being part of the possibly observed event. Observing such an event at the LHC, using the CMS detector, would represent a clear signal for new physics as such events are not expected to be produced from standard model interactions. However, from an experimental point of view, using timing measurements from ECAL sub-detector in making such observations must be handled with ultimate care as there could be many different sources of isolated, high p_T and even delayed photons due to timing miss-measurements and poor event reconstruction. A few of these sources which have been identified are high p_T , isolated and delayed photons from timing miss measurements and miss-identification, photons produced from cosmic and other proton beam related activities like *beam halo* muons

producing photons through the process of *bremstrahlung* in the ECAL, and obviously detector effects like high p_T neutrons by-passing the PbWO₄ crystals and hitting directly the photo-detectors, APD and VPT, mimicking the behavior of isolated, delayed and high p_T photons. The latter kind of photons are called *spikes*. These photons can be identified as isolated, having high p_T with ECAL time measurements showing that they arrive early as well as late compared to "normal" photons produced at the nominal proton-proton interaction region whose average arrival time at ECAL is 0 ns. These different sources of background makes it challenging to distinguish a possible signal photon from the separate background photons. Thus, estimating the background contributions to possible signal events sample requires using true proton-proton collision events rather than simulated events which do not accurately mimic proper timing measurements for this kind of background events as is normally the case in most physics analysis. Nevertheless, as it is with most hadron collider physics analysis, exploring the use of the number of jets in the event selection can most often reduce dramatically the background contamination to possible signal sample. It is not different with this analysis, where we have employed *jet multiplicity* both as a possible signal definition requirement for the production of high p_T isolated and delayed photons but also as a detector variable for reducing and at times discriminating background from possible signal events. Our motivation is to perform a model independent search while at the same time guided by SUSY models such as SPS8 benchmark model and GGM, where the production of a high p_T isolated, delayed photon in association with a number of jets and large E_T^{miss} constitutes a typical new physics event which could be produced at the LHC. Thus, our simulated events from SPS8 or GGM model, serves both as a guiding model for understanding a possibly observed event with a new physics signature and also for setting limits on some fundamental parameters with respect to these models in case we observed no significant excess over SM prediction.

A typical signal event considered in this analysis for the existence of a neutral massive long-lived particle decaying into a photon, is the detection of a late photon arriving at crystals in the ECAL sub-detector of CMS associated with jets and large E_T^{miss} . In the SPS8 model with R-parity conservation (RPC), the neutralino ($\tilde{\chi}_1^0$) is the long-lived neutral particle and decays into a high p_T isolated and late arrival photon in association with at least two jets and a weakly interacting gravitino (\tilde{G}) in a signal event. The jet

multiplicity is from jets produced in the cascade decay of possibly higher mass SUSY particles into the neutralino. The gravitino (\tilde{G}) presence is inferred using the transverse momentum imbalance whose magnitude is E_T^{miss} . Using this signal events signature, we divide our data samples into possible signal regions (SR) and control regions (CR) and use these CRs for estimating background contributions from beam related activities, miss reconstructed standard model processes and detector effects. We also use events with negative photon time as a control sample for studying veto methods for rejecting and estimating background contribution from non-collision events.

6.1.1 Signal and Background Modelling

We begin generating signal events according to the SPS8 GMSB model by producing Supersymmetry Les Houches Accord (SLHA) files using the SUSY software package *ISASUSY*,[67]. *ISASUSY* contains the program *ISAJET* which is used to determine SUSY mass spectrum and decay parameters according to a given SUSY model. The input to *ISAJET* are the fundamental parameters $\{\Lambda, M_{\text{mess}}, N_5, \tan(\beta), sgn(\mu), C_{\text{grav}}\}$. According to the SPS8 benchmark model, we have chosen, $sgn(\mu) = 1$, $\tan(\beta) = 15$, $N_5 = 1$ and $M_{\text{mess}} = 2\Lambda$ allowing C_{grav} and Λ as the free parameters to study the different life time and mass of the neutralino. The output of *ISAJET* is a SLHA file that has the SUSY mass spectrum and decay rates and branching ratios according to the SPS8 model. *HDECAY* is used as the tool for simulating the decay of SUSY particles including the neutralino to gravitino. The neutralino can also decay into Z bosons, *Higgs* and e^+e^- with a gravitino but with about 83 to 94% of its decay into $\gamma + \tilde{G}$. 97 to 99% of all the events contain at least a single photon. These SLHA files containing information about the SUSY mass spectrum and decay rates is fed into a *PYTHIA6*, [68], proton-proton collision event generation interface of the CMS software (CMSSW) event generation and reconstruction software. In our case **CMSSW_5_3_2_patch7** version of the software is used. The center of mass energy for these proton-proton collisions $\sqrt{8}$ TeV for generating these SUSY events. Production, interaction and decay of these events in the CMS detector is simulated using the GEANT4 package,[69]. Since a possible background process to our analysis is miss-measurement of the timing of photons produced by Standard Model processes like multi-jets and $\gamma +$ jets processes produced

from strong interactions described by quantum chromodynamics (QCD), we also generate and simulated at leading order cross-sections using PYTHIA 6 and GEANT4 a small sample of these events for determining an estimate of time miss-measurement of our signal Monte carlo events. Digitization and event reconstruction in terms of its constituent objects like jets, photons, muons and electrons, after production and decay in the full CMS detector is later again performed during analysis using the CMSSW software.

Simulated Signal Events

Our signature for signal events within the SPS8 benchmark model are events containing the following:

- at least one energetic delayed photon,
- a number of high transverse momentum jets,
- large missing transverse momentum,

Simulated Background Events

QCD multi-jets and $\gamma +$ jet(s) events with high p_T photons with miss reconstructed photon time is a possible background source. In order to understand and calibrate for any such miss measurements, we use simulated or Monte Carlo $\gamma +$ jet(s) events to perform such a study and for sanity check with MC time measurements. Events with W and Z decay and $t\bar{t}$ with large missing transverse momentum, jets and miss-reconstructed photons could also possibly contribute to background, however, these processes produced mostly in-time events with rarely any photons with large late times. Thus, we consider this background to be negligible and do not perform any MC studies for them.

6.1.2 Datasets

The dataset used in this analysis was produced during proton-proton collisions of LHC Run 1 in 2012 with the center of mass energy, $\sqrt{S} = 8$ TeV. The CMS detector recorded data equivalent to total integrated luminosity of 19.1 fb^{-1} .

Data

These datasets contain events with at least a single photon triggered. Only datasets for which the luminosity-sections are certified as GOOD are used. The *jason* file with this good luminosity sections is **Cert_8TeV_PromptReco_Collisions12_JASON.txt**. Table 6.1 shows the dataset and their corresponding integrated luminosity as used in this analysis.

Dataset	Recorded Luminosity [fb ⁻¹]
/Run2012B/SinglePhoton/EXODisplacedPhoton-PromptSkim-v3	5.1
/Run2012C/SinglePhoton/EXODisplacedPhoton-PromptSkim-v3	6.9
/Run2012D/SinglePhoton/EXODisplacedPhoton-PromptSkim-v3	7.1
/SingleElectron/Run2012A-22Jan2013-v1/AOD	5.2
/DoubleElectron/Run2012C-22Jan2013-v1/AOD	4.8

Table 6.1: Dataset and corresponding integrated luminosity totaling 19.1 fb⁻¹ used in this analysis

Background and Signal Monte Carlo

The Monte Carlo (MC) samples are produced taking into account the Summer 2012 prescriptions carrying information on the calibration and alignment conditions of the CMS detector with pile up (PU) conditions at 8 TeV. We generate QCD events at leading order (LO) cross-section (σ) and normalized to the 19.1 fb⁻¹ integrated luminosity. The official CMS MC production events for signal GMSB contains 50000 events. Performing a quick sanity check by measuring and comparing the generated neutralino lifetime ($c\tau$) to its lifetime from SLHA files produced with ISAJET, we observed that most of the generated neutralino events had their lifetimes reduced by a factor of about 3. In order to extend our study to longer neutralino lifetimes, we produced private GMSB samples, generated and simulated with the same conditions as the official CMS samples but having correctly produced and measured neutralino lifetimes thus extending the GMSB sample to include neutralinos with long lifetimes. These combined GMSB MC samples from private and official simulations allow our search analysis to scan neutralino ($\tilde{\chi}_1^0$) lifetimes, $c\tau$ from 250 mm to 12000 mm for each Λ_m point with Λ_m ranging from

100 TeV to 180 TeV as shown in table 6.2. Table 6.3 also show the p_T range for the processed QCD samples.

Λ [TeV]	$c\tau$ (mm)	σ_{LO} (pb)	Number of Events	Branching Ratio
100	250-12,000	0.368	50,000	0.9444
120	250-12,000	0.133	50,000	0.9042
140	250-12,000	0.0574	50,000	0.8711
160	250-12,000	0.0277	50,000	0.8464
180	250-12,000	0.0145	50,000	0.8282
220	250-12,000	0.0044	50,000	0.8282
260	250-12,000	0.0015	50,000	0.8282
300	250-12,000	0.0008	50,000	0.8282

Table 6.2: The signal GMSB SPS8 MC samples for difference Λ and Branching Ratios used in this analysis

\hat{p}_T	σ_{LO} (pb)	Number of Events
50 ~ 80	3322.3	1995062
80 ~ 120	558.3	1992627
120 ~ 170	108.0	2000043
170 ~ 300	30.1	2000069
300 ~ 470	2.1	2000130
470 ~ 800	0.212	1975231

Table 6.3: The $\gamma+$ jets samples used in this analysis

6.2 Event Selection

The major background events to this analysis are events which are not produced from the nominal proton-proton collisions. These events can be separated into three major categories; *Halo* muons, *Spikes* and *Cosmic muons*. In addition to these events, there are also QCD events which mimic the $\tilde{\chi}_1^0 \rightarrow \gamma + \tilde{G}$ decay due to photon miss reconstruction and measurement of fake E_T^{miss} . Contribution from $\gamma+$ jets events can also be regarded as background events especially in cases there is a real isolated photon and a fake E_T^{miss}

due to miss identification of jets as photons. Even though the event topology for most $\gamma +$ jets events is quite different from that of GMSB signal events.

Another possible background contribution, in addition to QCD multi-jets events, events from ElectroWeak (EWK) decay including $W \rightarrow e + \nu$ and $t\bar{t}$ decays, where the top (t) decays to a b quark and a W 100% of the time. The electron is miss reconstructed and thus miss identified as a photon and real E_T^{miss} is measured due to the presence of the neutrinos (ν). We can easily reduce this background by requiring high jet multiplicity events since most of these EWK and QCD events contains low number of high p_T jets in them. In order to maintain a high background rejection and good signal selection efficiency, we select events with at least two jets. This helps to reduce EWK and other low jet multiplicity backgrounds contributions prior to additional photon quality selections based on the isolation and electromagnetic shower profile. Using ECAL time measurements, our signal acceptance regions are events with photons whose time is between $3 < t_\gamma < 13$ ns. This cuts allows us to avoid events with high spike contamination.

In addition to collision backgrounds mentioned in the previous section, non-collision originated background events like Cosmic muons, beam halo muons and ECAL spikes contain photons with large reconstructed time and large E_T^{miss} measurements. E_T^{miss} measurements includes p_T from all reconstructed particles in an event with the assumption that these are events from the nominal proton-proton collision. However, not all events are produced from collision. Cosmic muons, beam halo muons, spikes, ECAL and HCAL noise can all contribute to the total sum of the measurable event p_T imbalance. In some events these provide the major contributions to E_T^{miss} calculations. We begin by selecting events with at least a good vertex, quality jets, satisfying ECAL spike cleaning, DT time cosmic muon cleaning and CSC tight halo-muon cleaning criteria. This event selection criteria is very useful in reducing contributions from non-collision events.

A typical diagram showing both non-collision and collision backgrounds in neutralino production and decay from LHC proton-proton collision within the CMS detector is shown in figure 6.1. A typical GMSB decay of the neutralino is also shown in this

diagram indicating the two different sources for delayed photon produced from this decay.

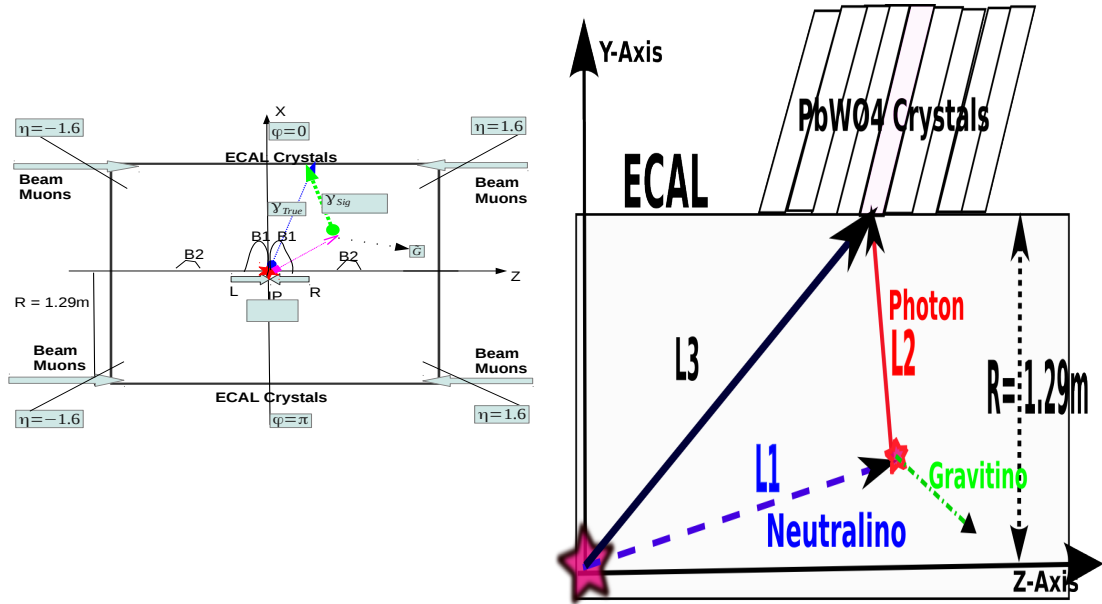


Figure 6.1: Schematic diagram showing $\tilde{\chi}_1^0 \rightarrow \gamma + \tilde{G}$ decay topology within the ECAL volume of the CMS detector. Proton beams are also shown showing the possible production of collision and non-collision delayed photons

6.2.1 Trigger

Our pre-event selection begins online by selecting only events which pass our online higher level trigger (HLT). The HLT trigger used for our $\sqrt{S} = 8$ TeV proton-proton collision analysis is the `HLT_DisplacedPhoton65_CaloIdVL_Isol_PFMET25` seeded by `HLT_L1SingleEG12` level 1 trigger. It was developed primarily for the study of displaced photons. To avoid bias in event selection towards any particular model, this trigger only requires that an accepted event contains an isolated photon with a p_T threshold of 65 GeV/c and E_T^{miss} above 25 GeV. The photon shower shape must also satisfy $0.1 < 0.S_{\text{Minor}} < 0.4$. We study our trigger efficiency and turn-on curve (efficiency becomes close to 100%) for selecting events with delayed photon candidates. In order to avoid any correlation between the photon and E_T^{miss} variables, we study efficiency for each variable separately using another trigger `HLT_Photon50_CaloIdVL_Isol`.

The selected photon candidates for studying this HLT photon efficiency must pass our offline photon selection candidate criteria shown in table 6.4. The HLT photon selection efficiency for p_T is defined as the fraction of offline reconstructed photons to those triggered by *HLT_IsoPhoton50* photon candidates within $\Delta R < 0.5$. Similarly, the E_T^{miss} HLT efficiency is defined as the fraction of events containing at least a jet and E_T^{miss} more than the HLT required E_T^{miss} of 25 GeV. The results of the trigger efficiency measurements are shown in figure 6.2 against photon p_T and E_T^{miss} . These efficiency studies are made using the *HLT_Photon50_CaloIdVL_IsoL* trigger which has no E_T^{miss} and jet multiplicity requirement as the denominator and the *HLT_DisplacedPhoton65_CaloIdVL_IsoL_PFMET25* as numerator. A *SinglePhoton* dataset is used to verify these efficiency while and GMSB and $\gamma +$ jets samples is used to derive any correction factors between data and MC events.

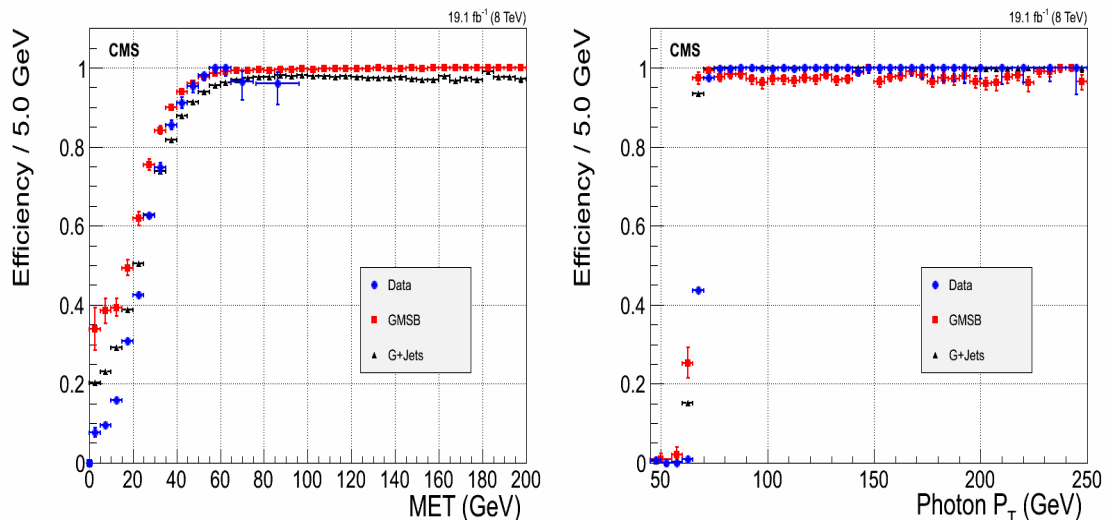


Figure 6.2: Trigger efficiency turn-on curves for photon p_T and $E_T^{\text{miss}} > 25$ GeV (left) and for E_T^{miss} with photon $p_T > 80$ GeV/c (right). The $\gamma +$ jets samples require photon $p_T > 170$ GeV/c for selecting events with true E_T^{miss} .

6.2.2 Offline Selection

Our offline event selection requires candidate events in addition to passing our HLT trigger, contain at least a single photon, a jet and E_T^{miss} . The photon object collection used in our analysis is an extended collection of standard CMS Egamma photon

objects collections to include events classified as “*out-of-time*”. This classification was performed during the official CMS supercluster reconstruction process. This enlarged photon sample include events like spikes, ECAL noise, photons from beam halo and cosmic muons and detector malfunctions. It is also entirely possible that this collection also contains true candidate delayed photons which is our signal events. The selected photons are required to pass the photon selections criteria in table 6.4.

Photon Identification and Selection Criteria	
Criteria	Requirement
Event leading photon must have $p_T(\gamma^1)$	$> 80 \text{ GeV}$
Other photons in event must have $p_T(\gamma^{>1})$	$> 45 \text{ GeV}$
$ \eta_\gamma $, (Barrel Only),	$< 3.0 (< 1.5)$
S_{minor}	$0.12 \leq S_{\text{Minor}} \leq 0.38$
\mathbf{H}/\mathbf{E}	< 0.05
$\Delta R(\gamma, \text{track})$	> 0.6
HCAL Iso	< 4.0
ECAL Iso	< 4.5
Track Iso	< 0.2
Photon Isolation cone size $\Delta R(\gamma, \text{otherparticle})$	< 0.4
Topological Spike cuts	$1 - E_6/E_2 < 0.98, 1 - E_4/E_1 < 0.98$

Table 6.4: The photon identification and selection criteria used in this analysis

The presence of jets as associated particles from gluino cascade decay and the gravitino (\tilde{G}) from neutralino decay, $\tilde{\chi}_1^0 \rightarrow \gamma + \tilde{G}$ requires jet identification and E_T^{miss} or \cancel{E}_T selection criteria as well. Our jet and E_T^{miss} or \cancel{E}_T selection criteria is based on the particle-flow (PF) algorithm. Additional $\cancel{E}_T > 65 \text{ GeV}$ due to the flatness of the HLT trigger efficiency against E_T^{miss} (see figure 6.2). Table 6.5 show a summary the jet identification and selection criteria with the threshold requirements used in this analysis.

Jet PF identification selection criteria

Criteria	Requirement
Jet p_T	$> 35 \text{ GeV}$
Number of Jet constituents	> 1
Charge EM energy fraction (CEF)	> 0.99
Neutral Hadron energy fraction (NHF)	< 0.99
Neutral EM energy fraction (NEF)	< 0.99
If $ \eta $ of jet is > 2.4 , Charge Hadron energy fraction (CHF)	> 0
If $ \eta $ of jet is > 2.4 , Charge multiplicity (NCH)	> 0
$\Delta R(\gamma, \text{jet}) = \sqrt{(\phi_\gamma - \phi_{\text{jet}})^2 + (\eta_\gamma - \eta_{\text{jet}})^2}$	> 0.3

Table 6.5: The Jet ID selection used in this analysis

E_T^{miss} Corrections

During the official CMS electromagnetic supercluster reconstruction, timing cuts of $|t_{RECO}| > 3.0 \text{ ns}$ in EB is used for cleaning “out-of-time” events. As a result, the p_T contribution from out-of-time photon events is not included in the calculation of E_T^{miss} or \cancel{E}_T . This introduces a difference in the calculation of \cancel{E}_T for “in-time” events ($|t_\gamma| < 3.0 \text{ ns}$) and “out-of-time” events ($|t_\gamma| > 3.0 \text{ ns}$). Since the out-of-time photon E_T is not included in the sum total transverse momentum of an event to derived the total transverse momentum imbalance, we correct for this, by adding the out-of-time photon E_T to the PF-MET measured during CMS \cancel{E}_T reconstruction. We defined an additional variable, \cancel{E}_T^γ , accounting for this correction and use this variable in our event selection criteria.

1. \cancel{E}_T : PF-MET, \cancel{E}_T from CMS standard E_T^{miss} measurements.
2. \cancel{E}_T^γ : PF-MET with photon E_T added i.e $\cancel{E}_T^\gamma = \cancel{E}_T + E_T$ of the out-of-time photon.

Our signal event selection criteria is defined as events with $\geq 1 \gamma + \geq 2 \text{ jets} + \cancel{E}_T^\gamma > 60 \text{ GeV} + \cancel{E}_T > 60 \text{ GeV}$

We use a control sample to perform a closure test of our background estimation procedure. The selection criteria is events with $\geq 1 \gamma + \leq 1 \text{ jet} + \cancel{E}_T > 60 \text{ GeV} + \cancel{E}_T^\gamma > 60 \text{ GeV}$

6.2.3 ECAL Time

The photon arrival time at ECAL is our main observable for distinguishing background from signal. However, the presence of spikes, noisy crystals and pile-up events, require measuring the photon time with methods which are robust to timing bias from such events. There are different ways to measure the photon time using ECAL. The reference time is the time measured from a relativistic electromagnetic object like a photon produced from nominal proton-proton collisions arriving at ECAL in an average time of zero. The photon time is measured using either of the following methods:

- *Seed Time*: Time from the highest energy crystal, which is not a spike, of the photon supercluster.
- *Cluster Time*: Error weighted average time of all the crystals in the seed basic-cluster of the photon supercluster.

Timing reconstruction as described in chapter 4 is the extraction of time from the pulse shape through a fitting method. The χ^2 obtained from the fit determines how well the time is reconstructed. One way of rejecting fake photons which are either jets miss-identified as photons or spikes is to use the fitted χ^2 . Studies performed have shown that a $\chi^2 < 4$ cut improves the ECAL timing resolution by rejecting spikes and anomalous photon events as possible. Figure 6.3 shows a comparison between the pulse shape profile of a spike and that of a good event.

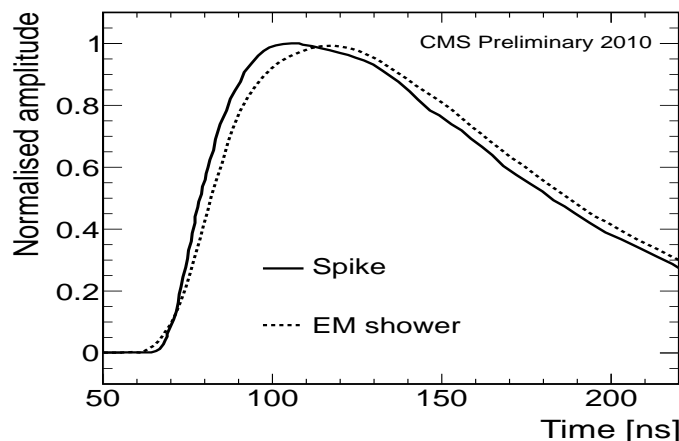


Figure 6.3: Pulse shape profile showing a spike (solid line) and a real photon (dashed line) from data.

In this thesis, we measure time using the seed crystal time approach. Our choice of seed time is based on a number of independent timing analysis performed comparing the timing resolution obtained from cluster time to the seed time. We observed the cluster timing method to be very biased towards the time of an isolated spike especially when the spike is embedded in a photon object. The timing resolution especially for large timing events is much better compared to the cluster time measurement method which is an essential region when searching for new long-lived particles. Figure 6.4 shows the timing measurements of photons using either seed time or cluster time. The seed time show an approximate timing resolution of 400 ps compared to 450 ps with a broad timing tail from using the error weighted average cluster time. The cluster time method is also computational time and resource consuming.

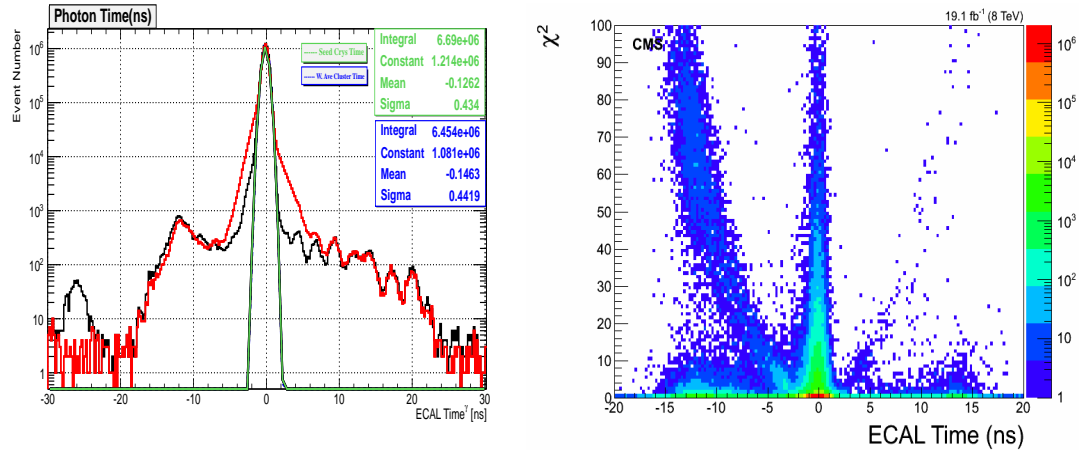


Figure 6.4: Timing distribution of photons showing timing measurements using seed crystal (black) and using Weighted Average basic cluster time (blue). Resolution (σ) from seed time is better compared to that for cluster time which is computationally intensive. Together with the χ^2 , the seed time performs better in identifying anomalous timing objects.

Monte Carlo simulation of ECAL timing is challenging as the time of anomalous events such as spikes and noisy crystal channel present during data taking aren't well simulated. To account for MC and data timing measurement differences, We use QCD simulated $\gamma + jets$ events and select events containing only one or two jets and study the

distribution of the difference between the generated time (T_{GEN}) and the reconstructed MC event time (T_{RECO}) in a timing window of [-2, 2] ns. Comparing this difference to data, the difference in the mean time between the data and MC $\gamma +$ jet sample is used to smear the reconstructed time of the MC samples to be comparable to true reconstructed time in data. A difference of about 125 ps is observed between the timing from data and MC. Timing from the smeared MC sample show a close agreement with data. Figure 6.5 show this comparison before and after timing calibration (smearing adjustment) is applied on the MC samples.

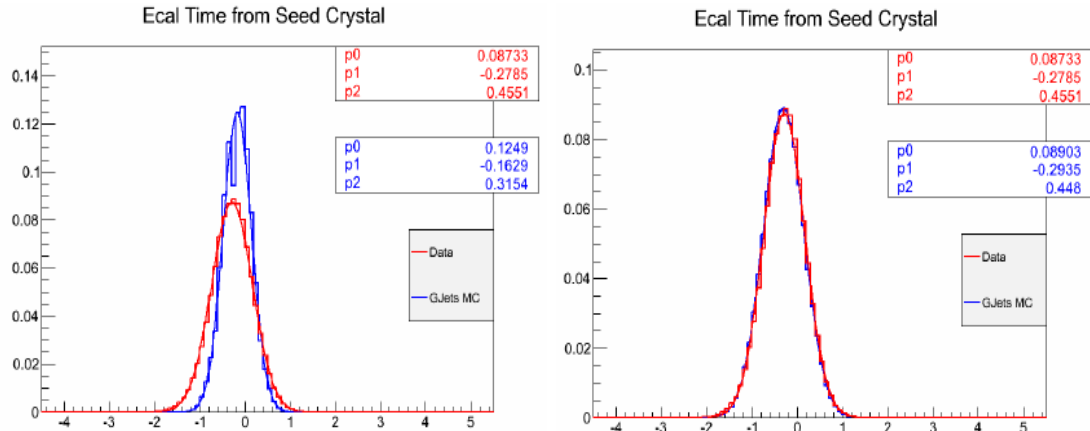


Figure 6.5: Timing distribution of photons showing timing of data and MC $\gamma +$ jets (blue) samples and data (red) before (left) and after (right) timing Calibration is applied to MC.

It is worth noting that the difference of 125 ps between T_{RECO}^{MC} and T_{RECO}^{DATA} compared to 500 ps ECAL timing resolution is not enough to influence event selection, however event distribution in the tails remains a major concern.

The ECAL timing distribution for photons with $pt > 50$ GeV in the ECAL (barrel and endcap inclusive i.e $|\eta_\gamma| < 3.0$) show timing distributions (see figure 6.6)

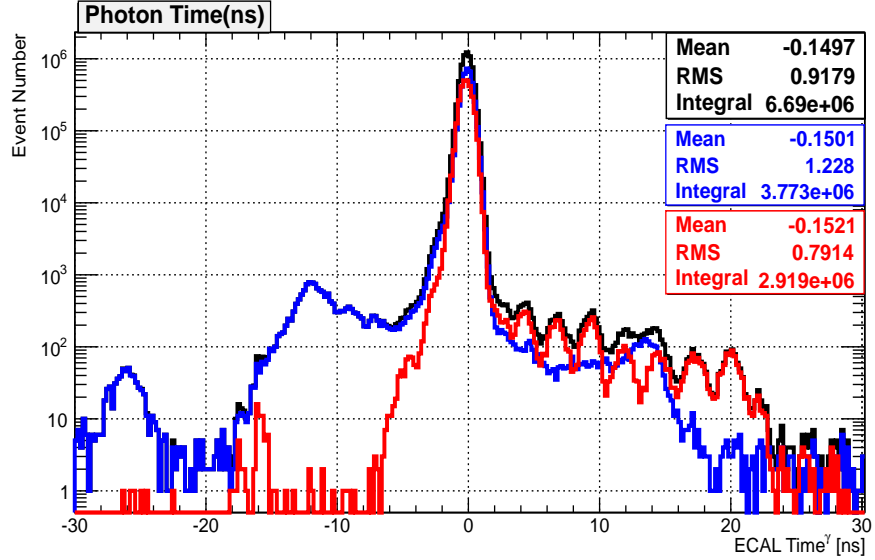


Figure 6.6: ECAL timing distribution of photons in barrel (EB), endcap (EE) and all of ECAL (ALL ECAL) with $p_T > 50$ GeV from data. A 2.5 ns delay timing structure is observed in endcap subdetector.

with a clear 2.5 ns discrete pattern with most of these photons arriving in the endcap, $1.47 < \eta < 3.0$ compared to the barrel, $|\eta| < 1.47$. These are photons produced from collisions of *Ghost* and *Satellite* bunches with either the main proton collision bunch or *Ghost/Satellite*. They contribute an irreducible amount to the photon time distribution which is very challenging to reject or estimate quantitatively. A rough estimate can be obtained by looking at ratio of the proton population in the filling profile of the LHC RF cavities as mentioned in section 3.1.5 of chapter 3 which gives a factor 10^{-5} compared to contributions from the main proton-proton bunch collision. It is observed that contribution from ghost bunches is in the endcap crystals, since very few these photons are produced with enough p_T compared to those from main proton bunch collisions. And even if they do, the ratio of photons from these secondary proton collision to that of the main proton-proton collision is of the order of 10^{-5} at most. As a result of this, we do not use the endcap in this analysis in addition to the fact that timing resolution in the endcap is relatively poor compared to the barrel. We check and validate this factor 10^{-5} using events with $Z \rightarrow e^+e^-$ since Z events do not require high p_T during production and must should capture the 2.5 ns timing pattern if present from

ghost/satellite collisions. We study electron candidates with time within [-2.0, 2.0] ns window. We use this in our background estimation method testing as will be discussed in future sections.

Delayed Photon Source

With a well time calibrated ECAL and good MC to data time agreement, we can study the source of delayed photons from neutralino decay in ECAL using its decay kinematics. There are two possible sources for delayed photon from neutralino decay. From Figure 6.1, an estimated photon arrival time at ECAL can be given by the following methods:

- From slow moving neutralinos: $\Delta t_1 = (L_1/c\beta) - (L_1/c)$
- From non-directpath traveled: $\Delta t_2 = (L_1 + L_2 - L_3)/c$
- ECAL measured time = $\Delta t_1 + \Delta t_2$

Figure 6.7 shows the distribution of Δt_1 and Δt_2 indicating that most of our late arrival photons are produced from the decay of slow moving neutralinos, i.e. $\beta \ll 1$, as opposed to photons from non-direct flight or travel path to ECAL. These neutralinos are produced with low p_T such that the ratio $\frac{p_T}{m_{\chi_1^0}} \ll 1$.

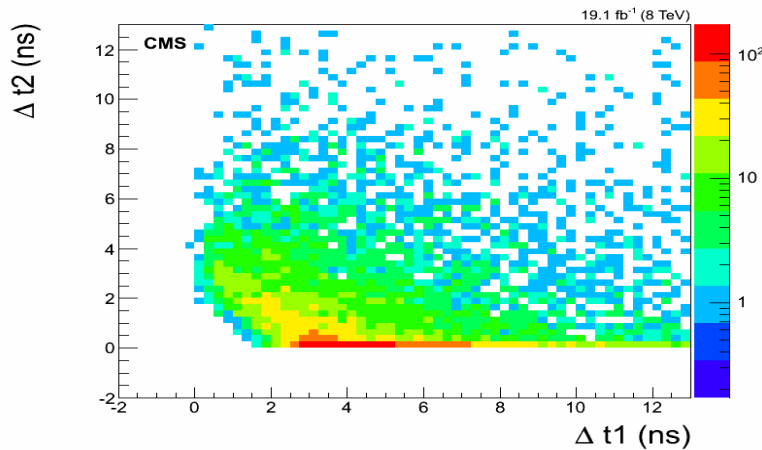
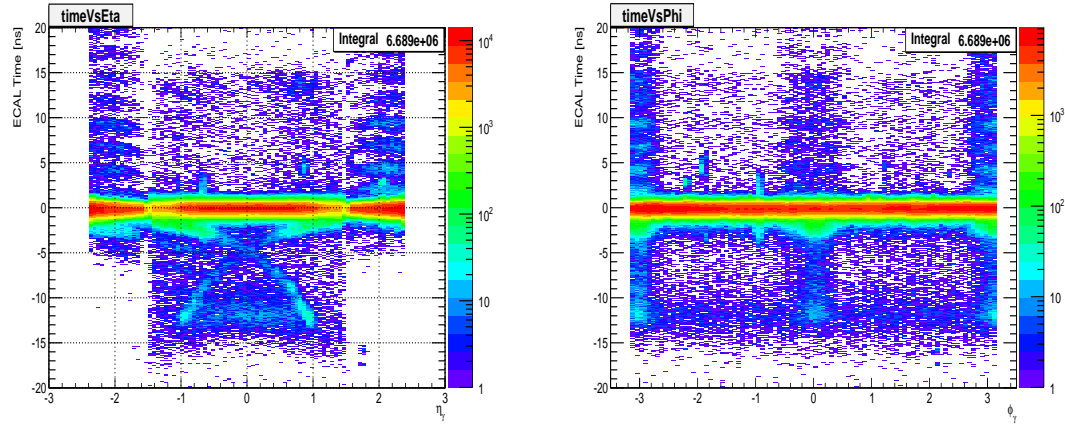


Figure 6.7: Sources of delayed photons produced from neutralino decay in the SPS8 model with $\Lambda = 180$ TeV and $c\tau = 6000$ mm arriving at ECAL.

6.3 Background Estimation

Our background estimation strategy is to first identify and reject as much non-collision background and anomalous events as possible then perform an ABCD background estimation technique on the irreducible residual background. We do this by comparing photon kinematic properties for in-time and off-time photon events. Separating our data sample into jet multiplicity and negative, in-time and positive time enable our approach to be possible. To better understand the different background sources and their contribution we make a two dimensional histogram of the photon η and ϕ against the photon seed time and a one dimensional histogram of the timing distribution for different jet multiplicity events. These events pass the loose selection criteria for photons, jets and \cancel{E}_T already described in the previous section. The photon ECAL time Vs η and ϕ inclusive 2-D distributions are shown in figure 6.8



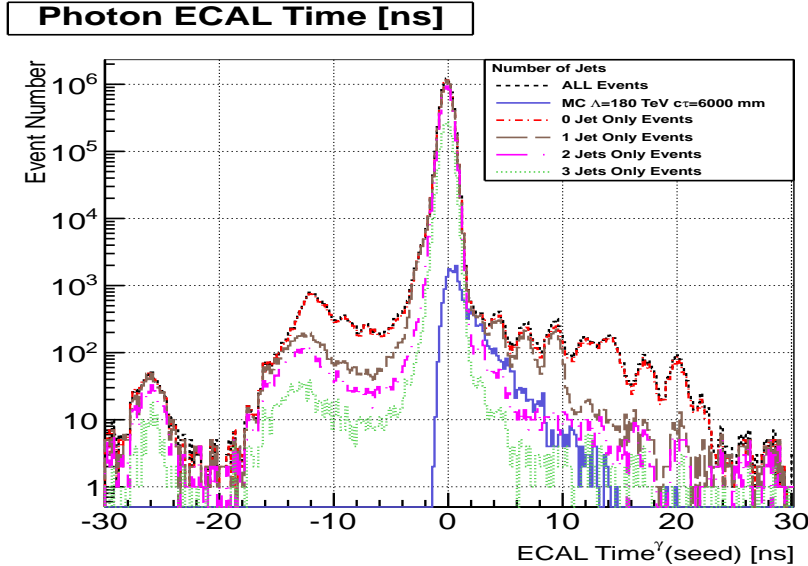


Figure 6.8: ECAL time against η (left) and ECAL time against ϕ (right) for photons with $p_T > 60$ GeV from data. The lower plot shows the photon timing distribution for events with different jet multiplicity.

The histograms in figure 6.8 show contributions from quite a variety of sources. The possible sources considered in this analysis include: QCD processes which we consider to be a combination of γ +jets, multijets and other processes producing photons from nominal proton-proton main bunch collisions. Most of the QCD processes are expected to have minimal contribution to large timing photons and \cancel{E}_T except due to timing miss-reconstruction and \cancel{E}_T miss-measurements or miss-identification of jets as photons. The events with significant contributions of possible or true large ECAL time measurements are produced from machine induce backgrounds (MIB)(arising from ghost/satellite bunch collisions) or beam halo muons, cosmic muons and anomalous events like spikes. These event do not only contribution significantly large photon times but also to large \cancel{E}_T which is our signal selection sample. We employ a data driven background estimation technique in this analysis described briefly as follows:

- Divide the dataset into individual samples peculiar to the expected kinematics and observation of each individual background source,
- Identify observable based on its kinematics which can be used as variables to

identify or tag and reject a particular background contribution with an acceptable amount of efficiency,

- Used alternate samples particular to each background source to calculate and verify the event tagging and miss-tag rate or efficiency,
- Use the tagging and miss-tag rates to estimate the background contribution of each individual background source in a well defined control region (CR) or sample,
- Use another CR as a closure test sample to verify our background estimation method.

All events are selected to be in the barrel i.e $|\eta_\gamma| < 1.47$ as the overwhelming contribution of ghost/satellite bunch collisions observed in the endcap (EE)(see figure 6.6) and poor timing resolutions (≈ 3.0 ns) make it very challenging to extend this analysis to include the endcap (EE). Our data driven method background estimation strategy involves splitting our single photon dataset into two major samples: Events with *Nominal or in-time* photons whose photon ECAL time is within ± 2 ns containing at least 2 jets, and events with *off-timing* photons where the photon ECAL time is $2.0 < t_\gamma < 13.0$ ns and $-10.0 < t_\gamma < -3$ ns with containing 0 or 1 jets. Our signal events are events containing photon(s) with ECAL time, $2.0 < t_\gamma < 13.0$ ns, with at least 2 jets and large \cancel{E}_T . Our motivation is to avoid the observed spike overpopulated region with photon time , $t_\gamma \approx -12$ ns and because high jet multiplicity events are not usually MIB or non-collision events produced with p_T . On the other hand, nominal photons from QCD interaction are mostly produced in-time in association with more than 0 jets.

By comparing these two samples, we develop kinematics variables for studying and reducing contributions from collision and non-collision backgrounds.

6.3.1 Non-Collision Backgrounds

Halo Photons

Muons with energy up to 1 TeV are produced when proton beam collides with collimators at $z = 150$ m from the CMS detector interaction point or when proton beams

collide with residual beam gas in the beam pipes. These are referred to as Beam-Induced Backgrounds (BIB). These muons through the process of bremsstrahlung produce high p_T photons with significantly large ECAL time, deposit their energy in ECAL crystals. The rate of BIB produced photons depend on the beam current and the operational conditions of the LHC such as machine optics, collimator settings, residual gas densities and filling scheme. These muons which travel in a near parallel flight path to the direction of main proton bunch in the beam pipe are referred to as *halo muons*. We expect halo muons to produce muon tracks in the Endcap muon systems (CSC and RPCs) with corresponding associated ECAL electromagnetic cluster in the ECAL. Halo muons can travel from one side of the detector, along the z -direction, to the other side of the detector if produced with sufficient energy. Their Time-Of-Flight (TOF) with respect to a potential hit position in the ECAL sub-detector can be estimated and measured. The expected arrival time at ECAL of a halo muon traveling parallel along the beam line is estimated using its kinematics given in equation 6.1.

$$t_{\text{ECAL}}^{\text{expected}} = -1/c \left(\pm Z_{\text{cluster}} + \sqrt{Z_{\text{cluster}}^2 + R_{\text{cluster}}^2} \right) \quad (6.1)$$

Z_{cluster} is the photon supercluster position or longitudinal distance along z -axis from nominal interaction point, R is the radial distance of the cluster from the beam line which is equal to $R_{EB,\text{ECAL}} = 1.29$ m and c is the speed of light. One can further show that their expected arrival time in ECAL entirely depends on potential hit positions in ECAL and hence η . This is by reducing equation 6.1 to 6.2.

$$t_{\text{ECAL}}^{\text{expected}} = -\frac{R_{\text{cluster}}}{2c} \exp(-\eta) \quad (6.2)$$

Using this expression, we can compare halo flight path η -dependence as expected to what is observed from data. Our result in figure 6.9(*bottom, right*) confirm our expectation that most of the halo muons are produced from BIBs and tend to always produce photons with earlier (negative) arrival time in ECAL. In addition to using halo flight path to tag photons produced from halo muons, we also use halo muon hit positions in the Cathode Strip Chambers (CSC) matched to photon supercluster positions in the ECAL calorimeter. This is possible since halo muons are not bent in the azimuthal (ϕ) direction by the magnets and are mainly located around the $y = 0$

plane. By measuring the difference in ϕ between the CSC segment position and the ECAL photon cluster, we can associate with high percentage halo muons to photons produced from halo muons in ECAL. We call these photons *Halo Photons* and their matching to these halo muons is represented by a variable we call $CSC(Seg, \gamma)\Delta\phi$. A matching to within 3 deg shown in figure 6.9(*bottom, left*) provide a clear method of separating Halo photons from true photons from collision.

A distribution of the Halo photon time against the photon ϕ_γ shown in figure 6.9(*top, right*) shows that most halo photon are distributed around $\phi = 0, \pm\pi$ in agreement with our expectation since, the magnetic field in ECAL does not affect the flight path of Halo muons.

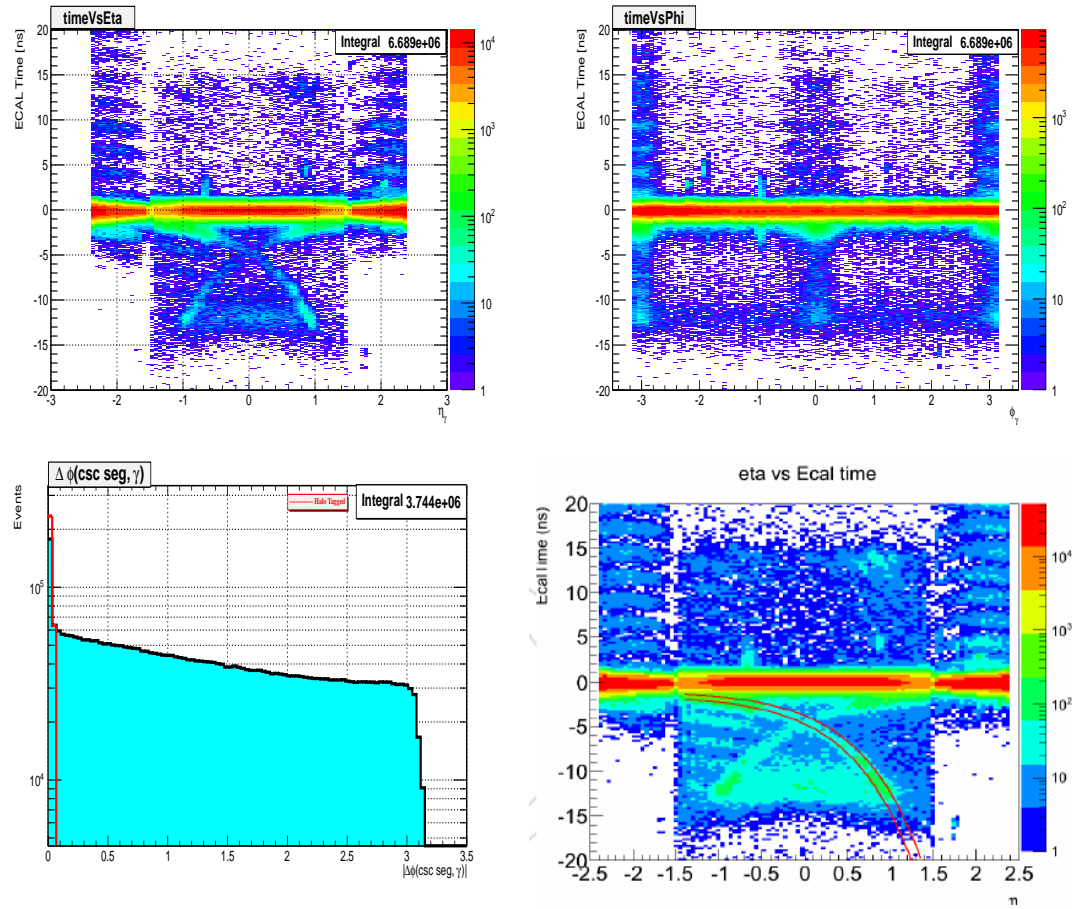


Figure 6.9: ECAL time Vs η (left) and ECAL time Vs ϕ (right) and $CSC(Seg, \gamma)\Delta\phi$ for photons with $p_T > 80$ GeV from data. Halo photons show a clear matched between CSC segments and ECAL cluster in $\Delta\phi$ with their distribution peaking at $\phi = 0, \pm\pi$ and also the shape of their expected time.

Cosmic Photons

Cosmic muons like beam Halo muons with sufficient energy will also bremsstrahlung in the ECAL producing photons referred here as *cosmic photons*. Unlike halo muons, cosmic muons can arrive at ECAL from any direction. Barrel cosmic photons are expected to be produced from cosmic muons with hits in the Drift Tubes (DT) segments. Using the DT hits and their corresponding photon supercluster $\eta - \phi$ position in ECAL, we can match this hit position in DT segments to ECAL photon superclusters within $\Delta\eta$ and $\Delta\phi$. The two dimensional distribution for $DT\Delta\eta(DT, \gamma)$ and $DT\Delta\phi(DT, \gamma)$ for this matching for events with photon time above, $t_\gamma > 2$ ns and time below, $t_\gamma < -3$ ns is shown in figure 6.10. We conclude that events containing photons with small $\Delta\eta$ and $\Delta\phi$ to be candidate cosmic photons. Comparing this to $\Delta\eta$ and $\Delta\phi$ 2-dimensional distributions of photons from a pure cosmic muons sample (data taken when no proton-proton collisions is happening) show these distributions to be very similar as seen in figure 6.10.

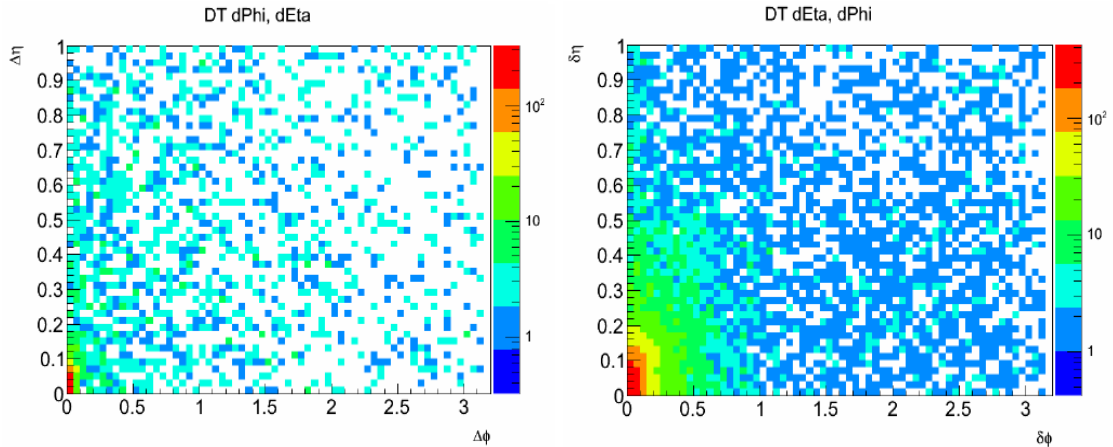


Figure 6.10: 2 dimensional plot showing $DT\Delta\eta(Seg, \gamma)$ against $DT\Delta\phi(Seg, \gamma)$ for photons with $p_T > 80$ GeV, ECAL Time, $t_\gamma > 2$ ns and ECAL Time $t_\gamma < -3$ ns from proton-proton collision data (left) and pure cosmic muon data (right). Small $\Delta\eta$ and $\Delta\phi$ are cosmic photon candidates.

Anomalous Photons: Spikes

Neutrons and some charge hadrons which deposit their energy directly to the APDs instead of the crystal scintillation are referred to as *anomalous signal* or *spikes*. Spikes can mimic the kinematics of true photons from proton-proton collisions leading to the miss-identification of spikes as true photons. Spikes like true energetic photons can be isolated and so easily pass photon isolation cuts without being identified. A spike supercluster usually consists of very few crystals and most of the time single or double crystals except when embedded in a true photon of high electromagnetic fraction jets where they consist of many crystals and are difficult to identify. However, most spikes show a different signal pulse shape to that of true photons and also have large negative ECAL time especially at $t_\gamma \approx -12.0$ ns region. In addition to using energy topological selection cuts, which are based on the spike crystal energy deposits, during ECAL cleaning one can also use the χ^2 fit value of the timing reconstruction to identify and reject spikes. Spike cleaning is performed during online and offline super cluster reconstruction. However, this online cleaning is not entirely very efficient. Since ECAL clusters belonging to spikes are usually made up of very few crystals compared to photons clusters with many crystals, using the number of crystals in a reconstructed super cluster can be used to distinguish true isolated photons from events with spikes. It has been observed that spike contributions increase with increase in LHC luminosity. Thus, as a selection criteria, photons passing our cosmic photons and halo photons identification and with number of good crystals less than 7 are considered to be spike candidates. Figure 6.11 shows the distribution of the number of crystals in a photon super cluster comparing photons with ECAL time, $t_\gamma < 0$ ns, in-time photons (ECAL $-2.0 < t_\gamma < 0$ ns and selected spike and halo control sample. The spike control sample is selected using the spike energy topological cut “swiss-cross” variable in the region with $t_\gamma \approx -12.0$ ns where it is observed that spike concentration is high, is used to identify and reject events with spikes during super cluster reconstruction. We observe as shown in figure 6.11(*left*) that most spikes always have fewer(< 7) crystals in their photon supercluster.

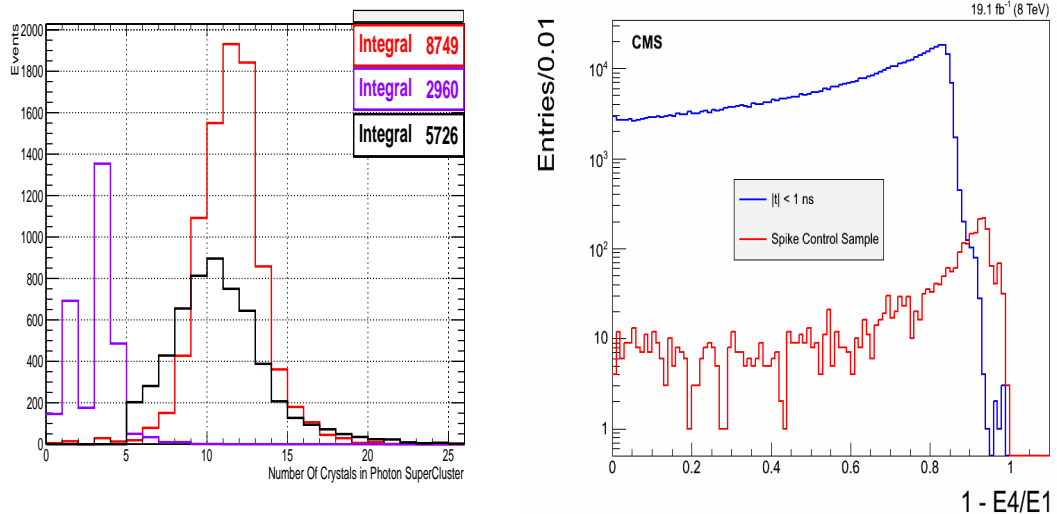


Figure 6.11: Plot showing *number of crystals* in photon supercluster for photons from the region with ECAL Time, $t_\gamma < 0$ ns. Figure shows the timing distribution of candidate true photons(black), spike candidate photons (magenta) and halo candidate photons (red). The toplogical swiss-cross variable ($1 - E_4/E_1$) distribution is shown comparing true photons ($|t_\gamma| < 1.0$) to spike populated sample.

6.3.2 Collision Backgrounds

QCD Photons and Pile Up

Collisions from the main proton bunches happening every 50ns during 2012 LHC Run I are not the only collisions that can occur at the LHC. The presence of satellite/ghost bunches spaced in 5.0 ns or 2.5 ns discussed in section 3.1.5 along LHC bunch structure can also collide producing delayed photons either from collisions between these satellite/ghost bunches or with the main proton bunch. As observed in figure 6.6, photons from these events are a serious background source to delayed photons and most of these photons will pass all the above event and photon selection criteria. Thus, it is imperative to estimate delayed photon contributions from satellite/ghost bunches if it is not negligible. Since these background source is non-reducible and the kinematics of these events are very similar, we employ the standard ABCD method to estimate these background contribution to the signal region. However, we only perform this estimation after cleaning for possibly non-collision event contamination.

6.3.3 Event Cleaning, Veto Performance and Fake Rate

Using the derived kinematic variables for halo, cosmic and spike photons, we apply selection cuts on these variables for tagging and rejecting contributions from non-collision events. These cuts are applied in addition to our above event selections cuts to perform the following event cleaning:

- Veto 0-jet events as this sample is highly populated with beam halo events,
- Veto events with $CSC\Delta\phi(Seg, \gamma) < 0.05$,
- Veto events with $\Delta\eta(DTSeg, \gamma) < 0.1$ and $\Delta\phi(DTSeg, \gamma) < 0.1$.
- Only photons with $|\eta_\gamma| < 1.45$ are considered,
- Veto events with photons with Number of Good crystals < 7 and $1 - E_4/E_1 > 0.98$.
- Remove photons tagged as halo and cosmic photons,
- Veto events with less than 2-jets.

Events which pass all these additional selection criteria make up the sample which is used to estimate our final background to our signal. Since it is very challenging to define pure control samples for each non-collision background source without possible contamination, we estimate the fake rates from the above veto or rejection conditions using in-time ($|t_\gamma| < 2.0$ ns) photon sample where we believe non-collision contribution is small compared to true photons from collision. Our measured fake rates are shown in table 6.9.

Background Source	Fake Rate(%)
<i>Halo Photons</i>	≈ 3
<i>Cosmic Muons</i>	≈ 1.4
<i>Spikes</i>	≈ 0.4

Table 6.6: Fake rates for different non-collision cleaning.

After performing our event cleaning criteria, tagging and rejection of most of halo, cosmic and spike events, our residual background photon timing distribution is shown in figure 6.12 with the different sources of our background tags. We now perform an

ABCD background estimation technique on this residual background to estimate possible contamination of the remaining non-collision background to signal.

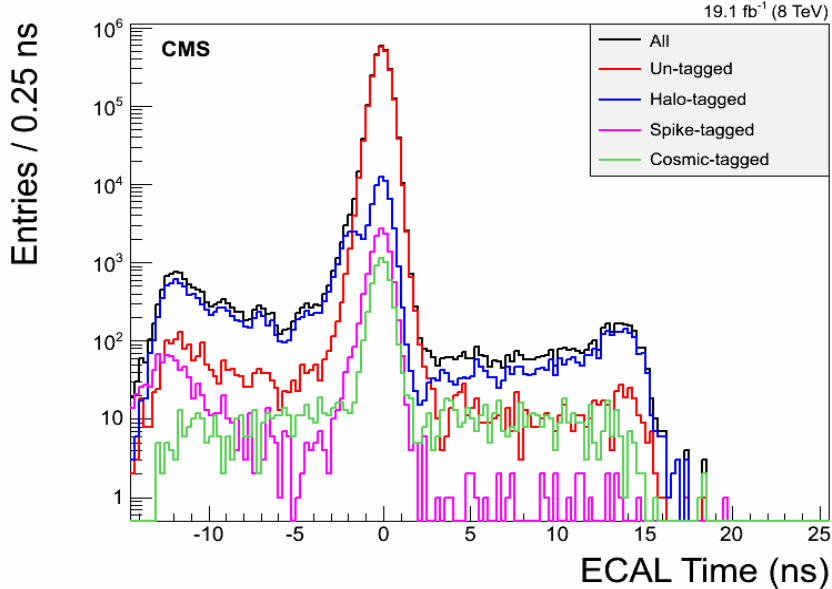


Figure 6.12: Residual Background after tagging the different non-collision background sources using the methods described in text.

Residual Background Estimation Using ABDC Technique

In order to estimating the background contribution from collision and non-collision sources, we employ a 3-dimensional space involving \cancel{E}_T , \cancel{E}_T^γ and photon ECAL time, t_γ . Our signal events are those with $3.0 < t_\gamma < 13.0$ ns with large E_T^{miss} , and by large E_T^{miss} , we mean events with $\cancel{E}_T^\gamma > 60$ GeV, $\cancel{E}_T > 60$ GeV. Non-collision events as already seen can also have large time, since they are mostly out-of-time and by E_T^{miss} calculation and corrections(see discussion above) should have large \cancel{E}_T^γ and small \cancel{E}_T . Events from collision on the other hand are produced mostly in-time ($-2.0 < t_\gamma < 2.0$ ns) except in cases of timing mis-measurements or ghost/satellite contributions where $t_\gamma > 3.0$ ns. Collision events, mostly produced through SM interactions, cannot be produced with large correctly calculated E_T^{miss} , e.g. $\gamma + \text{jets}$ events are produced with very small E_T^{miss} , however due to timing mis-measurements, they may appear out-of-time and assigned large E_T^{miss} . Thus we conclude that collision events will generally have small \cancel{E}_T but

large \cancel{E}_T^γ .

We select control samples (CS) defined by \cancel{E}_T , \cancel{E}_T^γ and t_γ according to the ABCD technique to estimate our background contributions while remaining vigilant and taking into account the possible contamination to each background source from possible fluctuations in event rate as a result of our selection cuts in defining these CRs. The overall estimation technique is verified through a closure test procedure and the collision background estimation is validated using an extra control sample of $Z \rightarrow e^+e^-$ events for Z candidates reconstructed from photon candidates extended to include out-of-time events.

1. **$\cancel{E}_T^\gamma > 60 \text{ GeV}$:** CS in which collision (QCD) background is suppressed while halo, cosmic ray and spike photon is enhanced since most non-collision background photons are produced with high p_T hence large \cancel{E}_T^γ . Using this CS, we define four regions for estimating the non-collision background contribution using the ABCD recipe.

Non-Collision	$\cancel{E}_T < 60 \text{ GeV}$	$\cancel{E}_T > 60 \text{ GeV}$
$3.0 < t_\gamma < 13.0 \text{ ns.}$	C	D
$-10.0 < t_\gamma < -3.0 \text{ ns}$	A	B

Table 6.7: ABCD Control Regions (CRs) for estimating non-collision background.

Thus, the number of events expected in Control Region (CR) D using table 6.7 with the assumption that $\frac{N_D}{N_B} = \frac{N_C}{N_A}$ is given as:

$$N_D = \left(\frac{N_B}{N_A} \right) \cdot N_C \quad (6.3)$$

2. **$\cancel{E}_T > 60 \text{ GeV}$:** CS where non-collision background (halo, cosmic and spike photons) contribution is suppressed while collision (QCD) background contribution is enhanced. Further dividing this CS and applying $A' B' C' D'$ method to estimated collision contribution is shown in table 6.8.

Collision	$\not{E}_T < 60 \text{ GeV}$	$\not{E}_T > 60 \text{ GeV}$
$3.0 < t_\gamma < 13.0 \text{ ns.}$	C'	D'
$-2.0 < t_\gamma < 2.0 \text{ ns}$	I'	I
$-10.0 < t_\gamma < -3.0 \text{ ns}$	A'	B'

Table 6.8: $A' B' C' D'$ and $I I'$ CRs for estimating collision background.

Using CRs defined in table 6.8, we can estimate the contributions of collision background in both CRs B and D of our non-collision background CS as follows:

$$N_B^{col} = N_{B'} = \left(\frac{I}{I'} \right) \cdot N_{A'}, \quad N_D^{col} = N_{D'} = \left(\frac{I}{I'} \right) \cdot N_{C'} \quad (6.4)$$

where we have assumed that $\frac{N_{B'}}{N_{A'}} = \frac{N_I}{N_{I'}}$ and $\frac{N_{D'}}{N_{C'}} = \frac{N_I}{N_{I'}}$.

N_B^{col} and N_D^{col} are collision contributions to CRs B and A . The final combined background estimation is given by equation 6.5.

$$N_D^{Total} = \left(\frac{N_B - N_B^{col}}{N_A} \right) \cdot N_C + N_D^{col} \quad (6.5)$$

where $N_D^{Total} = N_D^{non-col} + N_D^{col}$ is the total background estimation in our signal region.

Closure Test

Selecting events with 0-jets and 1-jet, we performed closure test of our background estimation method. We also perform a cross-check on the assumptions used in our background estimations for small contributions for collision background using $Z \rightarrow e^+e^-$ events. Our underlying assumption here is that background contributions to large timing from collision source referred here as QCD is very small and must be of the order of 10^{-5} in comparison to in-time photons. i.e the ratio $N_{|t_\gamma|>3 \text{ ns}} / N_{|t_\gamma|<2.0 \text{ ns}} \approx 10^{-5}$ with N being the number of photons. The closure test compares the number of events observed in CR D to the number expected using our ABCD background estimation method in the same CR D . We observed 10 events while from using equation 6.5, we expected $16.78^{+2.95}_{-3.45}$. We argue that within our statistical uncertainties, there is quite an agreement between our expectation and observed events. The complete result from

our closure test is shown in table 6.9. This gives us confidence that our background estimation method is robust and reliable. We apply the same ABCD to estimate the background contribution in our signal sample. Our signal sample consist of events with at least 2-jets, at least a single photon and $\cancel{E}_T > 60 \text{ GeV}$, $\cancel{E}_T > 60 \text{ GeV}$.

Non-Collision	$\cancel{E}_T < 60 \text{ GeV}$	$\cancel{E}_T > 60 \text{ GeV}$
$3.0 < t_\gamma < 13.0 \text{ ns}$	C(405)	D(10) 16.78
$-10.0 < t_\gamma < -3.0 \text{ ns}$	A(871)	B(36)
Collision	$\cancel{E}_T < 60 \text{ GeV}$	$\cancel{E}_T > 60 \text{ GeV}$
$3.0 < t_\gamma < 13.0 \text{ ns}$	$D'(4)$	D(10)
$-2.0 < t_\gamma < 2.0 \text{ ns}$	$F'(1353685)$	F(34543)
$-10.0 < t_\gamma < -3.0 \text{ ns}$	$B'(5)$	B(36)

Table 6.9: Result from closure test of background estimation technique using 0 and 1-jet events. Numbers in bracket represent our expected background estimate using ABCD method.

6.3.4 Background Estimation Cross Check

The main assumption in our background estimation technique is that, the contribution from collision background events to out-of-time regions ($3.0 < t_\gamma < 13.0 \text{ ns}$) is negligible. In order to show that this assumption is correct, we select $Z \rightarrow e^+e^-$ events from `SingleElectron` and `DoubleElectron` data sets of 2012. Our motivation is to use a control sample where contributions from non-collision events is very small. We select Z candidate events from an extended photon sample including out-of-time photon events according to the following selection criteria:

- The candidate two electrons for the Z bosons must have individual $p_T > 25 \text{ GeV}$,
- The di-mass of these two electrons, $|m_{e^+e^-} - 91| > 61 \text{ GeV}/c^2$,
- Each electron must be in the barrel, $|\eta_{e^-}| < 1.479$ and $|\eta_{e^+}| < 1.479$.

At the electron super cluster level, we used the seed crystal time adjusted to account for the electron time of flight, as the electron time. The seed crystal must satisfy the recommended crystals or rechit cleaning criteria by the ECAL group which include

`kWeird`, `kBad`, `kPoorCalib` used for rejecting crystals showing anomalous behavior like spikes, noisy, bad crystals or poorly calibrated crystals. In this cross-check, we define our signal region as Z -candidate events with a well defined mass from both electrons i.e $76 < |m_{e^+e^-}| < 100 \text{ GeV}/c^2$ while the non Z events control sample are events which do not fall into this signal category. A quick look at photon t_γ vs η_γ and ϕ_γ plots as previously shown for halo photons in figure 6.9, shows that the electron candidates from the `Single/DoubleElectron` dataset when compared to the `SinglePhoton` dataset in figure 6.13 show no or very little contribution from cosmic, halo and anomalous photon events. This confirms our choice of the Z candidate events sample as a reliable sample to study collision events as it is free from non-collision events.

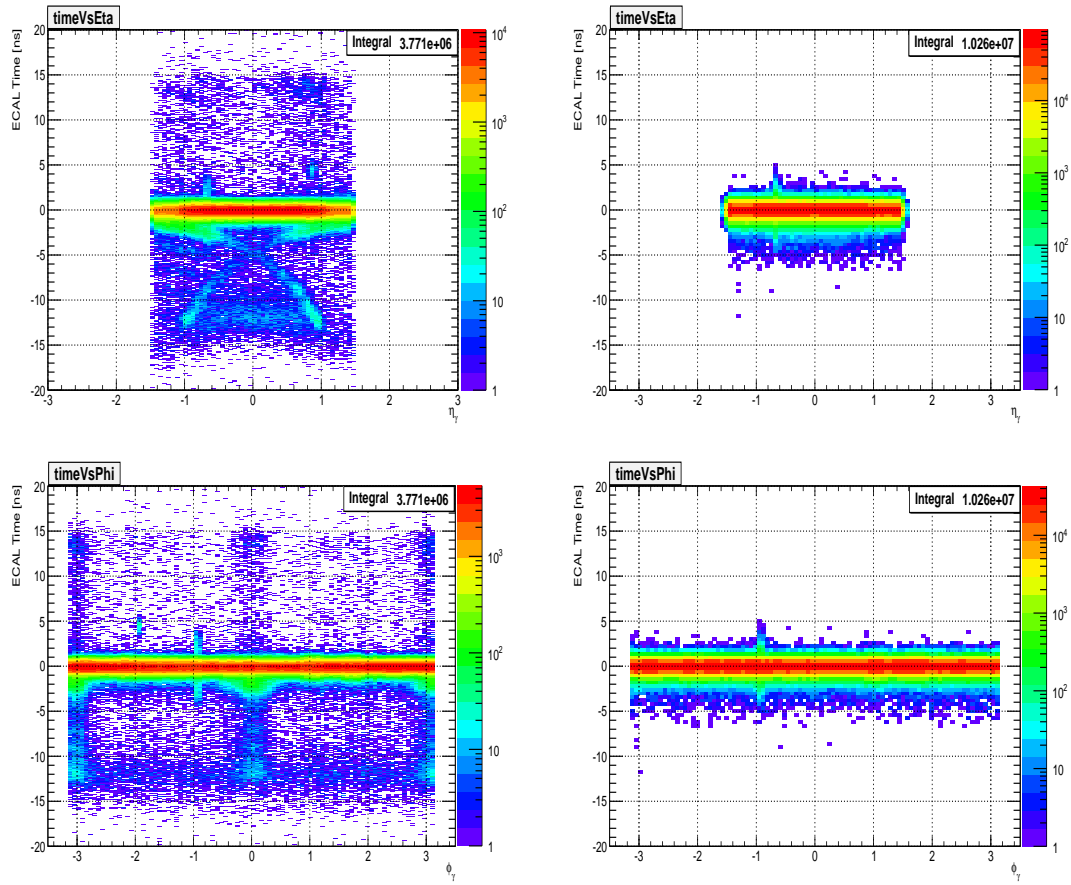


Figure 6.13: ECAL time, t_γ Vs η_γ (top) and t_γ Vs ϕ (bottom) for photons from **SinglePhoton** dataset (left) compared to electron candidates from the **DoubleElectron** dataset (right). All photons or electron candidates are in barrel subdetector. Most of the photons with $\phi = 0, \pm\pi$ are halo photons which are not observed in the Z boson candidate sample.

Figure 6.14 shows the Z boson mass reconstructed from the candidate electrons and timing of each electron for Signal (*top and blue*) and for our control sample (*bottom and red*).

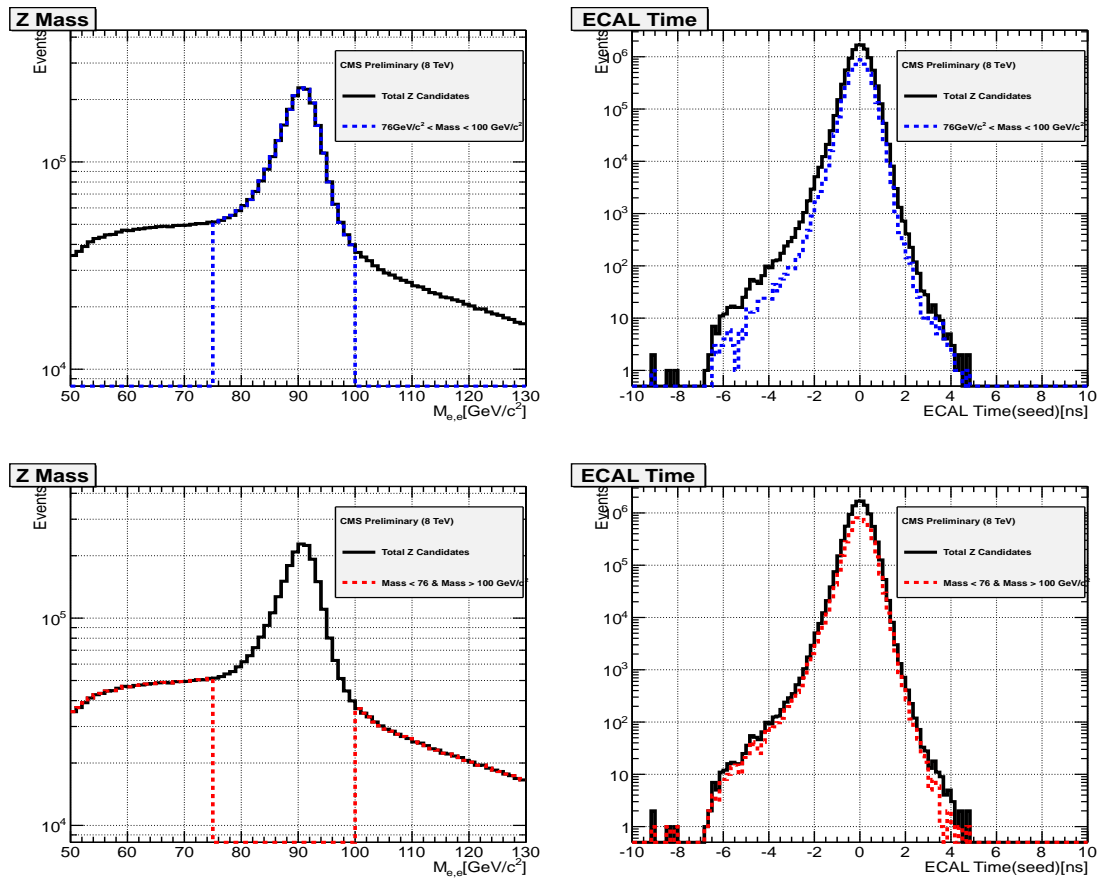


Figure 6.14: Di-electron candidate mass distribution and the time of both electrons for the signal $76 < m_Z < 100 \text{ GeV}/c^2$ Z boson sample(left) and similar distributions from the Control ($50 < m_Z < 76 \text{ GeV}/c^2$ and $100 < m_Z < 130 \text{ GeV}/c^2$) sample (right). Candidates events from the DoubleElectron dataset.

Using the background Z control sample, we estimate its contribution to out-of-time events using a simple scaling methods which can also be understood as an ABCD method. The method is applied as follows:

- Using a polynomial function, we fit the di-electron candidate mass distribution of the background control sample to extract a set of fit parameters,
- Using these fit parameters to define our polynomial function, we use this function to extract a scaling factor use to determine the true contribution of the background control region events in the signal region which in this case are Z bosons with possible large ECAL timing, $|t| > 3$ ns.
- We scale the background control sample timing distribution (electrons time) using the extracted scale factor. This scale factor is defined as,

$$\text{Scale Factor} = \frac{N}{M_1 + M_2}$$

- By subtracting the scaled background control sample Z candidates timing distribution from the signal sample Z candidate timing distribution, we are left with the real Z boson events whose electron time can fluctuate into larger timing region.
- Comparing the total number of observe electron candidates with $t > 3$ ns to those in-time, $|t| < 2$ ns, their ratio i.e $N_{t>3\text{ ns}}/N_{|t|<2.0\text{ ns}}$ gives us an estimate of the possible genuine electromagnetic objects from collision with large ECAL timing.

A simple picture showing the above procedure with distributions is shown in figure 6.15.

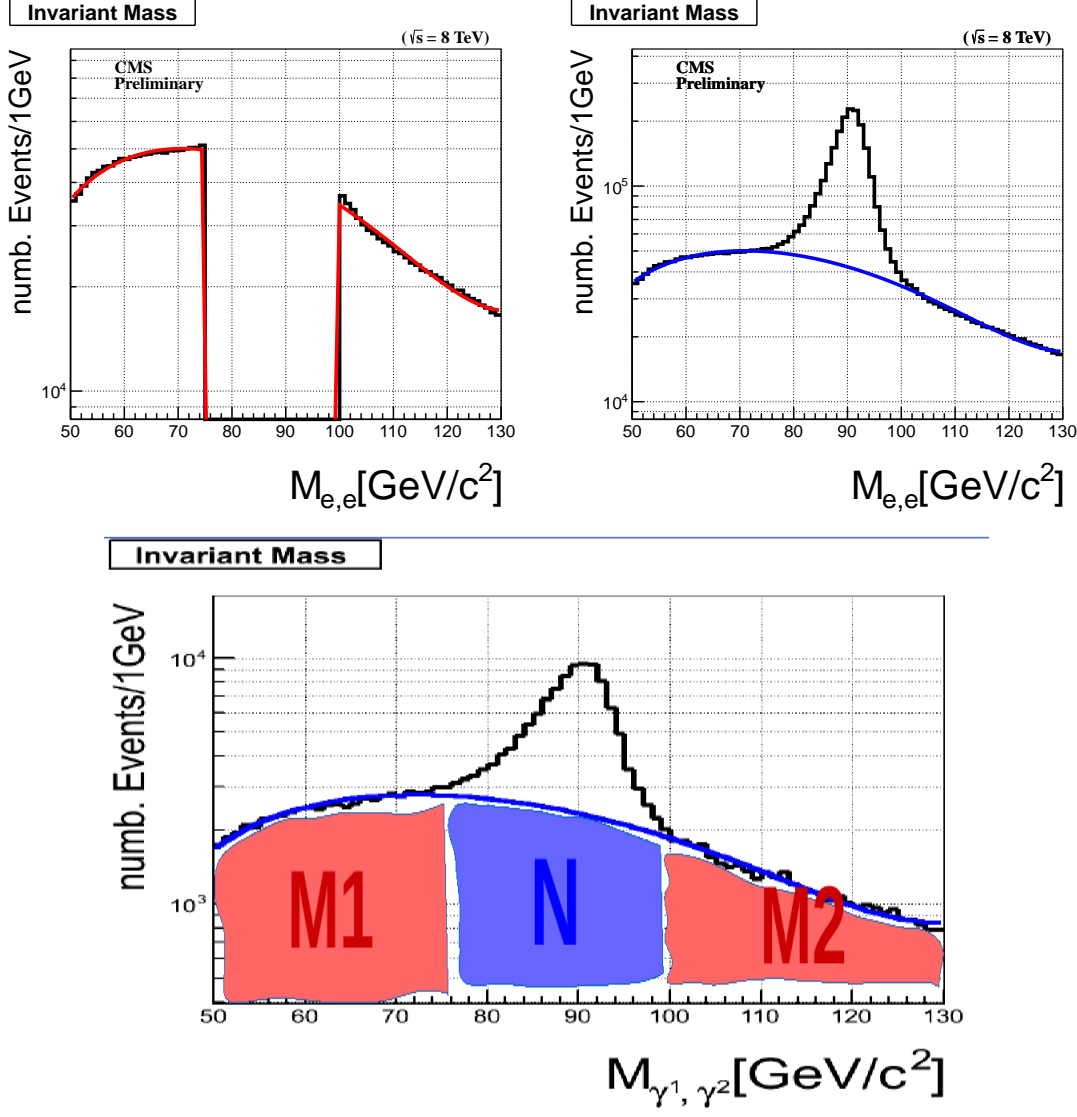


Figure 6.15: *Top:* Control sample (left) and signal sample (right) of di-electron candidate mass distribution. *Bottom:* Figure showing definition of scale factor use in estimating the contributions from control sample in signal sample.

The result of the final timing distribution for genuine Z boson events is shown in figure 6.16. It is not difficult to see that the ratio $N_{t>3 \text{ ns}}/N_{|t|<2.0 \text{ ns}} < 10^{-5}$ confirming that indeed the contribution of electromagnetic objects with large timing $t > 3 \text{ ns}$ is negligible and in agreement with our assumption that most collision events contain

photons which are mostly in-time, $|t| \leq 2$ ns. It's important to note that, we have not applied any E_T^{miss} selection cuts here. A simple cut, $E_T^{\text{miss}} > 60$ GeV could further reduce this ratio to an even smaller number as assumed in our above background estimation.

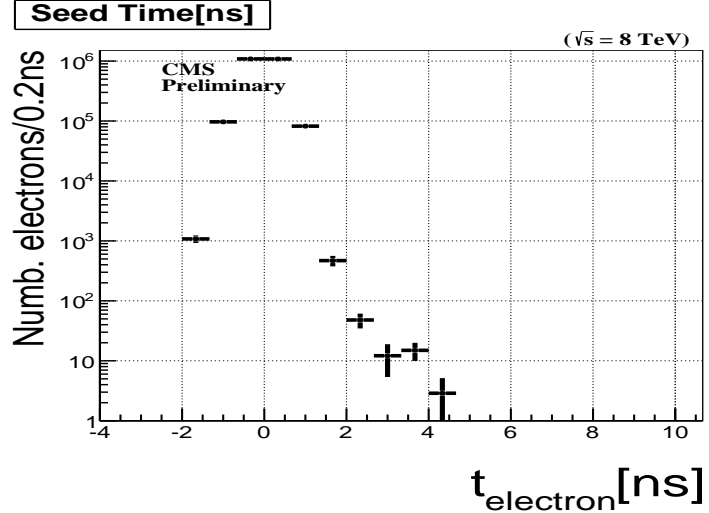


Figure 6.16: Timing distribution of genuine Z bosons after background contribution has been subtracted.

6.4 Results

Finally, we perform our background estimation on signal samples which are events with at least 2 jets, at least one high $p_T > 80$ GeV/c isolated photon with ECAL time $3.0 < t_\gamma < 13.0$ ns or $-10.0 < t_\gamma < -3.0$ ns and $\cancel{E}_T > 60$ GeV, $\cancel{E}_T > 60$ GeV.

We observed 1 event and expected $0.0888^{+0.1869}_{-0.0444}$ background events within our statistical uncertainties. Our complete result is shown in table 6.10 and in table 6.11, we show the number of GMSB SPS8 signal events passing our final selection for $\Lambda = 180$ TeV with different $c\tau$ values of the neutralino.

Non-Collision	$E_T < 60 \text{ GeV}$	$E_T > 60 \text{ GeV}$
$3.0 < t_\gamma < 13.0 \text{ ns}$	$C(0)$	$D(1)$
$-10.0 < t_\gamma < -3.0 \text{ ns}$	$A(5)$	$B(1)$
Collision	$E_T < 60 \text{ GeV}$	$E_T > 60 \text{ GeV}$
$3.0 < t_\gamma < 13.0 \text{ ns}$	$D'(5)$	D $0.0888^{+0.1869}_{-0.0444}$
$-2.0 < t_\gamma < 2.0 \text{ ns}$	$F'(657663)$	$F(30242)$
$-10.0 < t_\gamma < -3.0 \text{ ns}$	$B'(1)$	$B 0.23^{+0.092}_{-0.118}$

Table 6.10: Result of observed events and estimated background from signal sample, events with at least 2-jets. Numbers in bracket represent our observed number of events while numbers not in bracket are our expected number of background events estimated using ABCD method.

SPS8 GMSB Signal	Number of Events
GMSB(SPS8) ($\Lambda = 180 \text{ TeV}, c\tau = 250 \text{ mm}$)	0.2096
GMSB(SPS8) ($\Lambda = 180 \text{ TeV}, c\tau = 500 \text{ mm}$)	4.5423
GMSB(SPS8) ($\Lambda = 180 \text{ TeV}, c\tau = 1000 \text{ mm}$)	6.3646
GMSB(SPS8) ($\Lambda = 180 \text{ TeV}, c\tau = 2000 \text{ mm}$)	6.3968
GMSB(SPS8) ($\Lambda = 180 \text{ TeV}, c\tau = 4000 \text{ mm}$)	6.1442
GMSB(SPS8) ($\Lambda = 180 \text{ TeV}, c\tau = 6000 \text{ mm}$)	4.6498
GMSB(SPS8) ($\Lambda = 180 \text{ TeV}, c\tau = 12000 \text{ mm}$)	2.918

Table 6.11: Final number for $\Lambda = 180 \text{ TeV}$ GMSB SPS8 MC signal events passing our selection cuts.

6.5 Systematic Studies

The different sources of systematic which affect this analysis and the estimated contribution of each identified source of systematic is shown in table 6.12. These systematic is also used in the calculation of the upper limit on observed signal cross-section. We obtained these systematic percentage by varying each individual source and see how that affects the number of events passing our selection cuts. The systematic uncertainty on luminosity measurement has the recommended value of 2.2% provided by CMS and LHC luminosity measurements. The uncertainty for the jet energy corrections (JEC) and jet

energy scale (JES) has also been measured using the standard CMSSW tool by [63] and provided by the CMS JEMET working group. The uncertainty on the photon energy scale in barrel was estimated to be 1.0% and based on the final-state radiation (FSR) in $Z \rightarrow \mu\mu\gamma$ events [64]. The uncertainty from parton density functions (PDF) evaluated using the re-weighting technique using the Master Equation of CTEQ65 model set described in [65]. The uncertainty on the E_T^{miss} resolution uses a conservative estimate from [66]. The uncertainty on the ECAL timing obtained by comparing the peak in the timing distribution between $\gamma +$ jet sample and data events with time $|t| < 2$ ns is found to be of the order of 200 ps per event and from a study of high p_T photons beyond gain transitions has agreed by ECAL DPG to be a conservative estimate. Another important source of systematic is in the selection of the background control samples and our background estimation and individual systematic in the tagging and miss-tagging of non-collision background and estimating background contributions from collisions. We combined these separate systematic contributions into a single background estimation systematic referred here as our background estimation systematic. This is our largest source of uncertainty in our analysis which we estimate to vary from 50% to 200%.

Source	Uncertainty on $\sigma_{UL}^{\text{Exp}}(\%)$
Photon energy scale (1.0%)	< 3.0%
Jet energy scale	< 0.05%
Jet energy resolution (10%)	< 1.90%
PDF uncertainty (10%)	< 1.70%
E_T^{miss} resolution (10%)	< 2.8%
ECAL time uncertainty (0.5 ns)	< 5.0%
Background estimation uncertainty (50.0)	< 51.0%
Luminosity (4.5%)	< 2.2%

Table 6.12: Summary of systematic uncertainties used in this analysis and applied to our cross-section upper limit, σ_{UL} calculation.

Chapter 7

Statistical Analysis

7.1 Limit Computation

The upper limit calculation procedure used in this analysis is the CLs technique. We fed carefully estimated amounts of background and signal with systematic to obtain the limit. The variable for which the 95% upper limit is set unlike previous experiments is based entirely on the neutralino proper decay length, $c\tau_{\tilde{\chi}_1^0}$.

The method we used in our upper limit calculation is by first performing a Hypothesis test and then use the result of this test to derived our confidence intervals. We do the following:

- We define a NULL hypothesis (H_0) and the Alternate hypothesis (H_1). If we had several other hypothesis, we will defined them also.
- Select a Test statistics ($t(x)$), where x is the data.
- Select a corresponding test statistics calculator.
- Use the result of the hypothesis test to compute the interval by inverting the result of the hypothesis test.

First, we describe the acceptable technique in experimental high energy physics for computing *p-values* used in any search and discovery experiment.

7.1.1 CLs Technique

The CL_s technique [70] is attributed as the standard technique or framework for computing the confidence or exclusion intervals in a search and discovery experiment. It has been shown to work during the search for the Higgs boson at LEP and recently in the discovery of the scalar boson in 2012, by both CMS and ATLAS experiments with the mass of this boson being: $m_H = 125.36 \pm 0.37(\text{stat.Unc}) \pm 0.18(\text{syst.Unc})$.

This method has been implemented in a unique statistical software package called *HiggsCombine* with the goal of providing direct access to a variety of robust statistical methods with optimised performance for computing limits or confidence intervals. *HiggsCombine* [72] is the official standard tool recommended by the CMS statistical committee and CMS Higgs group for calculating limits in any CMS search and discovery analysis. It takes as input estimates on the number or distribution of signal and background and the observed number or distribution from data and produces an upper limit in the production cross section of a given physics process for a given value of a parameter of interest (POI). *Higgscombine* tool has the advantage in that, it allows for the possibility to use several different statistical methods of calculating the upper limit. This way, one can make comparison and simple checks for any inconsistency. In this analysis, we used an Asymptotic [73] and HybridNew (a hybrid of Frequentist and Bayesian methods),[72], to calculate our observed upper limits. The purpose of the using the CL_s method is to compute reliable upper limits in a search scenario when the observed signal is very small compared to the background. In the CL_s technique, one uses not the p-value (CL_{s+b}) but rather divide this by CL_b (which is 1 minus the p-value for background only hypothesis). The reason for this is to define a conditional probability conditioned to the scenario of observing only background or background only hypothesis. The CL_s is formally defined as:

$$CL_s = \frac{CL_{s+b}}{CL_b} = \frac{p_{s+b}}{1 - p_b} \quad (7.1)$$

where $s + b$ means signal and background.

7.1.2 Statistical Test Formalism

The Neyman-Pearson Theorem states that the likelihood ratio gives the most powerful hypothesis test. Therefore, we construct our test statistics t_μ as a function of the observed data, as a likelihood ratio. In a search analysis, one defines the null hypothesis H_0 describing only known processes, or the background only which is to be tested against an alternate hypothesis H_1 defined as a background and signal. However in the computation of upper limits:

- H_0 being the NULL hypothesis includes the background and signal ($s + b$) while
- H_1 being the ALTERNATE hypothesis includes only the background (b).

Using these, two hypothesis we quantify the level of agreement between our observed data with either of the hypothesis by computing a p -value (p -value if the probability under the assumption of a given hypothesis, of finding data of equal or greater incompatibility with the predictions of the given hypothesis). A given hypothesis is then regarded as being excluded if its p -value is observed below a given threshold. In particle physics, this threshold value for the p -value is 0.05 corresponding to 95% of confidence level (CL). The CMS accepted method of computing upper upper limit is based on mix of frequentist-hybrid significance test using the profilelikelihood ratio as a test statistics (HybridNew method). The parameter of interests in in our case the rate (cross section) of signal process as well as *nuissance parameters* as systematics for the background and signal models. This parametrized systematics effects results, as is always the case, to loss in sensitivity.

In this search experiment, for each event in the signal, we measured the timing of the photon as our observable. We use this value to construct a histogram $\mathbf{n} = (n_1, \dots, n_N)$. The expectation value for each value of n_i can be written as:

$$E[n_i] = \mu s_i + b_i \quad (7.2)$$

where μ is the parameter which determines the signal strength, when $\mu = 0$ means background-only and when $\mu = 1$ then we have the signal and background hypothesis.

The the mean number of entries in the i th bin from signal and background are given as:

$$s_i = s_{tot} \int_{bin,i} f_s(t; \theta_s) \quad b_i = b_{tot} \int_{bin,i} f_b(t; \theta_b) \quad (7.3)$$

with the functions $f_s(t; \theta_s)$ and $f_b(t; \theta_b)$ being the probability density functions (Pdfs) of the variable t for the signal and background events and θ_s and θ_b representing the parameters which characterise the shapes of the pdfs. s_{tot} and b_{tot} represents the total mean numbers of signals and backgrounds while the integrals represent the probabilities for an event to be found in bin i . $\theta = (\theta_s, \theta_b, b_{tot})$ denote all nuisance parameters (systematic uncertainties) while s_{tot} is the signal normalization is fixed to the value predicted by the nominal signal model.

The likelihood function is the product of the Poisson probabilities for all bins:

$$\mathcal{L}(\mu, \theta) = \prod_{r=1}^N \frac{(\mu s_r + b_r)^{n_r}}{n_r!} e^{-(\mu s_r + b_r)} \cdot \mathcal{G}(\theta) \quad (7.4)$$

where $\mathcal{G}(\theta)$ is a discrete (Poisson) distribution of the nuisance parameters. This distribution can be different for different nuisance parameter.

Using the likelihood function, the profilelikelihood ratio is then defined as:

$$\lambda(\mu) = \frac{\mathcal{L}(\mu, \hat{\theta})}{\mathcal{L}(\hat{\mu}, \hat{\theta})} \quad (7.5)$$

Here $\hat{\theta}$ is the the value of θ that maximizes \mathcal{L} for a specified μ , thus, it is referred to as the *conditional maximum-likelihood estimator* (CMLE) of θ (given as a function of μ). While $\mathcal{L}(\hat{\mu}, \hat{\theta})$ is the maximized (unconditional) likelihood function with $\hat{\mu}$ and $\hat{\theta}$ being its *maximum likelihood* (ML) estimators. The nuisance parameters broadens the profilelikelihood as a function of μ relative to what is expected if their values where fixed and this reflects in the loss of sensitivity or information about μ due to the systematic uncertainties.

7.1.3 Test Statistics and p -values

The above expression for $\lambda(\mu)$ shows that $0 \leq \lambda \leq 1$, where λ close to 1 indicates a very good agreement between the data and hypothesis value of μ . The test statistics to be used for our statistical test is defined as:

$$t_\mu = -2 \ln \lambda(\mu) \quad (7.6)$$

It is important to note that the test statistics approach to any statistical test is favourable because just by looking at the values of the test statistics, higher values corresponds to increasing incompatibility between the data and the value of μ which is from the signal hypothesis. This incompatibility or disagreement between the data and a given hypothesis is quantified by calculating the probability or p -value as:

$$CL_{s+b} = p_u = \int_{t_{\mu,obs}}^{\infty} f(t_\mu|\mu) dt_\mu \quad (7.7)$$

where, $t_{\mu,obs}$ is the value of the test statistics t_μ obtained from the data and $f(t_\mu|\mu)$ is a pdf constructed from t_μ depending on the signal strength μ . The set of values for μ that are rejected because their p -value is below a specified threshold value α lying on either sides of those not rejected gives a two sided confidence interval of μ and if just on one side of the ones not rejected gives an upper limit on the rejected values of μ .

In the background only scenario i.e $\mu = 0$, the test statistics is defined as:

$$q_\mu = \begin{cases} -2 \ln \lambda(0), & \hat{\mu} \geq 0 \\ 0, & \hat{\mu} \leq 0 \end{cases}$$

where $\lambda(0)$ is the profilelikelihood ratio for $\mu = 0$ defined in 7.5. and again to quantify the disagreement between the background-only hypothesis ($\mu = 0$) and the data is given by the p -value as:

$$CL_b = p_0 = \int_{q_{0,obs}}^{\infty} f(q_0|0) dq_0 \quad (7.8)$$

where $f(q_0|0)$ denotes the pdf if the test statistics q_0 under the background-only ($\mu = 0$) hypothesis. Figure 7.1 shows a sampling distributions of the test statistics and how the

p-values can be extracted from these distributions.

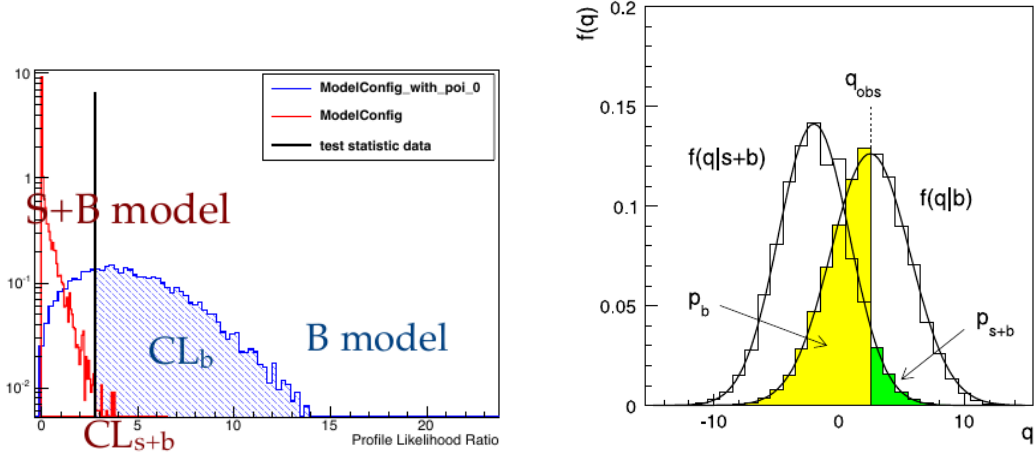


Figure 7.1: Sampling distributions for $f(t_\mu|\mu)$ showing how one extracts the *p*-values. left: is the using a analytic of the Asymptotic method and right: is from the HybridNew method.

In addition to the *p*-value, for expressing the disagreement between the data and a given hypothesis, the Higgscombine tool also provides a quantity known as the *significance* (\mathcal{Z}). \mathcal{Z} and the *p*-value have a very non-linear relation. Once can defined that relation using a two-sided fluctuation if a Gaussian variable σ , with 5σ significance corresponding to a *p*-value of $p = 5.7 \times 10^{-7}$ to denote a discovery. Since, we have not observed any significant excess of events over our standard model background, we will not mention a lot about significance in this thesis, but rather talk about *p*-values as they are indispensable in computing limits.

The important question is always, how does one obtain an expression or a distribution of the test statistics and $f(t_\mu|\mu)$ from the likelihood function? To answer this question, the HiggsCombine tool was developed which consist of various ways of both analytically (e.g the Asymptotic statistical method [73]) or through numerical integration or Monte Carlo computation (e.g the HybridNew statistical method) obtain the test statistics and $f(t_\mu|\mu)$. We have shown the limit computation results of both methods as used in this analysis. As an example, the pdf $f(q_\mu|\mu)$ of the test statistics (q_μ)

obtained through the **Asymptotic** statistical method as given in [73] is:

$$f(t_\mu|\mu') = \Phi\left(\frac{\mu - \mu'}{\sigma}\right)\delta(t_\mu) + \frac{1}{2}\frac{1}{\sqrt{2\pi}}\frac{1}{t_\mu} \exp\left[-\frac{1}{2}\left(\sqrt{t_\mu} - \frac{\mu - \mu'}{\sigma}\right)^2\right] \quad (7.9)$$

where result to a half-chi-square distribution when $\mu = \mu'$.

In subtle point worth mentioning is that in the HybridNew approach, systematics uncertainties are taken into account through the Bayesian prior density $\pi(\theta)$, and the distribution of the test statistics is computed under the assumption if the Bayesian model of average given as:

$$f(q) = \int f(q|\theta)\pi(\theta)d\theta$$

and the prior pdf $\pi(\theta)$ is obtained from some measurements characterised by a given likelihood function $\mathcal{L}_\theta(\theta)$ which is then used to find the prior using Bayes' Theorem. Unlike other cases where systematic uncertainties are taking as being part of the data and incorporated directly through $\mathcal{G}(\theta)$ as shown in equation 7.4. Nevertheless, they arrive at the same result.

In summary, the hypothesis test is performed using a given statistical method on each value of a chosen parameter of interest (POI)(usually denoted μ). The p -value if obtained from the sampling distribution of the test statistics being used. Can either obtain this test statistics analytically or through Monte Carlo computation and numerical integration. By plotting the p-value as a function of the POI, we obtain the p-value curve (in this case the $CL_s = \frac{CL_{s+b}}{CL_b}$). The value of μ which has a p-value α (e.g 0.05) is the upper limit (for 1-dimensional limits, 2-dimensional limits gives lower and upper limits) of $1 - \alpha$ confidence interval (e.g 95%).

combined result

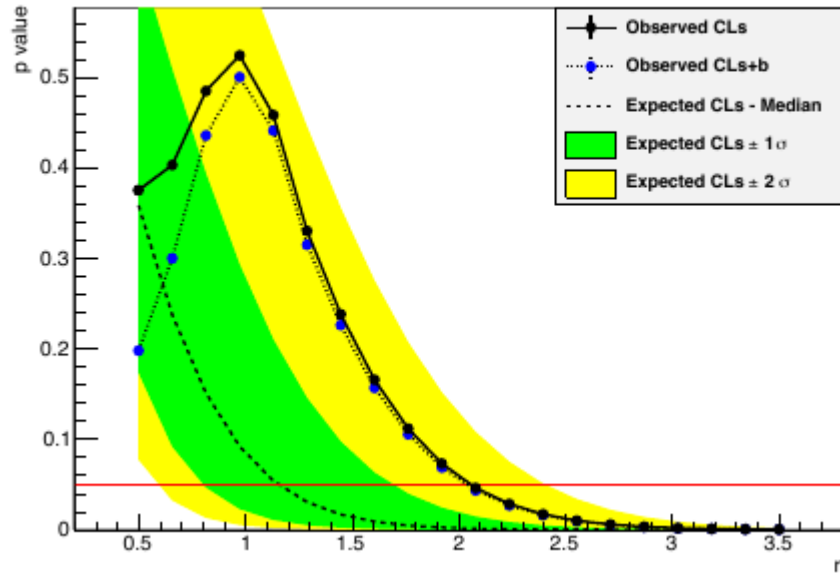


Figure 7.2: Distribution of p -values showing how upper limit on μ is extracted for a given threshold probability.

Chapter 8

Limit Interpretation

Using the CL_s technique, the HiggsCombine tool produces an upper limit along with the expected limit at different quantiles as the signal strength computed which is a ratio of Number of Signal events over the Number of Expected signal events i.e

$$r = \frac{N^{Obs}}{N_{expect}} \quad (8.1)$$

and using the equation as given in chapter 3 on the cross-section $\sigma = \frac{N}{\varepsilon \cdot A \cdot \mathcal{L}}$ and hence the observed cross-section upper limit is given as:

$$\sigma_{UL}^{Obs} = \frac{r \cdot N^{expect}}{\varepsilon \cdot A \cdot \mathcal{L}} \quad (8.2)$$

where \mathcal{L} is the integrated luminosity (19 fb^{-1}) and ε and A are the signal selection efficiency and Acceptance respectively. In addition to the observed limits (Solid black line), the uncertainties on the expected limits at 68%/16% ($\pm 1\sigma$) and at 98%/2.5% ($\pm 2\sigma$) provide the **GREEN** and **YELLOW** respectively, the error from the median (50%) expected limits (dashed red line) shown in figure 8.2.

8.1 Signal Efficiency and Acceptance

The efficiency times acceptance ($\varepsilon \times A$) combined as one is seen the figure 8.1.

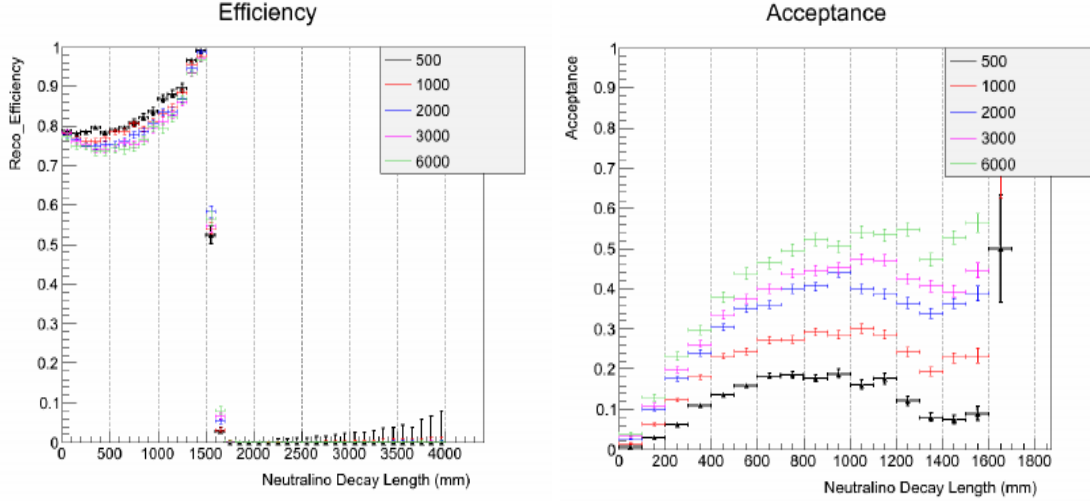


Figure 8.1: The reconstruction and selection efficiency (left) \times Acceptance ($t > 3$ ns) (right) against transverse decay length in laboratory frame for different $c\tau$ points.

The $\frac{N_{expet}}{\mathcal{L}}$ defines the expected signal cross section which is obtained from a given signal model. In our scenario, our choice of signal model we want to produce exclusion limits on the possible production and decay of a long-lived particle described by this signal model is GMSB. Thus the interpretation of our search analysis is given within the context of any GMSB model with a long-live neutral particle decaying to a photon and gravitino. Such a model is the minimal GMSB or the SPS8 model and the general GMSB model. However, the results provided are based on interpretation within the context of the SPS8 model. In GMSB, the neutralino $\tilde{\chi}_1^0$ is the NLSP and decays to the gravitino \tilde{G} the LSP (as a result of R-parity conservation) in association with a very energetic photon γ . Because of the smallness in mass difference between the $\tilde{\chi}_1^0$ and the \tilde{G} as well as the coupling, the $\tilde{\chi}_1^0$ decay to \tilde{G} is delayed and as a result, the photon emitted can arrive late in the calorimeter crystals. Measuring the arrival time of the photon on ECAL crystals, we can extract important parameters of theory of GMSB.

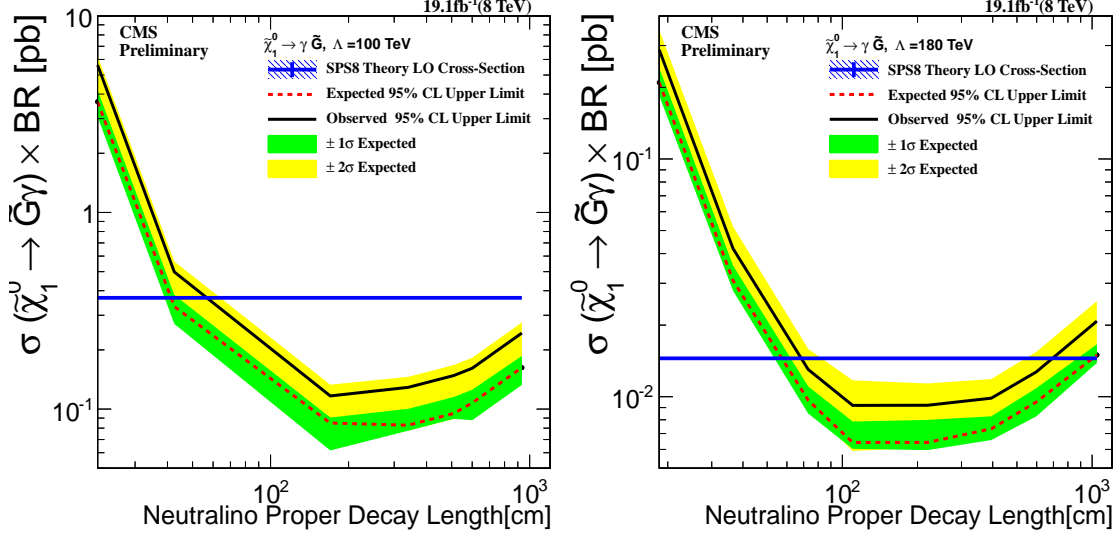


Figure 8.2: Neutralino production cross section against proper delay length upper limit interpretation in SPS8 model. (Left) $\Lambda = 100$ TeV, (Right)(left) $\Lambda = 180$ TeV

In the SPS8 model, the parameter space for long-live neutralinos is governed by $\Lambda_m - c\tau$ 2-dimensional parameter space. For each Λ_m point, we have a fixed neutralino mass with different proper lifetimes $c\tau$. We have obtained limits for Λ_m ranging from 100 TeV to 180 TeV corresponding to lightest neutralino mass $m_{\tilde{\chi}_1^0}$ between 90 to 255 GeV/c^2 and proper lifetime $c\tau$ ranging from 250 to 12000 mm corresponding to $\tau_{\tilde{\chi}_1^0}$ from 0.8 ns to 40 ns.

For a given value of $\Lambda_m = 180$ TeV, we have a lightest neutralino production cross section times branching ratio plot shown in figure 8.2, showing that the ECAL detector is sensitive to lightest neutralinos of mass $m_{\tilde{\chi}_1^0} = 255$ GeV/c^2 and life time upto 30 ns and we are 95% confident that we have not missed any neutralino whose mass is $m_{\tilde{\chi}_1^0} = 255$ GeV/c^2 and lifetime is $\tau \leq 30$ ns.

For a given lifetime of $\tau = 20$ ns, we can also obtain upper limits on the production cross section times branching ratio when compared against their theoretically expected values for a lightest neutralino with mass ranging from $m_{\tilde{\chi}_1^0} = 90$ GeV/c^2 to $m_{\tilde{\chi}_1^0} = 255$ GeV/c^2 . The observed upper limit on this cross section is $\sigma_{\tilde{\chi}_1^0}^{UP} \geq XX$ pb with proper lifetime of $\tau = 30$ ns.

Using both the mass and proper lifetime of the lightest neutralino, we present possible

2-dimensional limits simultaneously on $m_{\tilde{\chi}_1^0}$ or Λ_m and $c\tau$ or τ in the SPS8 model, comparing this with the result of previous experiments. This is shown in figure 8.3.

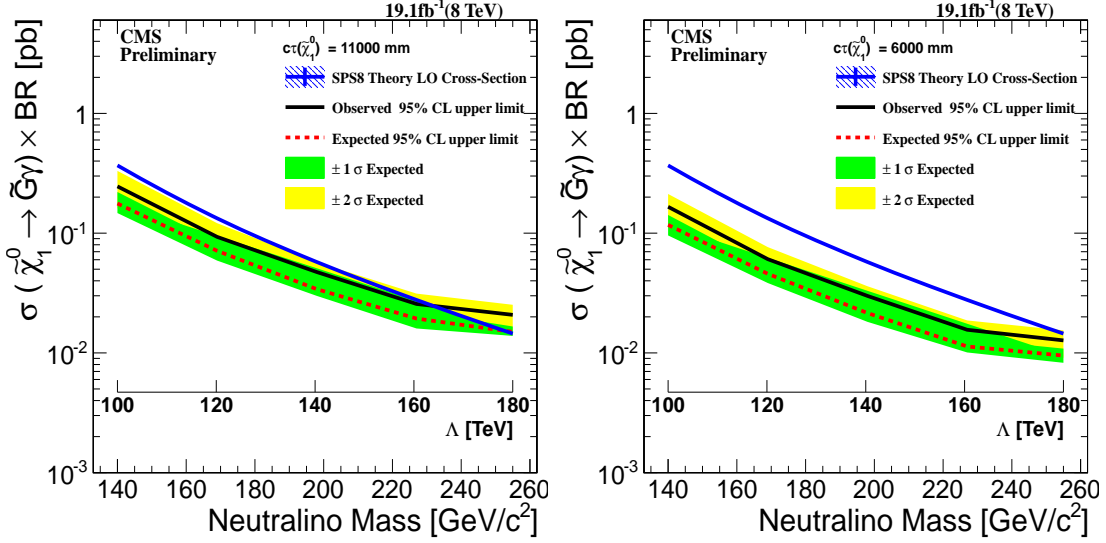


Figure 8.3: Neutralino production cross section against neutralino mass upper limit at 95% confidence levels interpretation in SPS8 model. (Left) $C\tau = 11000 \text{ mm}$, (Right) $C\tau = 6000 \text{ mm}$

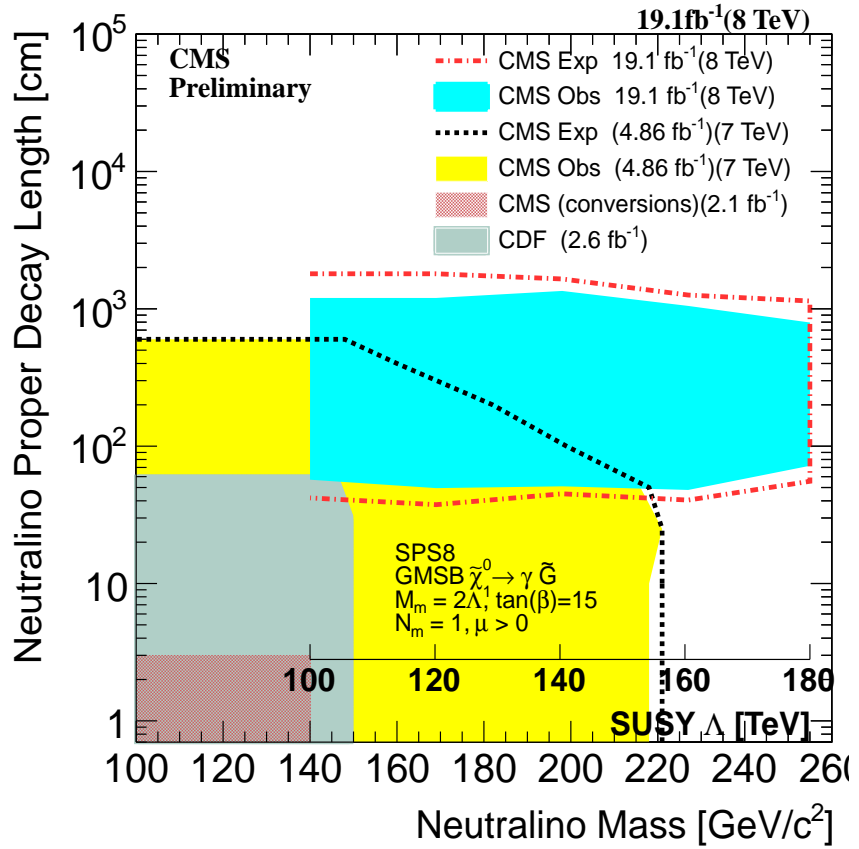


Figure 8.4: Neutralino two dimensional exclusion limit of neutralino mass (Λ) against proper delay length upper limit interpretation in SPS8 model in the decay $\tilde{\chi}_1^0 \rightarrow \gamma + \tilde{G}$ with limits from previous experiments shown.

Chapter 9

Conclusion

We have performed a search analysis for NMLLP decaying to photons using the time of arrival of the photon as measured by the ECAL sub detector of the CMS detector. Haven fail to find any significant signal of delayed photons over the standard model background, we interpreted our results in SUSY models with NMLLP like SPS8 of minimal GBSM or general GMSB models. We showed that, neutralinos whose production and decay mechanism is described in the SPS8 mGMSB model, with $m_{\tilde{\chi}_1^0} \leq 235 \text{ GeV}/c^2$ and $\tau_{\tilde{\chi}_1^0} \leq 35 \text{ ns}$ are ruled out of existence at 95% confidence level using the 2012 8 TeV LHC dataset. This corresponds to an upper limit of $\sigma_{\tilde{\chi}_1^0}^{UP} \geq 0.02 \text{ pb}$ on the production cross section times branching ratio in a hadron collider. In addition, we mention some of the limitations in this particular analysis from a detector point of view and how in future studies can be improved. We hope that in the future, with increase in center of mass energy of the LHC collider as well as luminosity and an improve in timing resolution beyond what is already very reliable, we will surely find a new fundamental particle whose dynamics cannot be described by the already very successful standard model of particle physics.

Bibliography

- [1] “*Observation of a new boson at a mass of 125 GeV with the CMS experiment at LHC*”, *Phys. Lett. B* 716 (2012) 30-61
- [2] Steven Weinberg, “A Model of Leptons”, *Phys. Rev. Lett.* 19, 12641266 (1967)
- [3] “Observation of a Charged Charmoniumlike Structure in $e^-e^+ \rightarrow \pi^+\pi^-J/\psi$ at $\sqrt{S} = 4.26\text{GeV}$ ” M. Ablikim et al. *Phys. Rev. Lett.* 110, 252001 (2013), “Study of $e^-e^+ \rightarrow \pi^+\pi^-J/\psi$ and Observation of a Charged Charmoniumlike State at Belle”, Z. Q. Liu et al. *Phys. Rev. Lett.* 110, 252002 (2013);
- [4] Peter W. Higgs “Broken symmetries and the masses of gauge bosons”, *Phys. Rev. Lett.* 13.508, 19 October, 1964;
- [5] Ellis John, Olive Keith A. (2010). “Supersymmetric Dark Matter Candidates”. arXiv:1001.3651 [astro-ph]
- [6] J.Ellis, J.Hagelin, D. Nanopoulos, K.A. Olive and M. Srednicki; *Nucl. Phys.* B238 (1984) 453; H. Goldberg, *Phys. Rev. Lett.* 50 (1983) 1419; J. Ellis, T. Falk, G. Ganis, K.A. Olive and M. Srednicki, *Phys. Lett. B* 510 (2001) 236, arXiv: hep-ph/0102098.
- [7] H. N. Brown et al., Muon $g_\mu - 2$ Collaboration, *Phys. Rev. Lett.* 88 (2002) 2227, hep-ex/0102017; A. Czarnecki and W.J. Marciano, *Phys. Rev. D* 64 (2001) 013014, hep-ph/0102122.
- [8] M. Knecht and A. Nyffeler, hep-ph/0111058; I. Blokland, A. Czarnecki and K. Melnikov *Phys. Rev. Lett.* 88 (2002) 071803 hep-ph/0112117

- [9] CLEO Collaboration, M. S Alan et al., *Phys. Rev. Lett.* 74 (1995) 2885 as updated in S. Amed et al., CLEO CONF 99-10;
- [10] BELLE Collaboration hep-ex/0103042;
- [11] S.Mathin, arXiv:hep-ph/9709356;
- [12] B.Allanach et al,arXiv:hep-ph/0202233v1;
- [13] Haag,Rudolf; Sohnius, Martin; opuszaski, Jan T. “All possible generators of supersymmetries of the S-matrix”, Nuclear Physics B 88: 257274 (1975);
- [14] Salam, A.; Strathdee, J. (1974). “Super-gauge transformations”. Nuclear Physics B 76 (3): 477201;
- [15] Howard Baer, Xerxes Tata “Weak Scale Supersymmetry: From Superfields to Scattering Events”
- [16] Laura Covi “Gravitino Dark Matter confronts LHC” Journal of Physics: Conference Series 485 (2014) 012002
- [17] N.-E. Bomark and L. Roszkowski “3.5 keV x-ray line from decaying gravitino dark matter” Phys. Rev. D 90, 011701(R) Published 18 July 2014
- [18] G.F. Giudice and R. Rattazzi “ Theories with Gauge-Mediated Supersymmetry Breaking” arXiv:hep-ph/9801271v2
- [19] Steven Abel a,b , Matthew J. Dolan et al “Pure General Gauge Mediation for Early LHC Searches” arXiv:1009.1164v2 [hep-ph].
- [20] M. Dine and A. E. Nelson, Phys. Rev. D 48, 1277 (1993), arXiv:hep-ph/9303230
- [21] P. Meade, N. Seiberg, and D. Shih, Prog. Theor. Phys. Suppl. 177, 143 (2009), arXiv:0801.3278 [hep-ph]
- [22] M. Buican, P. Meade, N. Seiberg, and D. Shih, J. High Energy Phys. 0903, 016 (2009), arXiv:0812.3668 [hep-ph]
- [23] M. Dine, A. E. Nelson, and Y. Shirman, Phys. Rev. D 51, 1362 (1995), arXiv:hep-ph/9408384

- [24] M. Dine, A. E. Nelson, Y. Nir, and Y. Shirman, Phys. Rev. D 53, 2658 (1996), arXiv:hep-ph/9507378
- [25] J. T. Ruderman and D. Shih, J. High Energy Phys. 1208, 159 (2012), arXiv:1103.6083[hep-ph]
- [26] S. Ambrosanio 1 , Graham D. Kribs 2 , and Stephen P. Martin hep-ph/9703211 arXiv:hep-ph/9703211v2.
- [27] J.Dann et al.(LEPSUSY Working Group), Internal note LEPSUSYWG/97-04(1997), P. Janot, talk at the EPS Conference, Jerusalem, 1997.
- [28] CDF Collaboration, “Search for Supersymmetry with Gauge-Mediated Breaking in Diphoton Events with Missing Transverse Energy at CDFII “, *Phys. Rev. Lett.*
- [29] ATLAS Collaboration “Search for Diphoton Events with Large Missing Transverse Momentum in $1 fb^{-1}$ of 7TeV Proton-Proton Collision Data with the ATLAS Detector”, arXiv:1111.4116v1, 17th Nov 2011.
- [30] CMS Draft Analysis, “Search for Long-Lived Particles using Displaced Photons in PP Collision at $\sqrt{S} = 7TeV$ ”, CMS AN AN-11-081 104(2010)011801,
- [31] ATLAS Collaboration, J. High Energy Phys. 1212, 124 (2012), arXiv:1210.4457 [hep-ex]
- [32] The LHC Machine, Lyndon Evans and Philip Bryant *Jinst*,
- [33] The CERN Brochure 2009-003-Eng
- [34] CMS Collaboration, “The CMS experiment at the CERN LHC”, JINST 0803:S08004, 2008.
- [35] CMS uses a right-handed coordinate system, with the origin at the nominal interaction point, the x -axis pointing to the center of the LHC, the y -axis pointing up (perpendicular to the LHC plane), and the z -axis along the counterclockwise-beam direction. The polar angle, θ , is measured from the positive z -axis and the azimuthal angle, ϕ , is measured in the x - y plane. $\eta = -\ln \tan(\theta/2)$. The transverse energy

and momentum are defined as $\mathbf{E}_T = E \sin \theta$ and $\mathbf{p}_T = p \sin \theta$ where E is the energy measured in the tracking system. $\mathbf{E}_T^{\text{miss}} = | - \sum_i \mathbf{E}_T^i \vec{n}_i |$ where \vec{n}_i is a unit vector that points from the interaction vertex to the transverse plane.

- [36] “Timing Distribution at the LHC”, B.G. Taylor Colmar, 9-13 September 2002
- [37] “An FPGA based multiprocessing CPU for Beam Synchronous Timing in CERNs SPS and LHC”.*Proceedings of ICAL EPICS 2003, Gyeongju, Korea ICAL EPICS 2003*
- [38] “Timing and Synchronization in the LHC Experiments”, Varela, J. Krakv, 11-15 September 2000.
- [39] <http://ttc.web.cern.ch/TTC/intro.html>
- [40] CMS Collaboration, “CMS Physics: Technical design report, Volume 1” CERN-LHCC-2006-001
- [41] “Study of the LHC ghost charge and satellite bunches for luminosity calibration.”, CERN-ATS-Note-2012-029 PERF
- [42] “LHC bunch current normalisation for the April-May 2010 luminosity calibration measurements.”, CERN-ATS-Note-2011-004 PERF
- [43] CMS Collaboration, “The electromagnetic calorimeter. Technical design report”,, CERN-LHCC-97-33
- [44] Bo Lofstedt, “The digital readout system for the CMS electromagnetic Calorimeter”,*Nucl. Inst. Methods in Physics Research*,A 453 (2000) 433-439
- [45] CMS Electromagnetic Calorimeter Collaboration, “Energy resolution of the barrel of the CMS Electromagnetic Calorimeter”,*JINST* 2(2007)P04004.
- [46] CMS Collaboration, “Time Reconstruction and Performance of the CMS Crystal Electromagnetic Calorimeter”,CFT-09-006, 2009.
- [47] <https://twiki.cern.ch/twiki/bin/viewauth/CMS/ECALDPGTimeCalibration>
- [48] <https://twiki.cern.ch/twiki/bin/viewauth/CMS/ECALDPGHwTimeCalibration>

- [49] CMS Collaboration, “The CMS ECAL performance With examples”, *JINST* 9 C02008, 2014.
- [50] CMS-DP-2014/011: “*ECAL Timing Performance Run1*”
- [51] <https://twiki.cern.ch/twiki/bin/view/CMSPublic/EcalDPGResultsCMSDP2014011>
- [52] <https://twiki.cern.ch/twiki/bin/view/CMSPublic/EcalDPGResultsCMSDP2014012>
- [53] “Characterization and treatment of anomalous signals in the CMS Electromagnetic Calorimeter” CMS AN AN-10-357
- [54] “ Mitigation of Anomalous APD signals in the CMS ECAL”, *JINST* 8 C03020, W.Bialas and D.A. Petyt
- [55] CMS Collaboration, “CMS trigger and data taking in 2010 ”, *CMS CR-2011/051*.
- [56] CMS Collaboration, “Reconstruction of the signal amplitude of the CMS electromagnetic Calorimeter”, *Eur.Phys.J.* C46S1(2006)23-35.
- [57] D.del Re et al “An algorithm for the determination of the flight path of long-lived particles decaying into photons” CMS AN -2010/212.
- [58] CMS Collaboration,“Particle-Flow Event Reconstruction in CMS and Performance for Jets, taus and \cancel{E}_T ”, CMS Physics Analysis Summary CMS-PAS-PFT-09-001(2009).
- [59] CMS Collaboration, Missing Transverse Energy Performance in Minimum-Bias and Jet Events from Proton-Proton Collisions at $\sqrt{s} = 7$ TeV , CMS Physics Analysis Summary CMS-PAS-JME-10-004 (2010).
- [60] MET JINST (arXiv:1106.5048)
- [61] CMS Collaboration, “Missing transverse energy performance of the CMS detector”; arXiv:1106.5048v1
- [62] CMS Collaboration,“CMS Physics: Technical design report, Volume 2” CERN-LHCC-2006-001.

- [63] CMS Collaboration, “Determination of Jet Energy Scale in CMS with pp collisions at $\sqrt{S} = 8$ TeV”, *JME-10-010(2012)*
- [64] “<https://twiki.cern.ch/twiki/bin/viewauth/CMS/EGamma2012>.”
- [65] “Parton distributions for the LHC” *Eur.Phys.J C63(2009) 189-285* or arXiv:0901.0002
- [66] CMS Collaboration, “Search for ADD Extra-dimensions with Photon + MET signature”, *AN-11-319(2011)*
- [67] ISAJET 7.84 F.E. Paige, S.D. Protopopescu, H. Baer and X. Tata, <http://www.nhn.ou.edu/~isajet/>
- [68] T. Sj ostrand, S. Mrenna, and P. Skands, PYTHIA 6.4 physics and manual, *JHEP 05 (2006) 026*, doi:10.1088/1126-6708/2006/05/026, arXiv:hep-ph/0603175
- [69] GEANT4 Collaboration, GEANT4a simulation toolkit, *Nucl. Instrum. Meth. A 506(2003) 250*, doi:10.1016/S0168-9002(03)01368-8.
- [70] “Presentation of search results: the CLs technique”, *A. L Read 2002 J. Phys. G: Nucl. Part. Phys. 28 2693*
- [71] “Computation of confidence levels for search experiments with fractional event counting and the treatment of systematic errors”, *Peter Bock JHEP01(2007)080*
- [72] <https://twiki.cern.ch/twiki/bin/viewauth/CMS/>
- [73] “Asymptotic formulae for likelihood-based tests of new physics” *G. Cowan et al, arXiv:1007.1727v3*

Appendix A

Glossary and Acronyms

Care has been taken in this thesis to minimize the use of jargon and acronyms, but this cannot always be achieved. This appendix defines jargon terms in a glossary, and contains a table of acronyms and their meaning.

A.1 Glossary

- **Cosmic-Ray Muon (CR μ)** – A muon coming from the abundant energetic particles originating outside of the Earth’s atmosphere.
- **SUSY** – A theoretical model based on a fundamental symmetry called supersymmetry in which the fermions and bosons can exchange their spin, extending the standard model to account for the stability in the observed Higgs boson mass and to also predicting the existence of many extra new particles which could be candidates of dark matter.

A.2 Acronyms

Table A.1: Acronyms

NMLLP	Neutral Massive Long-Lived Particles.
DM	Dark Matter.
DE	Dark Energy.
GMSB	Gauge Mediated Supersymmetry Breaking
LHC	Large Hadron Collider
CMS	Compact Muon Solenoid
CR μ	Cosmic-Ray Muon